

Photonics in the ferroelectric super-crystal phase

Advisor: Eugenio Del Re

Dept. of Physics

PhD Thesis
February 2022



SAPIENZA
UNIVERSITÀ DI ROMA

Ludovica
Falsi

This page is intentionally left blank



SAPIENZA
UNIVERSITÀ DI ROMA

Photonics in the ferroelectric super-crystal phase

Modelli Matematici per l'Ingegneria, Elettromagnetismo e Nanoscienze
Dottorato di Ricerca in Elettromagnetismo – XXXIV Ciclo

Candidate

Ludovica Falsi

ID number 1334326

Thesis Advisor

Prof. Eugenio Del Re

31/10/2021

Thesis defended on 16/02/2022
in front of a Board of Examiners composed by:
Fulvio Mercuri, Stefano Trillo, Giovanni Leone (chairman)

Photonics in the ferroelectric super-crystal phase
Ph.D. thesis. Sapienza – University of Rome

© 2022 Ludovica Falsi. All rights reserved

This thesis has been typeset by L^AT_EX and the Sapthesis class.

Author's email: ludovica.falsi@uniroma1.it

"I say to you: One must have chaos in oneself to give birth to a dancing star"
F. Nietzsche, Thus spoke Zarathustra

Abstract

Nanodisordered ferroelectric perovskites belong to the family of relaxor ferroelectrics, and have long been attracting considerable attention in view of their unique physical properties. The introduction of compositional disorder on the nanoscale leads to the appearance of a broad temperature and frequency dependent peak in the dielectric susceptibility that manifests thermal, electric field, and strain hysteresis and is associated with anomalous relaxation. The presence of different compounds introduces, for specific composition concentrations, competing structural phases leading to unique polarization properties, such as the anomalous large capacitance and the giant piezoelectric effect. Recently, a new ferroelectric phase of matter, the spontaneous super-crystal phase (SC), has been discovered in bulk solid-solution of nanodisordered ferroelectric perovskite, several degrees below the Curie point. In this phase, domains, instead of locking into a disorganized pattern of clusters, form a 3D regular lattice of spontaneous polarization with micrometer lattice constant across macroscopic samples. This phase mimics standard solid-state structures but on scales that are thousands of times larger. The work presented in this thesis is an experimental investigation, through several photonics techniques, of the SC phase. In order to investigate the properties of the underlying ferroelectric domains, we first analyze the light-polarization dynamics which emerge from the interplay of mesoscopic domain ordering and anisotropy. Results indicate that polarized light propagating through the SC spatially separates in its polarization components, of mutually orthogonal linear polarization states. Furthermore, performing diffraction and refraction experiments, we discover that the SC phase is also accompanied by a broadband giant refraction (GR). Here the effective index of refraction is greater than 26 across the entire visible spectrum, even though no optical resonance is in place. The result is a material with no chromatic aberration and no diffraction. The discovery of GR opens up a wholly new realm of study, allowing us to expand our investigation to the field of nonlinear optics. Enhanced response causes wavelength conversion to occur in the form of bulk Cherenkov radiation with an arbitrarily wide spectral acceptance, more than 100 nm in the near infrared spectrum, an ultra-wide angular acceptance, up to $\pm 40^\circ$, with no polarization selectivity. From a more fundamental point of view, trying to understand the behavior and physics of complexity-driven GR, in particular the role played by ferroelectric clusters, using a 3D orthographic cross-polarizer projection technique, we provide for the first time, direct imaging of fractal cluster percolation. We also study the effect that the SC, of micrometer-scale, has on the average atomic structure, using several results, obtained

through different experimental techniques, from X-ray diffraction, to calorimetry. What we have found, is that the emergence of the SC is accompanied by a large scale and coherent anomalous lattice deformation. Alongside the investigation of the SC phase, we have exploited the strong nonlinear optical response of disordered ferroelectric crystals at the phase transition, which makes these materials suitable to study the physics of nonlinear waves. In our study, we focus principally on the exploration of applications in electro-optic integrated circuits, based on linear and nonlinear waves, and on the analysis of the physical origin of so-called soliton rogue waves.

After a brief introduction on the general context of nanodisordered ferroelectric perovskites, the work is organized as follows. The first part, is focused on the study of nanodisordered ferroelectric crystal, using light as the main probe in the understanding the SC phase. The main experimental findings are presented according to the following chapters.

Chapter 1 is a brief introduction on ferroelectric crystals. Focus is on the peculiar properties of nanodisordered ferroelectric perovskites and the SC phase, highlighting the different properties of the engineered and the spontaneous SC in different ferroelectric systems.

Chapter 2 is an experimental analysis on how the domain structure of the SC affects the propagation of polarized light.

Chapter 3 contains one main result of this Thesis. We use both laser light and white light, to demonstrate a giant index of refraction.

Chapter 4 describes the nonlinear response of the system in conditions of GR, a second main result of the Thesis. We performed Second-Harmonic-Generation experiments, where the giant response allows us to achieve constraint-free wavelength conversion.

Chapter 5 is an experimental and computational analysis of the ferroelectric cluster dynamics under the effect of a bias electric field. We perform, for the first time, direct cluster imaging in the volume achieved using high-resolution orthographic 3D projections based on giant refraction, identifying two distinct percolative processes that occur in the 3D volume.

Chapter 6 is an indepth structural investigation of bulk ferroelectric KTN. We observe average structure anomalies through redundant X-ray diffraction experiments, corroborated by optical diffraction, calorimetry, dielectric measurements and second harmonic generation results.

In the second part, light assumes a principal role through the study of nonlinear waves dynamics, supported by these media. The main experimental findings are presented according to the following chapters.

Chapter 7 gives an introduction to the basic physical mechanisms and methods on which the phenomena investigated rely. In particular, photorefractive and nonlinear wave equations leading to photorefractive solitons are derived, with a brief discussion on the formation of rogue waves.

Chapter 8 illustrates the use of Bessel beams to optically write patterns unaffected by diffractive distortions able to guide and route light, in the form of localized modes, through a volume. In particular the writing technique based solely on linear waves allows us to build a scalable and rewritable network of waveguides inside the bulk ferroelectric medium.

Chapter 9 reports an experimental and numerical analysis of the possible mechanism behind the formation of the soliton rogue waves. In particular, in section 9.1 we illustrate the experimental identification of soliton amplification and rectification, whereas in section 9.3 the observation of chaotic dynamics. These are basic ingredients in the physical understanding of rogue wave formation.

List of publications discussed in this Thesis

- F. Xin, F. Di Mei, L. Falsi, D. Pierangeli, A. J. Agranat and E. DelRe “Evidence of chaotic dynamics in three-soliton collisions” *Phys. Rev. Lett.* **127**, 133901 (2021).
- L. Falsi, M. Aversa, F. Di Mei, D. Pierangeli, F. Xin, A. J. Agranat and E. DelRe “Direct Observation of Fractal-Dimensional Percolation in the 3D Cluster Dynamics of a Ferroelectric Supercrystal” *Phys. Rev. Lett.* **126**, 037601 (2021).
- L. Lo Presti, J. Parravicini, R. Soave, G. Parravicini, M. Mauri, L. Loconte, F. Di Mei, L. Falsi, L. Tartara, S. Binetti, Aharon J. Agranat and E. DelRe “Observation of an exotic lattice structure in the transparent $\text{KTa}_{1-x}\text{Nb}_x\text{O}_3$ perovskite supercrystal” *Phys. Rev. B* **102**, 214110 (2020).
- L. Falsi, L. Tartara, F. Di Mei, M. Flammini, J. Parravicini, D. Pierangeli, G. Parravicini, F. Xin, P. Di Porto, A. J. Agranat and E. DelRe “Constraint-free wavelength conversion supported by giant optical refraction in a 3D perovskite supercrystal” *Commun. Mater.* **1**, 76 (2020).
- F. Xin, M. Flammini, F. Di Mei, L. Falsi, D. Pierangeli, A. J. Agranat and E. DelRe “Using Bessel Beams to Induce Optical Waveguides” *Phys. Rev. Applied* **100**, 043816 (2019).
- F. Xin, M. Flammini, F. Di Mei, L. Falsi, D. Pierangeli, A. J. Agranat and E. DelRe “Observation of extreme nonreciprocal wave amplification from single soliton-soliton collisions” *Phys. Rev. Applied* **11**, 024011 (2019).
- F. Di Mei, L. Falsi, M. Flammini, D. Pierangeli, P. Di Porto, A. J. Agranat, and E. DelRe, “Giant broadband refraction in the visible in a ferroelectric perovskite,” *Nat. Photon.* **12**, 734-738 (2018);
- M. Ferraro, D. Pierangeli, M. Flammini, G. Di Domenico, L. Falsi, F. Di Mei, A. J. Agranat and E. DelRe, “Observation of polarization-maintaining light propagation in depoled compositionally disordered ferroelectrics,” *Opt. Lett.* **42**, 3856-3859 (2017);

List of supplementary publications

- Y. Gelkop, F. Di Mei, S. Frishman, Y. Garcia, L. Falsi, G. Perepelitsa, C. Conti, E. DelRe and A. J. Agranat “Hyperbolic optics and superlensing in room-temperature KTN from self-induced k-space topological transitions”, *Nat Commun* **12**, 7241 (2021).
- F. Xin, F. Di Mei, L. Falsi, D. Pierangeli, A. J. Agranat and E. DelRe “Soliton Maxwell demons and long-tailed statistics in fluctuating optical fields” *Opt. Lett.* **45**, 648-651 (2020).

Contributions to Conferences

- Conference on Electronic Materials and Applications 2022 (EMA 2022), 19-21 January 2022, Orlando - FL, USA.
Invited speaker and session moderator. Oral contribution with title: Direct Imaging of Fractal-Dimensional Percolation in the 3D Cluster Dynamics of a Perovskite Supercrystal
- European Conference on Lasers and Electro-Optics and European Quantum Electronics Conference (CLEO/Europe-EQEC), 21-25 June 2021, Virtual meeting.
Oral contribution with title: Direct Imaging of Fractal-Dimensional Percolation in the 3D Cluster Dynamics of a Ferroelectric Super-Crystal.
- European Conference on Lasers and Electro-Optics and European Quantum Electronics Conference (CLEO/Europe-EQEC), 21-25 June 2021, Virtual meeting.
Oral contribution with title: Constraint-free wavelength conversion supported by giant refraction in a 3D perovskite Super-Crystal.
- European Conference on Lasers and Electro-Optics and European Quantum Electronics Conference (CLEO/Europe-EQEC), 23-27 June 2019, Munich, Germany.
Invited speaker. Oral contribution with title: Giant broadband refraction in the visible in a nanodisordered ferroelectric perovskite.
- European Conference on Lasers and Electro-Optics and European Quantum Electronics Conference (CLEO/Europe-EQEC), 23-27 June 2019, Munich, Germany.
Poster presenter. Poster contributions with title: Using Bessel beams to induce optical waveguides.

- Photonics & Electromagnetics Research Symposium (PIERS), 17-20 June 2019, Rome, Italy.
Oral contribution and first prize for the Best Student Paper Award, with title: Giant broadband refraction in the visible in a disordered ferroelectric perovskite.

Acknowledgments

The research contained in this thesis was carried out under the supervision of Prof. Eugenio Del Re, in collaboration with Fabrizio Di Mei, Luca Tartara, Mariano Flammini, Paolo Di Porto, Davide Pierangeli, Jacopo Parravicini, Gianbattista Parravicini, Leonardo Lo Presti, FeiFei Xin and Aharon J. Agranat. The experimental activity has been implemented in the laboratory of the Physics Department of the University of Rome "La Sapienza" (S005-S008, Fermi building) thanks to funding from grants the PRIN 2017 PELM project (Grant No. 20177PSCKT), the "Attract" project funded by the EC under Grant Agreement No. 777222, the Sapienza-Ricerca di Ateneo 2019 project, the H2020 Fet project PhoQus, and the Israel Science Foundation (Grant No. 1960/16).

Contents

Abstract	v
List of publications discussed in this Thesis	vii
Contributions to Conferences	viii
Acknowledgments	xi
1 Ferroelectric Perovskites and domain superlattice: an overview	1
1.1 General description	1
1.2 Nanodisordered ferroelectrics	5
1.2.1 Polar Nano Regions and Relaxors	5
1.2.2 Enhanced dielectric response	5
1.2.3 Anisotropic response	7
1.3 Ferroelectricity and cluster distribution	8
1.3.1 Engineered ferroelectric supercrystal	8
1.3.2 Observation of a spontaneous ferroelectric super-crystal phase	11
1.3.3 Super-crystal Model	13
I Experimental Investigation of the super-crystal phase	15
2 Evolution of the optical state of polarization below the Curie temperature	17
2.1 Polarization-maintaining light propagation in depoled nanodisordered ferroelectrics	17
2.1.1 Light Polarization in Anisotropic Media	17
2.1.2 Materials hosting the super-crystal	19
2.1.3 Stokes Parameter Measurements	19
2.1.4 Spatially Resolved Experiments	21
2.1.5 Temperature Varying Measurements	22
2.2 Ordered polar-domain configuration	23
3 Optical propagation in a super-crystal phase	25
3.1 Giant broadband refraction in the visible in a ferroelectric perovskite	25
3.1.1 Diffraction and Refraction	25
3.1.2 Experimental setup	27

3.1.3	White Light Propagation	28
3.1.4	Physical origin of Giant Refraction	30
3.1.5	Laser Light Propagation	31
3.1.6	Giant Refraction and Anisotropy	34
3.1.7	Index of refraction evaluation from diffraction	35
3.2	Broadband giant index of refraction	36
4	Nonlinear response in the super-crystal phase	37
4.1	Constraint-free wavelength conversion supported by giant optical refraction	37
4.1.1	Giant refraction Cherenkov Phase-matching	38
4.1.2	Giant refraction Cherenkov SHG	39
4.1.3	Materials and super-crystal preparation	40
4.1.4	Experimental setup and SHG conversion efficiency	41
4.1.5	3D nonlinear lattice	42
4.1.6	Cherenkov SHG Experiment	44
4.1.7	Super-crystal chromatic dispersion	45
4.1.8	Spectral and angular acceptance	46
4.1.9	Limitation caused by the Enhanced Fresnel reflection	47
4.1.10	Extreme nonlinearity	49
4.2	Future developments	49
5	Dynamics of the super-crystal phase: clustering and percolation analysis	51
5.1	Observation of Fractal-Dimensional Percolation in the 3D Cluster Dynamics	51
5.1.1	3D orthographic cross-polarizer projection	52
5.1.2	Percolation analysis	54
5.2	Self-similarity	56
5.2.1	Role of the 3D vortex structure	57
5.2.2	Effects of super-crystal breakdown on giant refraction	57
5.3	Microscopic origin of self-similarity	58
6	Characterization of bulk KTN	59
6.1	Observation of an exotic lattice structure	59
6.1.1	Experiments	59
6.1.2	Discussion of the X-ray experiments results	63
6.1.3	Origin of the anisotropic strain field	65
6.2	Role played by topological defects	69
II	Nonlinear waves in nanodisordered Ferroelectric Perovskites	71
7	Beam propagation in photorefractive media	73
7.1	Introduction	73
7.2	Photorefractive effect	74
7.2.1	Band-transport model	74

7.2.2	Self-induced space-charge field	76
7.3	Electro-optic effect in photorefractive crystals	77
7.3.1	Cumulative nature of photorefractive response	78
7.4	Nonlinear wave equation	80
7.5	Photorefractive soliton	81
7.6	Brief introduction of rogue waves	83
8	Using Bessel Beams to Induce Optical Waveguides	85
8.1	Bessel Beam	86
8.2	Guiding in a Bessel Index of refraction pattern	87
8.3	Waveguiding mechanism	88
8.3.1	Theory	88
8.3.2	Experiments	90
8.3.3	Electro-optic control	92
8.3.4	Multiple waveguides and beam-splitter	93
8.4	Reprogrammable optical networks	94
9	Soliton interactions	95
9.1	Single soliton-soliton collisions	95
9.1.1	Model	96
9.1.2	Experiments	98
9.1.3	Results	99
9.1.4	Numerical simulations	102
9.2	Microscopic rectification mechanism	104
9.3	Evidence of chaotic dynamics in three-soliton collisions	104
9.3.1	Experiments	105
9.3.2	Model	109
9.3.3	Numerical results	110
9.4	Evidence of chaotic dynamics	112
9.4.1	Applicative perspective	112
	Conclusions	113
	Bibliography	115

Ferroelectric Perovskites and domain superlattice: an overview

In this Chapter, we introduce the peculiar properties of nanodisordered ferroelectric perovskites, highlighting the role of temperature and compositional disorder, that have an important impact on the response of the system. These are then instrumental in the discussions and experiments describing the emergence of the super-crystal phase, a 3D lattice of polarization vortices, which emerge in different systems and geometries, and forms the heart of the original contribution of this Thesis.

1.1 General description

The materials that are extensively studied in this thesis are zero-cut polished solid solution of potassium-tantalate-niobate $\text{KTa}_{1-x}\text{Nb}_x\text{O}_3$ (KTN) and lithium-enriched solid solution $\text{K}_\alpha\text{Li}_{1-\alpha}\text{Ta}_\beta\text{Nb}_{1-\beta}\text{O}_3$ (KTN:Li), which belong to the class of perovskites. These are oxides with a chemical structure ABO_3 , where **A** is an alkaline metal, or a rare earth, and **B** is, in general, a transition metal. In Fig. 1.1 (a) is reported the elementary cell: there is one oxygen per each six face centres, the element **A** occupies the eight vertexes and the element **B** is placed in the center of the cube [1]. The chemical bonding is ionic with oxygens as anions and A-B as cations. Perovskites play a relevant role in optics because they are transparent ferroelectric media, dielectric or semiconductor, that manifest a strong electro-optic and nonlinear response [2–4]. Ferroelectricity is the property of materials to have a spontaneous and reorientable electric polarization. A peculiar aspect is the dependence of the crystal symmetry on temperature which sets out two main phases. Defining the Curie temperature, T_C , as the temperature of the phase transition, for temperature

$T > T_C$, the system is in the the paraelectric (disordered) phase while for $T < T_C$ is in the ferroelectric (ordered) phase [5]. The ferroelectric polar phase manifest hysteresis, for which a residual polarization persists when the external electric field is null, while in the paraelectric phase the crystal behaves like a common isotropic dielectric, e.g. without hysteresis. From a microscopic point of view, the phase transition corresponds to a structural rearrangement of the elementary cell from the centrosymmetric cubic paraelectric phase to a noncentrosymmetric orthorhombic ferroelectric phase with a non-zero dipole moment in the cell. (Fig. 1.1 (b)).

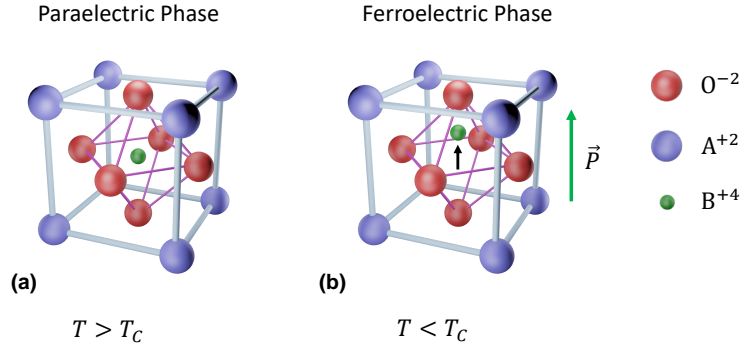


Figure 1.1. Three-dimensional structure of the perovskite unitary cell. (a) Structure for the paraelectric phase. (b) Structure for the ferroelectric phase with the displacement of the central cation that causes the spontaneous polarization \vec{P} .

Generally, the transition from a disordered phase (high temperature), compared with the order parameter, to an ordered phase (low temperature), can be described as the transition of a system with some group symmetry invariance for $T > T_C$, to another system with spontaneous symmetry breaking for $T < T_C$. These can be described using the Landau-Devonshire theory [6], where the free energy is expanded in terms of a single component of the polarization. We assume, for simplicity, that the free energy of the unpolarized, unstrained, crystal is equal to zero. Hence we can write

$$\mathcal{F} = \frac{1}{2}\alpha P^2 + \frac{1}{4}\beta P^4 + \frac{1}{6}\gamma P^6 - EP, \quad (1.1)$$

where we have truncated the power series at the sixth power term. The equilibrium configuration is determined by finding the minima of \mathcal{F} , $\frac{\partial \mathcal{F}}{\partial P} = 0$. We obtain an equation for the electric field E as a function of polarization

$$E = \alpha P + \beta P^3 + \gamma P^5 - EP. \quad (1.2)$$

To determine the dielectric susceptibility above the transition, we can differentiate Eq. (1.2) with respect to P and then setting $P = 0$, we obtain

$$\varepsilon_0 \chi_r = \left. \frac{\partial P}{\partial E} \right|_{P=0} = \frac{1}{\alpha}. \quad (1.3)$$

The Landau-Devonshire theory assumes that around the Curie point only α is temperature dependent, i.e.,

$$\alpha(T) = \frac{(T - T_C)}{\varepsilon_0 C}. \quad (1.4)$$

Substituting the expression (1.4) for α into Eq. (1.3), we find that the susceptibility χ follows the Curie-Weiss law:

$$\chi_r = \frac{C}{T - T_C}, \quad (1.5)$$

where C is a material-specific Curie constant.

The paraelectric-ferroelectric phase transition can be ascribed as both first and second order transition (according to Ehrenfest classification) depending on the sign of β [7]. For our aims, we consider the case in which $\beta > 0$, i.e. a second order phase transition. From a microscopic point of view, consider the interatomic forces acting on different ions: for example, for the B^+ ion, there is a free energy profile dependent both on position with respect to O^- ions and on temperature. In the paraelectric phase, with zero applied electric field, that potential shows a minimum corresponding to a centrosymmetric configuration of the primitive cell with zero dipole moment (Fig. 1.2, blue curve). At the critical temperature, the shape of the potential varies (Fig. 1.2, green curve), in such a way that for $T < T_C$ the symmetric position of the ion becomes a local maximum of the energy: the potential has two minima for each direction, and between them a local maximum (Fig. 1.2, orange curve).

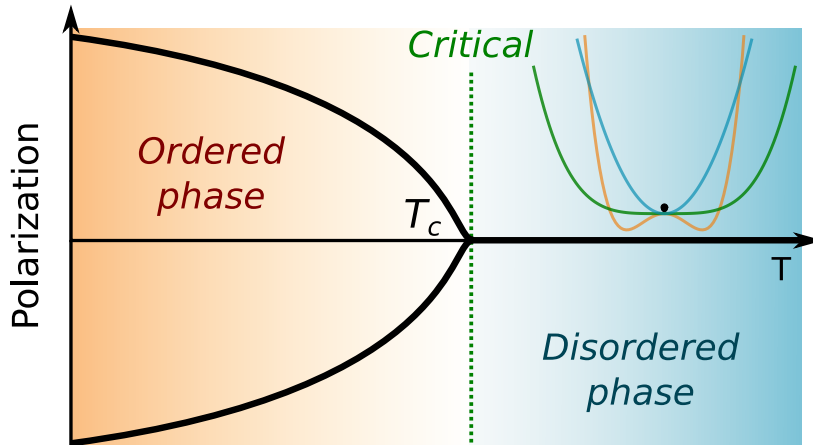


Figure 1.2. Second order phase transition. The order parameter begins to grow continuously just below the critical point. In the inset there is a representation of the free energy in the disorder phase (blue), the critical point (green) and the order phase (orange).

The B^+ ion occupies one of the possible minima with a consequent asymmetry of the charge distribution in the elementary cell that yields a local dipole momentum. Now, dipole-dipole interactions force the orientation of the dipoles in every cell of the crystal, reaching the global lowest energy configuration with all these dipoles aligned in the same direction. This process leads to the formation of ferroelectric domains, in which polarization is well defined and such that a macroscopic spontaneous polarization arises (Fig. 1.1 (b)).

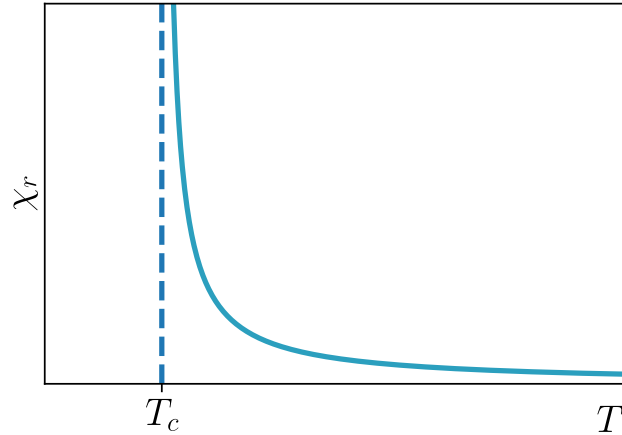


Figure 1.3. Curie-Weiss law. Electric Susceptibility χ_r as a function of temperature T exhibits a very pronounced peak approaching the transition temperature T_C .

Considering the electric susceptibility χ_r , as expected, it diverges as the temperature approaches T_C from the paraelectric phase according to Eq. (1.5). The Curie-Weiss Law (1.5) states that for $T \gg T_C$ the polarization of the system is globally zero. For $T \sim T_C$, χ_r diverges (see Fig. 1.3) and values of $\chi_r > 10^5$ are actually measured; the phenomenon is associated with the divergence of correlation length ξ , that is the system has a strong collective response. An important consequence of this is that the material, at the transition, manifest the so-called critical opalescence, i.e. a huge scattering caused by strong domain fluctuations, that do not allow light to propagate. For this reason, experiments are usually performed several degrees above T_C , as this leads to a homogeneous medium with a high χ_r [8–11]. Crystals characterized by compositional disorder such as KTN, furthermore prevent the long-range correlation of ferroelectric domains, which can be constrained to nanometric scales $\xi \ll \lambda$ even at the phase transition, allowing light propagation with no scattering. Lattice disorder, introduced by chemical substitutions in \mathbf{ABO}_3 perovskites, can furthermore lead to the formation of polar nanoregions at $T > T_C$ that influence statistical and dynamical properties of the medium [12].

Nanodisordered ferroelectrics

1.2.1

Polar Nano Regions and Relaxors

Disorder can turn an ordinary ferroelectric crystal into a relaxor ferroelectric (or relaxor), a class of disordered crystals possessing peculiar structure and properties [12, 13]. From a microscopic point of view, disorder is produced by the chemical substitutions of ions of different valences than the host ions leading to the formation of lattice defects, or substituting ions with ones different in size but with the same valence, generating an asymmetry of the cubic cell that causes a dipole moment. Relaxors have complexity. At high temperature $T \gg T_C$ relaxors behave like ordinary ferroelectrics in their non-polar paraelectric phase. Upon cooling, polar regions of nanometer scale with randomly distributed directions of dipole moments appear. This transformation, which occurs at the so-called Burns temperature (T_B) cannot be considered a structural phase transition because it is not accompanied by any change of crystal structure on the macroscopic or mesoscopic scale. Nevertheless, the polar nanoregions (PNRs) affect the behaviour of the crystal, giving rise to unique physical properties. For this reason the state of crystal at $T_C < T < T_B$ is often considered as the new phase different from the paraelectric one [13]. It is a glassy state, with randomly distributed directions of dipole moments, and non-ergodic behavior [14]. PNRs are known to form the basis for remarkable optical responses of both fundamental and technological interest, such as randomly-matched second harmonic generation [15–17], the giant photorefractive nonlinearities [18–23], giant quadratic electro-optic coefficients [2, 24–27], strong electromechanical coupling [28], and the anomalous electro-optic effect [3, 29, 30].

1.2.2

Enhanced dielectric response

A signature of this new phase is that, for $T < T_B$, the material does not follow the Curie-Weiss law (1.5) and this fact is used to define T_B itself (Fig. 1.4). As previously mentioned for ordinary ferroelectrics, at the Curie point we observe values of $\chi_r > 9 \times 10^3$. For relaxors this peak is of the same order of magnitude, but in contrast to ordinary ferroelectrics, it is highly diffused and frequency dependent. A typical behaviour of the χ_r vs T obtained through dielectric spectroscopy performed on a relaxor sample, specifically a sodium-potassium-tantalate-niobate (KNTN) crystal is reported in Fig. 1.4.

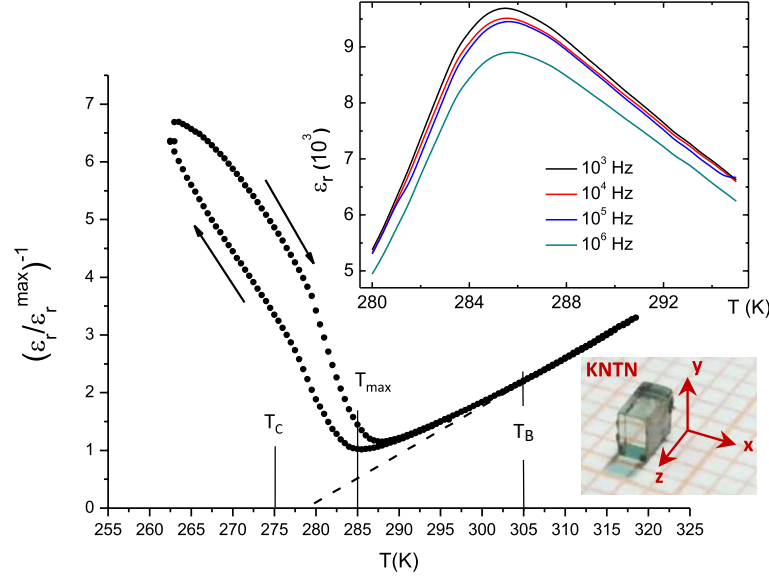


Figure 1.4. Experimental measurements of $\varepsilon_r = \chi_r + 1$ through dielectric spectroscopy for a relaxor ferroelectric KNTN. The real part of the dielectric constant manifests marked thermal hysteresis (arrows indicate cooling/ heating curves) below T_B and a breaking of Curie–Weiss law (dashed line) in the region $T_{max} < T < T_B$. The position of the temperatures T_C , T_B , T_{max} are in agreement with the definitions provided in text. In the insets, the detected dispersion in ε_r near T_{max} and a photograph of the specific KNTN sample. (Adapted from ref. [26]).

The broad phase transition makes it possible to exploit the high χ_r in the transparent paraelectric phase. However, presenting a diffused ferro-paraelectric phase-transition, a critical temperature T_C (the value estimated from the Curie law in paraelectric phase) cannot be defined easily and a glassy dynamic transition temperature T_{max} is introduced, as illustrated in Fig. 1.4. The temperature T_{max} is only approximate. As reported in the inset, measurements taken with different electric field frequencies change the peak χ_r value and the actual T_{max} . This phenomenon is described by the Vogel-Fulcher law (VF):

$$f = (2\pi\tau_0)^{-1} e^{\frac{-E_a}{k_B(T-T_{VF})}}, \quad (1.6)$$

where f is the measurement frequency and τ_0 , E_a and T_{VF} are fitting parameters [31]. The VF law is well known in spin glasses. When revealed in relaxors, it became one of the main reasons to postulate the existence of a dipole glass phase at $T < T_{VF}$ [13]. Moreover, Eq. (1.6) can imply a similar relation for typical time scales of dipole relaxation processes: the dipole relaxation time τ is strongly temperature dependent and the modified Arrhenius law holds [13]

$$\tau = \tau_\infty e^{\frac{E_b}{k_B(T-T_f)}} \quad (1.7)$$

where τ_∞ and E_b are parameters and T_f is the so-called freezing temperature [13], with $T_C \lesssim T_f < T_B$, that is the temperature under which the ergodic regime ceases

and PNRs remain in a frozen state. Eq. (1.7) establishes that τ grows when $T \sim T_f$ and diverges for $T = T_f$. This means that the system at $T < T_f$ cannot reach an equilibrium state, and remains in a metastable state. We remark that this metastable state is not always the same but is correlated with the previous history of the sample, i.e. thermal cycles, electric field application or observation time. A direct consequence of this is, in Fig. 1.4, the existence of a thermal hysteresis loop, that is, different values of χ_r are obtained in cooling and in heating. We note that although Eq. (1.6) and Eq. (1.7) have a similar structure, the connection between them is not straightforward and still debated [13]. A percolation mechanism of PNRs has been proposed to derived Vogel-Fulcher equation for the temperature dependence of τ [32, 33].

1.2.3

Anisotropic response

A last noteworthy feature of many relaxors is their peculiar anisotropic response, that is, different behaviors for fields applied along the three crystalline axes. An example of this is reported in Fig. 1.5, here the dielectric spectroscopy of a KNTN crystal shows directional anisotropy also in the nominally cubic phase. These observations are attributed to the alteration of polarization and internal strain induced during the sample growth. Moreover, the slightly different transition temperature is associated to a hysteretic effect [34].

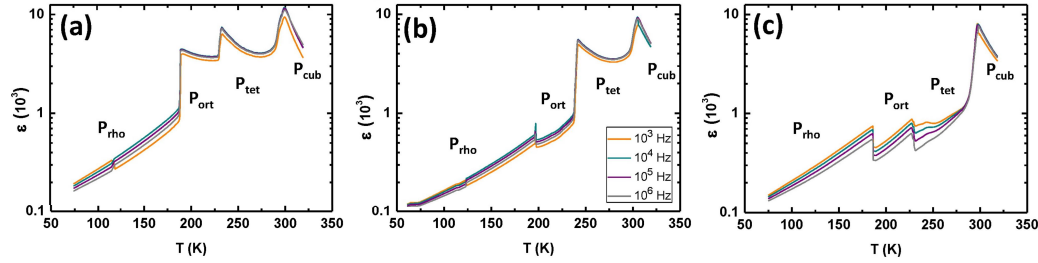


Figure 1.5. Relative permittivity as function of the measured temperature for several electric field frequencies (we recall that $\varepsilon_r = \chi_r + 1$). The experiment is performed during the heating stage along the three crystalline axes: *a* (a), *b* (b) and *c* (c). (Adapted from ref. [34]).

1.3

Ferroelectricity and cluster distribution

Textbook models of global symmetry-breaking include a low-symmetry low-temperature state with a fixed infinitely extended coherence. In contrast, the spontaneous polarization observed as spatial inversion symmetry that is broken during a paraelectric-ferroelectric phase transition generally leads to a disordered mosaic of polar domains that permeate the finite samples [6]. Coherent and ordered ferroelectric states with remarkable properties of both fundamental and technological interest [35–38] can emerge when ferroelectricity is influenced by external factors, such as system dimensionality [39], strain gradients [40–42], and electrostatic coupling [43, 44].

1.3.1

Engineered ferroelectric supercrystal

Multiaxial ferroelectrics are especially responsive to strain. These naturally self-organize into ordered domain structures over a wide range of length scales [45]. Domain walls in these materials bring new macroscopic functionality to ultrathin films, where extremely high domain wall densities can be generated [46]. When artificially confined electrostatically in superlattice geometries, strained ultrathin ferroelectrics can exhibit unusual polarization textures, such as flux-closure patterns and polar vortices. The response of such systems to applied fields may lead to greatly enhanced susceptibilities and unusual behaviour, including a negative capacitance [47, 48]. Domain structures with similar energies can give rise to the coexistence of different polarization textures and their interconversion on electrical, mechanical or optical stimulation, as has recently been explored in ferroelectric-dielectric $\text{PbTiO}_3\text{-SrTiO}_3$ (PTO/STO) superlattices [49]. An optically induced supercrystal phase arises when the heterostructure is illuminated with light above the bandgap i.e., with a λ that allows direct absorption [49]. Here the system grown on DyScO_3 substrates, is initially a two-phase mixture of ferroelectric-ferroelastic domains (FE) and polarization vortices (V) (see Fig. 1.6 (a)).

Using a sub-picosecond optical pulse excitation, the electrostatic landscape is manipulated with a reduction of the depolarizing field via photocarrier excitation, enabling the formation of a stable structure with long-range nanoscale polar order consisting of polar vortices that are meshed in three dimensions (Fig. 1.6 (b)). Both phases were experimentally mapped using X-ray scattering. The results show the two superlattice reflections of the pristine state collapse into a single vertical superlattice reflection (Fig. 1.6 (c)), with the simultaneous appearance of strong peaks in the off-specular part of the spectrum resulting from a fully coherent 3D modulation of the lattice with a well-defined periodicity of approximately $30\text{nm} \times 25\text{nm}$ in the $y\text{-}z$ plane. This phase captures and stores the light-activated carriers in a highly 3D charge-ordered state, which could be a potential strategy for charge storage and highly tunable capacitors. A different supercrystal phase has been observed in

metal-ferroelectric superlattices consisting of alternating layers of PbTiO_3 and a correlated metal SrRuO_3 without the need for optical excitation [50].

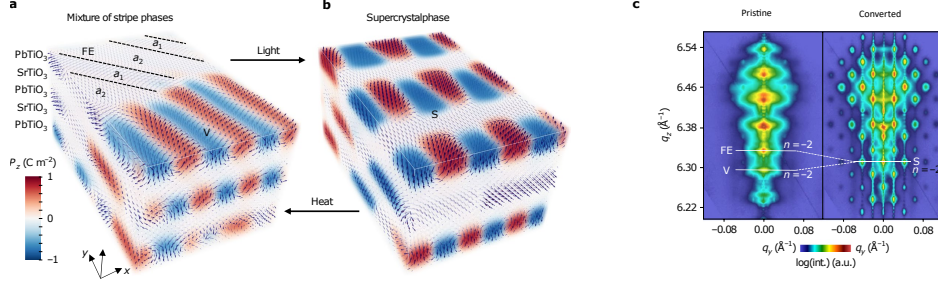


Figure 1.6. (a)-(b) Supercrystal formation. A two-phase mixture of in-plane ferroelectric-ferroelastic and polar vortex (a) is converted to a single 3D supercrystal phase by sub-picosecond optical pulses in a PTO/STO superlattice (b). Thermal annealing reverses this transition. (c) Supercrystal observation by X-ray diffraction. Diffraction along the q_y - q_z plane near the 004_{pc} peak for the mixed phase shows evidence of order only along the z direction, with distinct peaks due to the FE and V phases, as noted by the horizontal lines (Pristine). Upon optical excitation with light above the PTO bandgap, a periodic two-dimensional diffraction pattern appears due to spatial ordering in the y - z plane (Converted). (Adapted from Ref. [49]).

Synchrotron three-dimensional reciprocal space mapping reveals a diffraction pattern corresponding to a highly ordered 3D domain structure with an in-plane periodicity of 26 nm that is and an out-of-plane period of 12.7 nm (see Fig. 1.7 (a)-(c)). In this case, the observed 3D domain structure consist in vertical and flux-closure components (Fig. 1.7 (d)). Here a PbTiO_3 - SrRuO_3 superlattice is deposited on DyScO_3 substrates and elasticity will favour the ferroelastic domain formation, with a and c domains running through the entire thickness of the multilayer. The conductive layers introduce a depolarizing field, as even structurally perfect SrRuO_3 - PbTiO_3 interfaces have a finite screening length. Thus, the imperfect screening at the interfaces in PbTiO_3 - SrRuO_3 superlattices lead to energetically costly depolarizing fields within the PbTiO_3 layers, forcing the PbTiO_3 layers to split into vertical and horizontal flux-closure domains to eliminate the macroscopic polarization and reduce the electrostatic energy. For the vertical and horizontal flux-closure structures observed in this work, this requires the ferroelectric layer to be sufficiently thick. For thinner PbTiO_3 layers with finer domain periods such structures become increasingly less favourable, in part due to the increased energy cost associated with the many domain walls, and therefore other polarization configurations may appear.

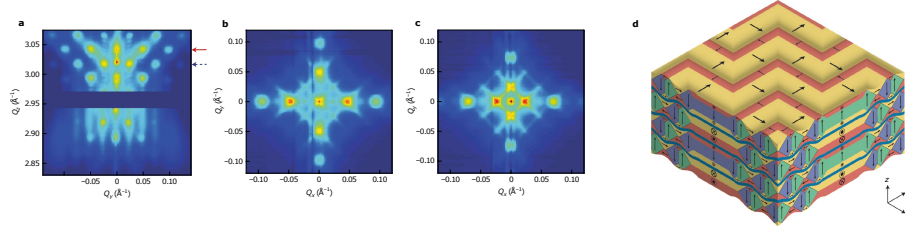


Figure 1.7. (a-c) Reciprocal space view of the 3D domain structure. (a) Synchrotron XRD reciprocal space map in the Q_y - Q_z plane around the 002_{pc} (220_o) substrate reflection for a PTO_{27} - SRO_5 superlattice showing the periodic satellite peaks arising from a highly ordered domain lattice with long-range coherence along the $[001]_{pc}$ direction. (b), (c), 2D cuts through reciprocal space in the $Q_z = 3.042 \text{ \AA}$ (b) and $Q_z = 3.017 \text{ \AA}$ (c) planes detailing the arrangement of in-plane and out-of-plane ordering, the long-range coherence of the domains along $\langle 100 \rangle_{pc}$ and the streaky diffuse scatter along $\langle 110 \rangle_{pc}$. (d) A 3D sketch of the overall domain pattern deduced from XRD, PFM and TEM studies (not reported in this thesis). (Adapted from Ref. [50]).

A different scenario emerges in the nominal ferroelectric phase of specifically grown potassium-lithium-tantalate-niobate (KLTN) crystal [9]. Here an extended coherent three-dimensional (3D) superlattice spontaneously forms, few degrees below the Curie point [51]. Visible light propagation reveals a polarization pattern with a micrometric lattice constant, a counterintuitive mesoscopic phase that naturally mimics standard solid-state structures but on scales that are thousands of times larger. The phenomenon is achieved using compositionally disordered ferroelectrics. At one given temperature, these have the interesting property of manifesting a single perovskite phase whose dielectric properties depend on the specific composition. A compositional gradient along the pull axis leads to a position-dependent Curie point $T_C(\mathbf{r})$, so that for a given value of crystal temperature T a phase separation occurs, where regions with $T > T_C$ are paraelectric and those with $T < T_C$ have a spontaneous polarization. Specifically tailored growth schemes are even able to achieve an oscillating T_C along a given direction. Under these conditions, we can expect that, at a given T in proximity of the average (macroscopic) T_C , the sample will be in a hybrid state with alternating regions with and without spontaneous polarization. Crossing the Curie point, under conditions in which perovskite polar domains pervade the volume forming 90° configurations to minimize the free energy associated with polarization charge, this oscillation can form a full 3D periodic structure. In the next section we illustrate the first observation of the super-crystal phase (SC) in KLTN and the first model proposed.

1.3.2

Observation of a spontaneous ferroelectric super-crystal phase

The experiment was conducted using a KLTN sample with a periodically oscillating niobium composition of period $\Lambda = 5.5 \mu\text{m}$ along the x axis (see Figs. 1.8 (a)-(d)). When the crystal is kept at $T = T_C - 2 \text{ K}$, i.e., in proximity of the spatially averaged room-temperature Curie point $T_C = 294 \text{ K}$, laser light propagating through the sample suffers relevant scattering with strongly anisotropic features.

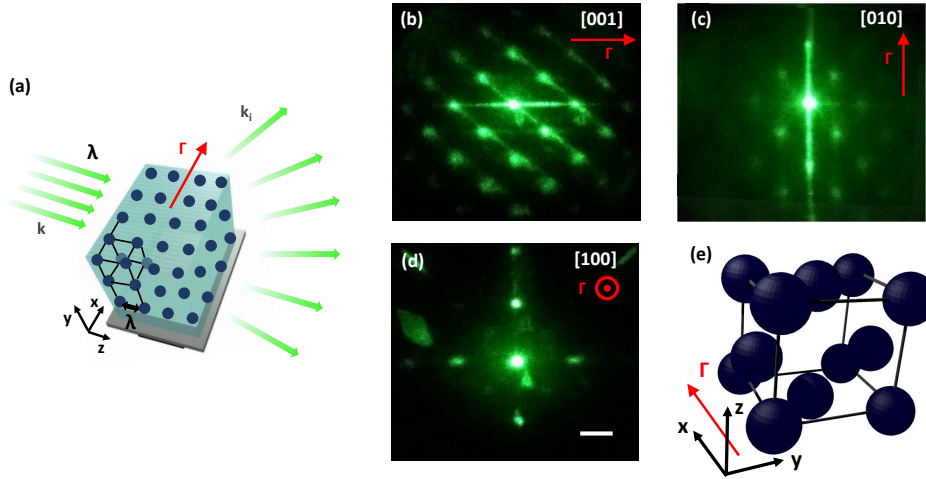


Figure 1.8. Super-crystal phase. (a) Sketch of visible-light diffraction from micrometric structures through a periodic KLTN. (b-d) 3D superlattice probed at $T = T_C - 2 \text{ K}$ along the principal symmetry direction of the crystal. (e) Crystallographic analysis reveals the elementary cubic structure of lattice constant Λ shown. Scale bar, 1.2 cm. (From Ref. [51]).

Typical results are reported in Fig. 1.8 (b)-(d), and appear as an optical analogue of X-ray diffraction in low-temperature solids. This optical diffractometry provides basic evidence of the 3D SC at micrometric scales. Probing the principal crystal directions reveals several diffraction orders that map the entire reciprocal space. The large-scale SC, that permeates the whole sample, overlaps along the x -direction with the built-in compositional oscillating seed. The SC extends in full three-dimensions, with the same periodicity $\Lambda = 5.5 \mu\text{m}$ of the x -oriented compositional oscillation, also along the orthogonal y and z -directions. In particular, Fig. 1.8 (d) indicates that in the plane perpendicular to the built-in dielectric microstructure Γ vector, i.e., where spatial symmetry should be unaffected by the microstructure in composition, the ferroelectric phase-transition leads to a spontaneous pattern of transverse scale Λ . The corresponding elementary structure on micrometric spatial scales is reported in Fig. 1.8 (e); it can be represented as an fcc-cubic structure in which the occupation of one of the three faces ($z - y$ face) is missing [52]. The structure can be reduced to a simple cubic structure with a three-fold basis and lattice parameter $a = \Lambda$.

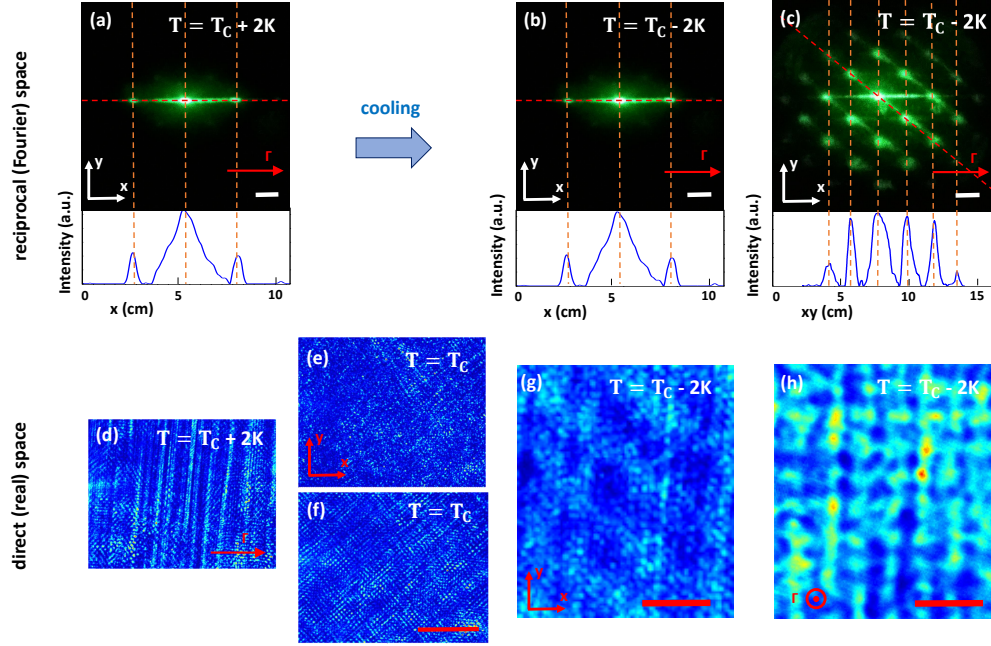


Figure 1.9. Light diffraction above and below T_C . (a) Reciprocal space probed at $T = T_C + 2$ K (hot paraelectric phase), showing the first diffraction orders due to the one-dimensional sinusoidal compositional modulation. Cooling below the critical point results at $T = T_C - 2$ K (super-crystal ferroelectric phase) in (b) a supercooled (metastable) 1D superlattice with the same diffraction orders that relaxes at the steady state into (c) the cold (stable) super-crystals. In both (b, c) the direction of incident light is orthogonal to Γ , as in (a). (d–h) Corresponding transmission microscopy images revealing (d) unscattered optical propagation, (e, f) scattering at the phase transition, (g) unscattered optical propagation in the metastable superlattice and (h) periodic intensity distribution underlining the 3D superlattice. Metastable and stable (equilibrium) phases are inspected, respectively, at times $t \approx 1$ min and $t \approx 1$ h after the structural transition at $T = T_C$. Bottom profiles in a–c are extracted along the red dotted line. Scale bars (a–c), 1.2 cm, (d–f), 100 μm and (g, h), 10 μm . (From Ref. [51]).

As the crystal is brought below the average Curie point, it manifests a metastable (supercooled) and a stable (cold) phase, as analyzed in Fig. 1.9 both in the reciprocal (Fourier) and direct (real) space. In the nominal paraelectric phase, at $T = T_C + 2$ K (Fig. 1.9 (a)), we observe the first Bragg diffraction orders (± 1) consistent with the presence of the seed microstructure, a one-dimensional transverse sinusoidal modulation acting as a diffraction grating; the distance from the central 0-order fulfils the Bragg condition, that is, scattered light forms an angle $\theta_B = \lambda/2n_0\Lambda \simeq 7^\circ$ with the incident wavevector \mathbf{k} . Crossing the ferroelectric phase-transition temperature T_C we detect a supercooled metastable state that has an apparently analogous diffraction effect (Fig. 1.9 (b)) that is dynamically superseded by the stable and coherent cold SC phase (see Fig. 1.9 (c)), in which spatial correlations are extended to the whole crystal volume. In real space, transmission microscopy shows unscattered optical propagation through the paraelectric sample at $T = T_C + 2$ K (Fig. 1.9 (d)), that

turns into critical opalescence and scattering from oblique random domains at the structural phase transition (Fig. 1.9 (e)-(f)), and in unscattered transmission in the metastable ferroelectric phase at $T = T_C - 2$ K (Fig. 1.9 (g)). After dipolar relaxation has taken place, the cold SC appears in this case as a periodic intensity distribution on micrometric scales, as shown in Fig. 1.9 (h).

1.3.3

Super-crystal Model

In standard perovskites, equilibrium configurations are mainly those involving a 180° and 90° orientation between adjacent polar domains, as schematically shown in Fig. 1.10 (a).

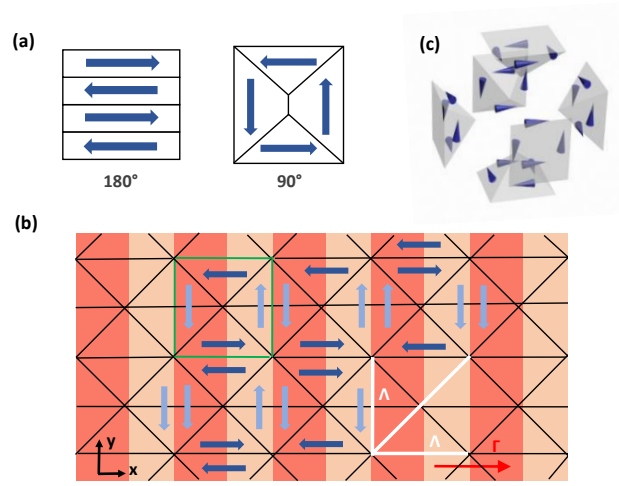


Figure 1.10. Polar-domain configuration underlying the 3D superlattice. (a) Typical 180° and 90° domain configurations in perovskites ferroelectrics. (b) Planar domain arrangement scheme in the stable super-crystal phase obtained with elementary blocks of 90° configurations (green cell). In this periodically-ordered ferroelectric state the compositional modulation, other domain walls ruling optical diffractometry (black lines), and periods along x, y and xy -axis (white bars) are highlighted. Vertical polarizations have a lighter color to stress their weak optical response in our KLTN sample. (c) Extension of the single unit-cell (green cell in (b)) in three dimensions. (From Ref. [51]).

To explain the 3D polar-state and its periodical features underlying the SC, we consider the 90° configuration, which is characterized by 45° domain walls that we observe in a disordered configuration during the ferroelectric phase transition at T_C (Fig. 1.9 (f)). Due to the periodic constraint along the x -axis, this arrangement has the unique property of reproducing our observations, minimizing energy associated to internal charge-density, and transferring the built-in 1D order to the whole volume with the same spatial scale Λ . We illustrate the domain pattern in Fig. 1.10 (b) for the $x - y$ plane, whereas in Fig. 1.10 (c) the elementary cell is shown

in the three-dimensional case, where it maintains its stability features in terms of charge-density energy. In particular, in Fig. 1.10 (b), domain walls resulting in the diffraction orders of Fig. 1.8 (b) are marked, as well as the 45° correlation period, that agree with optical observations of the reciprocal space. We further stress that vertical domains (light blue in Fig. 1.10 (b)) are optically analogous to paraelectric regions; moreover, 180° rotations in the polarization direction in each polar region has no effect on the optical response. In view of the symmetry of this arrangement, the observed diffraction anisotropy (Fig. 1.8 (d)) is then associated to the absence of grating-planes in the $y - z$ face. So the effect of the composition profile is here crucial in triggering the spontaneous formation of the macroscopic coherent structure, as it sets the typical domain size along the x direction and so rules the whole dynamic towards the equilibrium state. A different amplitude and period of the modulation may affect the formation, stability, time and temperature dynamics of the super-crystal; indeed, the parameters of the compositional gradient may be important in determining the interaction between polar regions. The effect not only opens new avenues in the optical exploration of critical properties and large-scale structures in disordered systems, but also suggests methods to predict and engineer new states of matter. It can also have an impact on the development of innovative technologies, such as nonvolatile electronic and optical structured memories [35–37], microstructured piezo devices and spatially resolved miniaturized electro-optic devices [29, 53, 54].

Part I

Experimental Investigation
of the super-crystal phase

Evolution of the optical state of polarization below the Curie temperature

In this Chapter we experimentally investigate the super-crystal phase studying the evolution of the optical polarization state through the measurements of both global and local Stokes parameters, varying the input light polarization and the temperature. Results indicate that, in contrast to pure depoled ferroelectrics, light propagates fully polarized for a linear polarization along the super-crystal principal axes. This analysis sheds light on the proprieties of the underlying ferroelectric domains.

2.1

Polarization-maintaining light propagation in depoled nanodisordered ferroelectrics

2.1.1

Light Polarization in Anisotropic Media

The polarization of light is strongly affected by anisotropy, the paradigm being the birefringence observed in non-centrosymmetric crystals, such as ferroelectrics [6], where the index of refraction depends on the polarization and propagation direction. In a full three-dimensional scenario, birefringence can also affect wave propagation, not only introducing coherent scattering [55], but even engendering localized guided modes. More exotic polarization phenomena can be observed in systems where the anisotropy emerges on periodic structures, as occurs in metamaterials [56–59], in periodically-poled multiferroic media [60] and in organic ferroelectrics [61]. Elaborate anisotropic states are also found in nanodisordered ferroelectrics in proximity of the

Curie point, signaling the paraelectric-ferroelectric phase transition, where polar nanoregions (PNRs) emerge. Polar nanoregions, in relaxor materials, generally form a disordered three-dimensional mosaic for which optical birefringence experiments indicate average local symmetry breaking, providing a tool for the study of possible non-ergodic behavior and dipolar-glass dielectric relaxation [62–65]. In turn, the presence of large polar domains below the Curie point or in the paraelectric phase under high electric field [24], causes complete depolarization of propagating optical fields, a result of multiple interference of random scattered waves. As discussed in Chapter 1.3.2, conditions have been found in which the polar nanoregion mosaic spontaneously settles into a three-dimensional coherent and periodic structure, a ferroelectric super-crystal (SC) with intriguing optical diffraction properties [51]. A question naturally arises: how is optical polarization affected by a SC? Polarimetric experiments indicate that, in distinction to pure depoled ferroelectrics, light propagates fully polarized for a linear polarization along the SC principal axes.

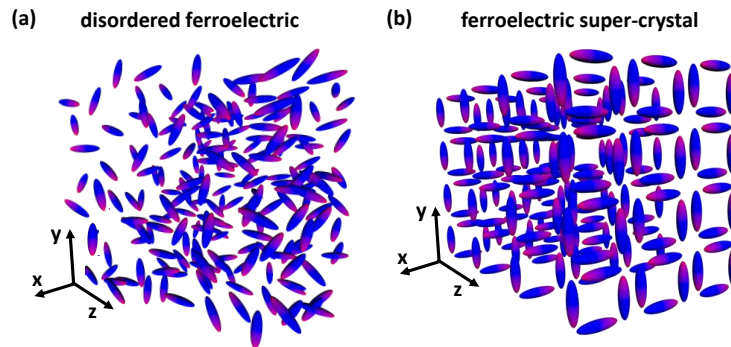


Figure 2.1. Schematic of different spontaneous ferroelectric states. (a) Three-dimensional disordered distribution of polar domains. (b) Example of a volume polar structure underlying a ferroelectric SC.

Analyzing the wave spatial distribution, we found the effect to be associated with the formation of speckle distributions of alternating orthogonally polarized states that spatially separate the input polarization into its linear polarization components parallel to the principal SC axes. Precursors of the phenomenon are observed also above the Curie point, where the ferroelectric SC vanishes, thus indicating preferred orientations of polar-nanoregions. To grasp the physics underlying the polarization dynamics reported, we note that a three-dimensional disordered mosaic of anisotropic domains, as schematically shown in Fig. 2.1 (a), dephases the components of an incident optical field according to the local random optical axis, so as to scatter and depolarize the transmitted light irrespective of its input polarization state. In turn, an ordered volume pattern of polar domains, such as the one encountered in a ferroelectric SC and illustrated in Fig. 2.1 (b), where each lattice cell may host a so-called Kittel-like vortex [51], leads to a qualitatively different polarization evolution. In fact, in this case ferroelectric anisotropy is inhomogeneous but the local optical axis is on average aligned along the SC structure.

2.1.2

Materials hosting the super-crystal

In our experiments we used SC formed in two different composite ferroelectrics to demonstrate the generality of the polarization-maintaining scenario. The sodium-potassium-tantalate-niobate (KNTN) super-crystal was obtained allowing a $\text{K}_\alpha\text{Na}_{1-\alpha}\text{Ta}_\beta\text{Nb}_{1-\beta}\text{O}_3$ ($\alpha = 0.85$, $\beta = 0.63$) solid-solution crystal to equilibrate for approximately 30 minutes below its ferroelectric-paraelectric Curie point $T = T_c - 3$ K, with $T_c = 293.5$ K. The crystal is grown through the top-seeded solution method by extracting a zero-cut optical-quality 2.1 mm by 2.5 mm by 2.6 mm specimen (along the x,y,z axes). The lithium-potassium-tantalate-niobate (KLTN) super-crystal emerged from the equilibration of a 2.4 mm by 2.0 mm by 1.58 mm $\text{K}_\alpha\text{Li}_{1-\alpha}\text{Ta}_\beta\text{Nb}_{1-\beta}\text{O}_3$ ($\alpha = 0.96$, $\beta = 0.62$) with $T_c = 294$ K. Dielectric response for both samples is detailed in Refs. [34, 66] and the super-crystal formation process is reported in Ref. [51].

2.1.3

Stokes Parameter Measurements

Polarization evolution in ferroelectric SC is investigated through conventional Stokes parameter measurements [67, 68], performed using the setup shown in Fig. 2.2.

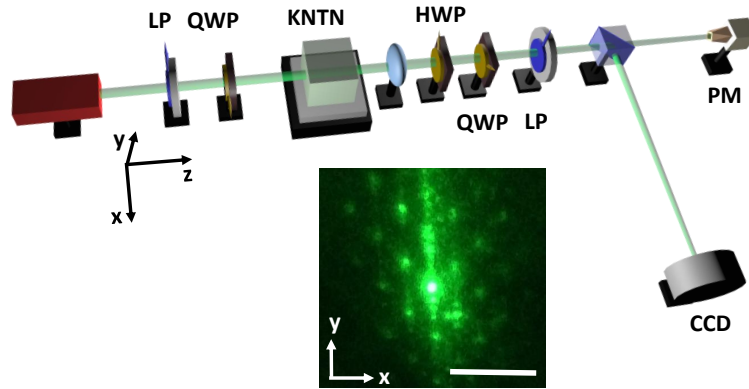


Figure 2.2. Sketch of the experimental setup: linear polarizer (LP), quarter-wave plate (QWP), half-wave plate (HWP), power meter (PM) and imaging camera (CCD). The inset shows the optical diffraction pattern observed for the KNTN super-crystal: discrete spots fill the Fourier space and signal a periodic micrometric order on large scales ($\approx 25 \mu\text{m}$) in the sample volume. Scale bar is 5 mm.

A beam from a Nd:Yag laser ($\lambda = 532$ nm, 150 mW) is expanded so as to form a plane wave propagating along the z direction and whose input polarization state is fixed using a linear polarizer and a half-wave plate. The output polarization state is analyzed using a half-wave plate, quarter-wave plate, and a linear polarizer placed after the sample. This allows the decomposition of the field into its Stokes

components, i.e., horizontal (parallel to the x axis) S_H , 45 degrees S_{45} and right-circular S_R from the optical intensity detected through a power meter and a CCD camera. Results for the KNTN SC are reported in Fig. 2.3 varying the input polarization state along different trajectories on the Poincaré sphere. In Fig. 2.3 (a) is shown the behavior of a linear polarization; the degree of polarization $\nu = \sqrt{S_H^2 + S_{45}^2 + S_R^2}$ is observed to strongly depend on the polarization direction θ of the field.

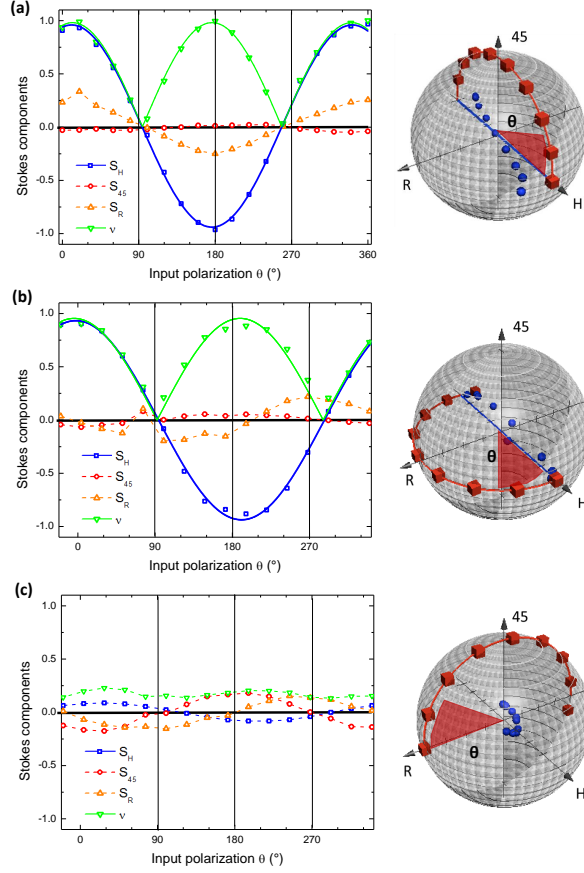


Figure 2.3. Light-polarization dynamics in the KNTN SC. (a-c) Stokes parameters measured varying the input polarization state along equators of the Poincaré sphere through the angular coordinate θ . Blue squares indicate the horizontal component of the polarization, red circles the 45° one, orange and green triangles are, respectively, the right-handed part and the degree of polarization ν . Solid lines are fitting functions (see main text) and dashed lines serves as guides. Insets show the corresponding input (red cubes) and output (blue spheres) states in the Poincaré space.

In particular, light remains fully polarized and ν is maximum for a field parallel to the x or y axis ($\theta \simeq 0^\circ, 180^\circ$), whereas complete depolarization occurs in the conjugate points ($\theta \simeq 90^\circ, 270^\circ$). For intermediate values of θ , evolution of the horizontal component is well fitted by $S_H(\theta) = \cos \theta$ (blue line in Fig. 2.3 (a, b)). Moreover, the transmitted light maintains a polarized fraction that almost coincides

with S_H , that is, $\nu(\theta) = |\cos \theta|$ (green line in Fig. 2.3 (a, b)). An analogous evolution is observed for an elliptical input state oriented along the x axis (Fig. 2.3 (b)). In this case, the circular components completely depolarize whereas the linear horizontal and vertical ones propagate unaffected in the spatially inhomogeneous ferroelectric structure. Moreover, the output field is always depolarized ($\nu \simeq 0$) along a trajectory on the Poincaré sphere orthogonal to the H axis (Fig. 2.3 (c)). The whole picture is observed in both SC, is found to be independent of the laser wavelength (532-633 nm) and crystal orientation, and occurs equally for light propagating along the x and y directions of the sample. This suggest a strong connection between the observed depolarization and the one reported in electro-optic experiments in similar crystals in proximity of T_C under large electric field [2, 23, 24, 26], an effect that has been only partially understood.

2.1.4

Spatially Resolved Experiments

To pinpoint the underlying mechanism we perform spatially-resolved Stokes parameter maps of the transmitted light. In Fig. 2.4 (a) we report the detected S_H for the significant case of a linearly polarized ($\theta = 90^\circ$ in Fig. 2.3 (a)) input wave from a He-Ne laser ($\lambda = 633$ nm, 15 mW) propagating along the z direction of the KLTN SC. We observe a speckle-like distribution arising from scattering during propagation. However, in contrast to what is expected for depolarized light from scattering, speckles distribute on a periodic lattice with approximately $6 \mu\text{m}$ lattice constant that coincides with the super-crystal structure.

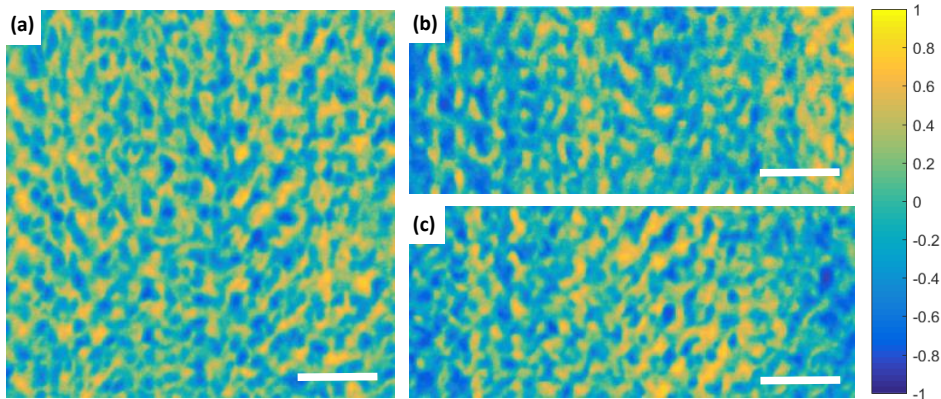


Figure 2.4. Evidence of a locally-polarized speckle lattice. Stokes parameter maps showing the transmitted (a) S_H (b) S_{45} and (c) S_R local components for a linear input polarization with $\theta = 90^\circ$. Scale bar is $20 \mu\text{m}$.

A similar speckle lattice is found for the S_{45} and S_R map, Fig. 2.4 (b) and Fig. 2.4 (c), respectively. Interestingly, while the global degree of polarization is $\nu \simeq 0$, the degree of polarization measured averaging on each spatial point is $\nu \simeq 0.7$. Therefore, the output polarization state consists of a mixture of spatially-separated polarized states. This indicates how inhomogeneity of the medium introduces a local

phase difference between orthogonal polarization components that strongly varies in space. A macroscopic Stokes measure (Fig. 2.2) averages out these local phases so that the field appears as depolarized although horizontal and vertical components are maintained during propagation. The optical polarization lattice closely follows the SC, and this demonstrate a principal role played by the underlying ferroelectric state (see Fig. 2.1 (b)).

2.1.5

Temperature Varying Measurements

To further test the role of ferroelectric domains, we perform polarimetric transmission experiments varying the crystal temperature, so as to introduce strong fluctuations in SC order, ultimately crossing the Curie temperature to restore global inversion symmetry in the paraelectric phase.

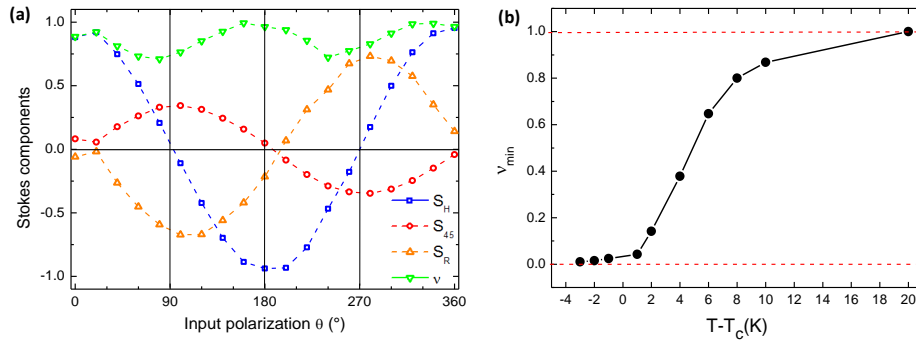


Figure 2.5. Partial depolarization from polar-nanoregions. (a) Stokes parameters measured in the nominal paraelectric phase ($T = T_C + 6$ K) for propagation along the x direction of the KNTN crystal. Inputs are linearly polarized, that is, θ varies along the equator of the sphere in Fig. 2.3 (a). (b) Minimum degree of polarization ν_{min} for measurements as in (a) versus $T - T_C$.

As reported in Fig. 2.5 (a) for the dynamics of a linearly polarized input state in KNTN (see Fig. 2.3 (a) for a comparison), the average depolarization of the input wave appears less pronounced at $T = T_C + 6$ K. Although ν still depends on θ , its minimum at $\theta \approx 90^\circ$ no longer vanishes. Although the main Stokes component remains S_H , other components become significant. Polarization evolution now is found to depend on the length of the sample along the propagation axis and on λ , suggesting a macroscopic birefringence of the hosting paraelectric medium. This is consistent with the fact that above the Curie point the super-crystal is superseded by a disordered distribution of PNRs [3, 27–30] that acts as a precursor of the macroscopic phase transition, so that no macroscopic index of refraction periodic lattice emerges. As reported in Fig. 2.5 (b), the corresponding minimum degree of polarization (ν_{min}) increases as temperature moves away from the critical point, an order parameter further underlining the role of the ferroelectric inhomogeneous structure. At $T = T_C + 20$ K, where the crystal appears no longer affected by polar-nanoregions (proper paraelectric phase), $\nu = 1$ for all input polarizations.

Ordered polar-domain configuration

In conditions for which an ordered three-dimensional polar-lattice is embedded in the material, the interplay between ferroelectric anisotropy and inhomogeneity leads to a new scenario in which the propagating wave can maintain its degree of polarization. Specifically, the field is separated into its linearly polarized components parallel to the SC principal axes in the form of two spatially distinct periodic speckle patterns. Experiments above the Curie temperature, then, suggest that polar nanoregions have preferred orientations along the crystal axes, a fact that may play a crucial role in phenomena involving the giant electro-optic and giant piezoelectric effect. Our results demonstrate how ordered polar domains can coherently modify the polarization of light, possibly enabling the use of the unconventional ferroelectric properties in photonic applications based on polarization control.

Optical propagation in a super-crystal phase

In principle, materials with a broadband giant index of refraction (e.g., $n > 10$ in the visible) overcome chromatic aberration and shrink the diffraction limit down to the nanoscale, allowing new opportunities for nanoscopic imaging [69]. They also open new avenues for the management of light to improve the performance of photovoltaic cells [70]. Recent advances have demonstrated the feasibility of a giant refractive index in metamaterials at microwave and THz frequencies [71, 72], however, the highest reported broadband index of refraction in the visible is $n < 5$ [73]. In this Chapter, we report a ferroelectric perovskite with an index of refraction $n > 26$ across the entire visible spectrum and demonstrate its behaviour using white-light and laser refraction and diffraction experiments. The sample, has a natural-occurring room temperature phase that propagates visible light along its normal axis without significant diffraction or chromatic dispersion, irrespective of beam size, intensity, and angle of incidence.

3.1

Giant broadband refraction in the visible in a ferroelectric perovskite

3.1.1

Diffraction and Refraction

In conditions of validity of the macroscopic Maxwell Equations, the optical electric field \mathbf{E} obeys $\nabla^2 \mathbf{E} - (n/c)^2 \partial_{tt} \mathbf{E} = 0$, where n is the wavelength-dependent index of refraction of the material and c the speed of light. Light entering a material with index of refraction n suffers refraction according to Snell's law, i.e., $\sin \theta_1 = n \sin \theta_2$, where θ_1 and θ_2 are the angles formed by the beam with the normal to the boundary

of the material. Once inside the material, diffraction causes the beam to have an angular spread $\Delta\theta \propto \lambda/nw_0$, where λ is the wavelength and w_0 is the input size of the beam, and this limits the spatial resolution of transmitted waveforms. Since n is wavelength-dependent, both refraction and diffraction are chromatic, i.e., different wavelengths follow different paths (chromatic aberration) and have a different angular spread. A giant refraction (GR) with $n \gg 1$ across the visible spectrum implies that refracted beams propagate along the normal to the material boundary, with a vanishing $\theta_2 = \sin^{-1}((1/n)\sin\theta_1)$, and a vanishing chromatic aberration $d\theta_2/d\lambda \simeq -\sin\theta_1(1/n)^2(dn/d\lambda)$. Furthermore, since each spectral component of wavelength λ obeys a different Helmholtz Equation $\nabla^2\mathbf{E}_\lambda + (k_0n(\lambda))^2\mathbf{E}_\lambda = 0$ [74], where $k_0 = 2\pi/\lambda = \omega/c$ and ω is the corresponding angular frequency, each plane-wave component of wave-vector \mathbf{k} obeys $k_x^2 + k_y^2 + k_z^2 = k_0^2n^2$. Angled components with $k_x, k_y \neq 0$, fixed by their values outside the material, manifest a different phase-velocity along the propagation axis $k_z = \sqrt{k_0^2n^2 - k_x^2 - k_y^2}$.

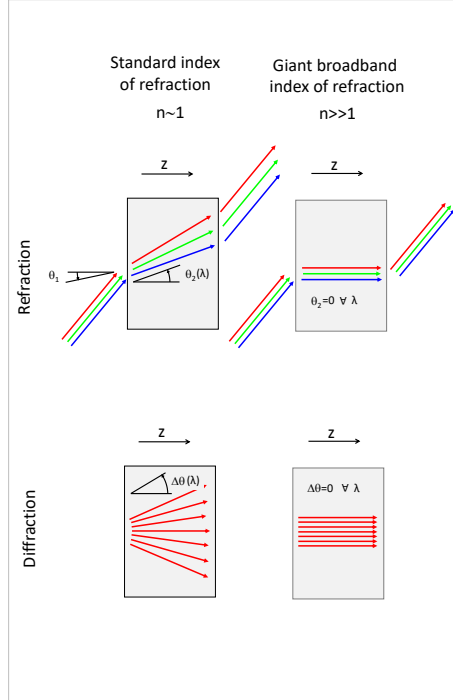


Figure 3.1. Giant Refraction (GR). Left; In a conventional material, light undergoes wavelength-dependent refraction (i.e. $\theta_2 = \theta_2(\lambda)$) and diffraction occurs with a wavelength-dependent angular spread $\Delta\theta(\lambda)$. Right: In a material with $n \gg 1$ we would observe giant refraction, that is, light is projected through it with $\theta_2 \simeq 0 \forall \lambda$, while no diffraction occurs ($\Delta\theta \simeq 0$), forming an ideal imaging material.

The dephasing of these components, i.e., diffraction, is thus associated with the value of $\partial k_z/\partial k_x = -k_x/\sqrt{k_0^2n^2 - k_x^2 - k_y^2} \sim (1/n)$ that vanishes, along with

$\partial k_z / \partial k_y$, as $n \gg 1$. Analogously, also the angular spread vanishes for $n \gg 1$, $\Delta\theta = |k_\perp|_{max} / k_z \sim 1/w_0 k_0 n$, where $|k_\perp|_{max} = |\sqrt{k_x^2 + k_y^2}|_{max} \sim 1/w_0$ is the size of the transverse angular spectrum at the boundary. In other words, for all wavelengths, $\theta_2 \simeq 0$ for all launch θ_1 , (no chromatic aberration) and we have a vanishing angular spread $\Delta\theta \simeq 0$ for all beam sizes w_0 (no diffraction). In terms of imaging, GR causes the material to project the input optical field directly to the output of the sample as if the space occupied by the material itself were absent (see Fig. 3.1). While GR is generally inaccessible in an isotropic material because an $n \gg 1$ implies that the Fresnel reflection coefficient at the input (and output) boundary is $R \simeq 1$ [75], i.e., no light ever enters or leaves the material, it becomes accessible in an anisotropic material. Strong anisotropy together with a giant dielectric response is found in critical disordered ferroelectric perovskites [2, 3, 34].

3.1.2

Experimental setup

The key ingredient of our experiment is a nanodisorder ferroelectric perovskite, a zero-cut polished lithium-enriched solid-solution of potassium-tantalate-niobate (KTN:Li) with an average composition $\text{K}_{0.997}\text{Ta}_{0.64}\text{Nb}_{0.36}\text{O}_3:\text{Li}_{0.003}$. It measures in the three directions $6.0^{(x)} \times 2.6^{(y)} \times 3.0^{(z)}$ mm and has a pale green hue (with an absorption of 2 cm^{-1} in the visible) caused by a small component of Cu impurities. The unit cell manifests random substitutions, a compositional-disorder that, on consequence of the structural flexibility typical of perovskites, leads to locally modified polarizabilities and temperature-dependent nanoscale dipolar structures (nanodisordered ferroelectricity).

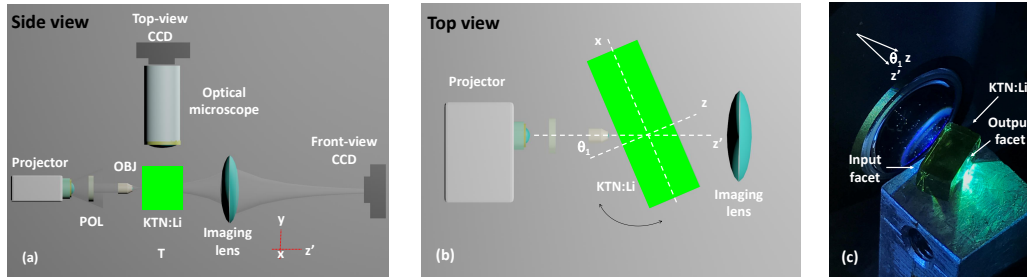


Figure 3.2. Sample and apparatus. (a) Side-view and (b) top-view of the experimental setup. (c) Image of the KLTN crystal during GR experiment. Strongly diffracting white-light from a projector is focused onto the sample, propagates through it, and appears to exit as if it had been focused directly onto the output facet, 3mm away. The sample projects the input light beam to the output as if not only the sample is absent, but also the space occupied by it.

The result is a modified ferroelectric behavior dominated by so-called polar-nanoregions (PNRs), characterized by dielectric dispersion and out-of-equilibrium behavior (relaxor ferroelectricity) [5, 76] (see section 1.2.1). In our present case, this disorder is itself not homogeneous, manifesting a spatially-periodic micrometric

oscillation along a specific crystal axis. This is because the sample is grown into a bulk through the top-seeded method, a technique that entails a slight time oscillation in the temperature of the solidifying melt that, in turn, translates into a characteristic periodic pattern along the growth (or pull) axis. This pattern conditions the nanoscale dipolar structures that, at the room-temperature Curie point ($T_C=288$ K), form a three-dimensional mesh of spontaneous polarization, the super-crystal (SC) [51, 77], as discussed in section 1.3.2 and Chapter 2. The experimental setup is sketched in Figs. 3.2 (a-b). The source is a commercial projector (NEC-VE281X, XGA, 2800 lumens). Light exiting a bright screen image is sent through a linear polarization filter (POL) that allows the passage of light polarized along the x axis (TM mode) or along the y axis (TE mode). Light is collected using a high-aperture long-working distance microscope objective (OBJ, Edmund Optics, 100X, 3mm working distance, achromatic, NA =0.8) positioned approximately 30 cm from the output lens of the projector. An important parameter in experiments is the rotation angle of the KTN:Li sample around the vertical y axis, θ_1 (see Fig. 3.2(b)), i.e., the angle between the normal to the sample input facet (z) and the experiment propagation axis (z'). A typical example of a GR experiment is reported in Fig. 3.2 (c). Images are obtained using an Apple iPhone7 either directly or through one eyepiece of a high-aperture optical microscope (Nikon, NA=0.8) positioned on top of the sample, along the y axis. Higher resolution images are attained placing in the eyepiece a high-resolution black-and-white charged-coupled-device CCD (PCO Pixelfly, 14 bit, 1392×1060 pixels). Transmitted light is collected by an imaging lens with numerical aperture 0.35 and focal length 75 mm. This lens forms an image of a desired plane onto the front-view CCD (Thorlabs BC-106VIS, 12 bit). Sample temperature is fixed by a current-controlled Peltier junction and is positioned and rotated using micrometric stages.

3.1.3

White Light Propagation

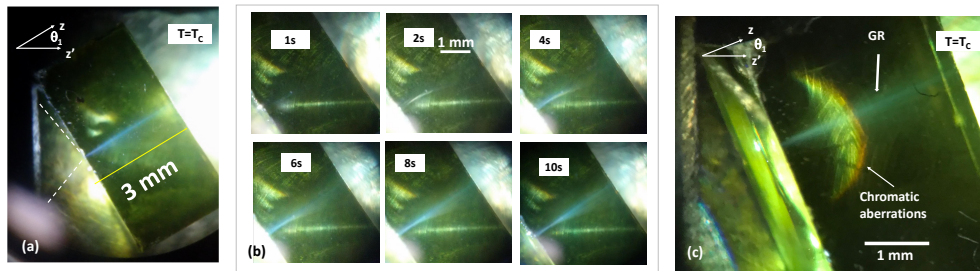


Figure 3.3. Low resolution white-light experiments. Low resolution color images of the GR inside the KLTN sample. (a) Top view of the behavior of light inside the sample and (b) the manifestation of GR as the sample thermalizes at the Curie point. (c) Achromatic nature of GR compared to colored scattering from the bottom alluminium support.

In Fig. 3.3 (a) the top view image shows light undergoing GR: the beam is transmitted orthogonal to the sample facets, irrespective of the actual tilt angle. In fact, for $T = T_C$, a distinct white beam forms that extends from the input of the sample to the output. This beam propagates with $\theta_2 = 0$, is white, and does not spread, even though it originates from a white incoherent focused spot from the microscope objective. We underline that, normally, the white beam diffracts so as to engulf the entire sample and chromatic aberrations appear. The GR beam forms on consequence of thermalizing the crystal to T_C , as can be appreciated in Fig. 3.3 (b), where the sample originally at 303 K is brought to $T = T_C = 288\text{K}$ and progressively thermalizes in time. Intervals of time measure the delay between the moment in which the image is captured and that for which the sensor measuring the temperature of the sample first reaches T_C . The phenomenon depends solely on T and is independent of beam intensity, size, launch angle θ_1 , and position in the sample.

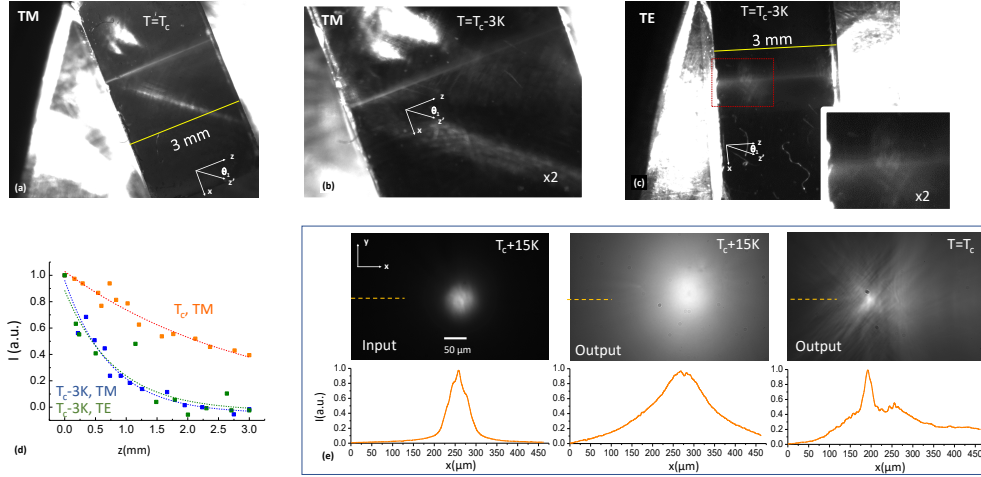


Figure 3.4. High resolution white-light experiments (a) High resolution top-view of the beam suffering GR at $T = T_C$ and (b) at $T < T_C$, an increased scattering is evident. (c) GR for the TE mode ($T < T_C$). (d) Intensity of scattered light along propagation for different polarization states and temperatures. (e) Input and output transverse intensity distribution when the sample manifests standard refraction ($T > T_C$) and GR ($T = T_C$). The broad background at $T = T_C$ is the original diffracting Snell component that is, in the present case, angularly superimposed with the GR beam.

As expected, GR also occurs when the white-light is focused before and after the input facet, but with a correspondingly larger width in the GR component. Specifically, in Fig. 3.3 (b), the focus is formed inside the sample and, as the GR regime emerges, the actual focus disappears and leads to a slightly enlarged GR transmission. The GR beam does not manifest the chromatic dispersion that can, in turn, be directly observed in conventional scattering from the crystal support, as reported in Fig. 3.3 (c). Higher-resolution images of the effect are reported in Figs. 3.4 (a)-(c). Figure 3.4 (a) reports the GR effect as the sample is kept at the

ferroelectric Curie point, while Fig. 3.4 (b) reports the phenomenon when the sample is kept at a lower temperature ($T_C - 3$ K). Compared to the GR case, increased scattering causes light to decay along the normal to the input facet. Enhanced scattering appears in the path of the beam. At this same temperature, also light polarized in the orthogonal TE mode suffers GR, along with a similar scattering (Fig. 3.4 (c)). The intensity of scattered light, as deduced from scattered intensity, is reported in Fig. 3.4 (d) (where background noise has been subtracted). Orange squares refer to data from the $T = T_C$ GR and indicate an exponential decay with a decay rate of 3.8 cm^{-1} while blue and green curves refer, respectively, to the TM and TE modes at $T = T_C - 3\text{K}$, with a decay rate of 11.2 cm^{-1} . Front images of the projector light are reported in Fig. 3.4 (e) at the input and output at $T = T_C + 15\text{K}$ and $T = T_C$. Light is focused to a $52 \mu\text{m}$ spot, and the sample is rotated by an angle of $\theta_1 = 35^\circ$. When GR emerges, the output Full-Width-at-Half-Maximum (FWHM) is $35 \mu\text{m}$, while without GR the FWHM is larger than $142 \mu\text{m}$ (the input FWHM is $52 \mu\text{m}$), as the output diffraction image is a convolution of the actual spread out beam with the limited optical transfer function of the output imaging lens. Because no refraction and diffraction are observed at T_C (Fig. 3.4), the estimated value of n across the visible spectrum descends from the experimental uncertainty. In terms of the angle of refraction, spatial resolution is limited by the width of the beam ($\sim 50 \mu\text{m}$) and the length of the sample ($L_z = 3 \text{ mm}$), so that the minimum observable θ_2 is $\delta\theta_2 = 50/3000 = 0.017$. Consequently, the minimum observable index of refraction is $\delta n = \sin \theta_1 / \sin \delta\theta_2 = 34$ ($\theta_1 = 35^\circ$), hence $n > 34$ for the spectrum of the projector lamp.

3.1.4

Physical origin of Giant Refraction

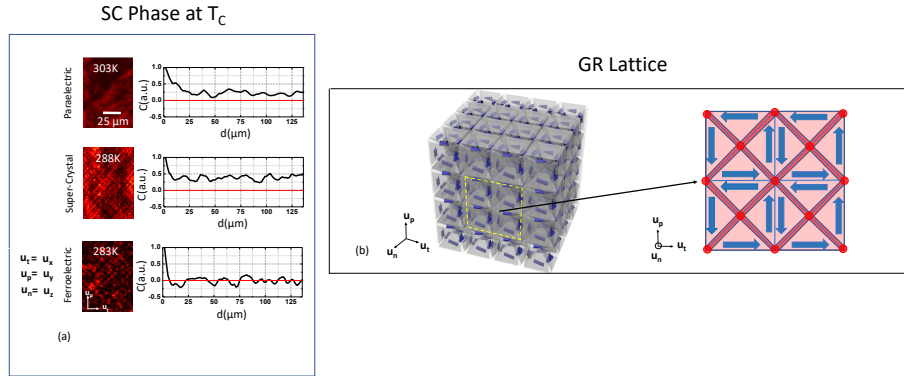


Figure 3.5. Monochromatic experiments and the physical origin of GR. (a) Optical characterization of the ferroelectric SC (the correlation coefficient $C(d)$ is calculated between a portion of the intensity distribution transmitted by the sample $35 \times 35 \mu\text{m}^2$ and a portion shifted by d along the \mathbf{u}_p axis). (b) Spontaneous polarization mesh in the perovskite tetragonal SC phase with a blow-up of the regions (red) supporting TM GR.

To further investigate the GR effect we have performed experiments with laser light substituting the projector with a 5 mW He-Ne laser operating at $\lambda = 632.8$ nm and linearly polarized along \mathbf{u}_t . The monochromatic light transmission is reported in Fig. 3.5 (a) for $T > T_C$ (303 K), $T = T_C$ (288 K), and $T < T_C$ (283 K). At T_C the emergence of a coherent spatial structure, typical of the ferroelectric SC [51, 77], leads to a finite correlation in the intensity distribution, absent in the paraelectric transmission and in the subcooled ferroelectric state, where relevant domain disorder is observed. Optical diffraction experiments indicate that the SC is compatible with the three-dimensional mesh of spontaneous polarization (blue arrows) illustrated in Fig. 3.5 (b) (left). Here the anisotropy required for GR occurs on a subset of regions in the sample that forms a characteristic lattice illustrated in Fig. 3.5 (b) (right) (red-shading). In detail, the blue-shaded regions contain spontaneous polarization prevalently along \mathbf{u}_t and \mathbf{u}_p , while the red-shaded regions also contain spontaneous polarization along \mathbf{u}_n . In conditions in which the optical susceptibility is enhanced along the direction of spontaneous polarization, these regions have the principal components of the index of refraction tensor that allow TM GR, i.e., $n_{nn} \gg n_{tt}, n_{pp}$ along \mathbf{u}_n , \mathbf{u}_t , and \mathbf{u}_p , respectively. GR for the TE mode, in turn, is supported by the regions with a prevalently \mathbf{u}_p directed spontaneous polarization (not illustrated). Only the component of the input beam that impinges on the regions that allow the correct anisotropy can actually manifest GR, while the remaining component of light suffers standard Snell refraction.

3.1.5

Laser Light Propagation

The presence of the two components is confirmed using low-aperture laser light, as reported in Fig. 3.6 (a). For low-aperture experiments (Figs. 3.6 (a-c)), the beam is first expanded using two confocal lenses to a plane-parallel 10 mm radius beam. The beam is then focused using a 150 mm focal length lens onto the input facet of the sample. The beam numerical aperture is NA=0.1 (in air). The input beam has a FWHM of 18 μm and is TM polarized. Top view images are captured in a fashion similar to that used for white-light (scattered light leads to an estimated monochromatic 632.8 nm decay rate along propagation at T_C of 4.6 cm^{-1} for the steady-state of Fig. 3.6 (c). Thanks to this procedure, we are able to study the component of the light beam that undergoes standard refraction and diffraction, not observable in the white-light experiments of Figs. 3.3 and 3.4. Moreover, as expected from the wholly three-dimensional nature of the SC, the effect occurs along all three directions of the underlying SC (see Fig. 3.6 (b) for GR with \mathbf{u}_n along the 6mm long side of the sample). Front view images and intensity profiles of transmitted light reported in Fig. 3.6 (c) indicate that the GR suffers a filamentation with a characteristic scale of tens of micrometers, compatible with the scale of the SC. Close inspection reveals that this filamentation is also marginally visible in the top-view images of the output facet, but at lower resolution, as caused by the coherent speckle dominated laser scattering (indicated as "Filaments" in the top-view image). The image is further distorted by the finite depth of focus of the imaging system, as this only allows a portion of the filaments (dashed yellow box in Fig. 3.6 (c)) to be in focus at a time in the strongly tilted geometry.

In Figs. 3.7 (a-c) we analyze laser light propagation in high-aperture conditions where the expanded laser light is strongly focused onto the input facet using the microscope objective (NA=0.8). The experiments are carried out with $\theta_1 = 35^\circ$ and the two reported sequences in Figs. 3.7 (a-c) differ in the actual position of the sample relative to the fixed input launch beam. In high aperture experiments, the component not undergoing GR diffracts to $81 \mu\text{m}$, so that its intensity is too low to be detected when the GR component forms with its highly localized spots (Figs. 3.7 (a-c)). This means that, as the sample thermalizes at $T = T_C$, only the GR beam is visible. Front-view images reported in Fig. 3.7 (b) indicate a spatial structure that reproduces the GR supporting structure (red-shaded regions) illustrated in Fig. 3.5 (b) (right). Congruently, the GR pattern is rigidly locked to the sample, it is found to move and rotate following the sample itself. In fact, while the SC (see Fig. 3.5 (a)) for $\theta_1 = 0$ is isotropic in the x and y directions, the images of the guided tilted cases for $\theta_1 = 35^\circ$ manifest an anisotropy compatible with a rotation of the SC structure of Fig. 3.7 (b) by $\theta_1 \simeq 35^\circ$.

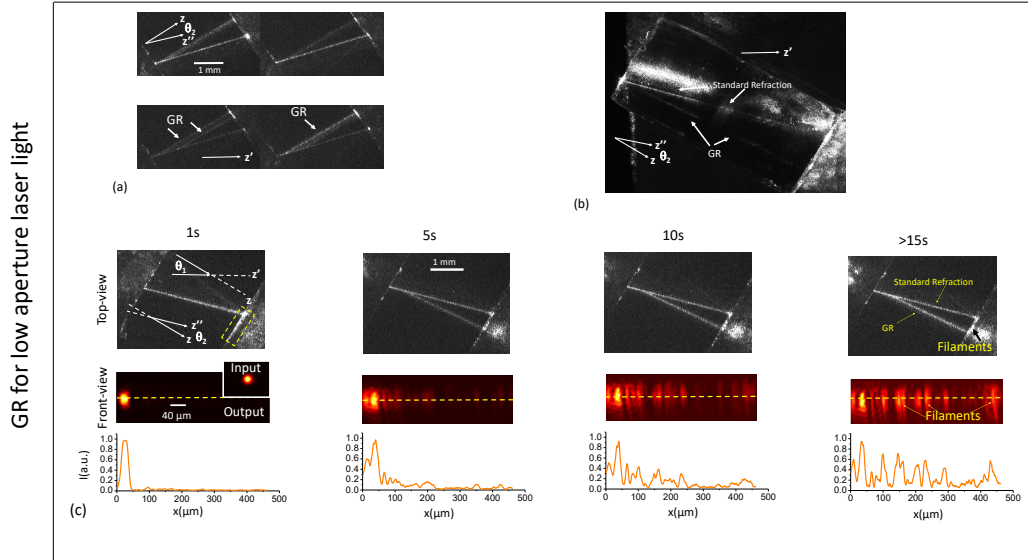


Figure 3.6. GR for low aperture laser light. (a) Low aperture laser light showing the decay of the standard refraction component into multiple GR beams at $T = T_C$ along with the standard refraction component (see text). (b) The top-view snapshot reports GR along the long 6 mm side of the sample. (c) Detailed analysis of laser light propagation seen from a top-view (top) front view (central) and as a profile along the dashed line (bottom) as the sample relaxes to $T = T_C$. Time intervals are measured starting from when the temperature gauge reaches T_C .

The consequence is that the whole GR process can even be confined to a single micrometric section of the sample, corresponding to a single vertex in the red-shaded region of Fig. 3.5 (b) (right), if the input launch beam is sufficiently focused down

and appropriately aligned, as reported in Fig. 3.7 (c) ("Position B" as opposed to the generic input "Position A" in Fig. 3.7 (b)). As expected, not only does the beam propagate along the normal of the input facet irrespective of the launch angle, but the beam itself does not spread on consequence of diffraction. Experiments in Fig. 3.7 allow an estimate of n (at the laser wavelength) analyzing beam diffraction. Comparing the output intensity FWHM in the steady-state case of Fig. 3.7 (c), where only one polarization-vertex is involved and the distortion associated with filamentation is absent, to the input FWHM (Fig. 3.7 (a)), we find that the beam spreads from $4.7 \mu\text{m}$ to $6.8 \mu\text{m}$ after a $L_z = 3\text{mm}$ propagation, leading to an estimate of $n > 26$ as explained in section 3.1.7.

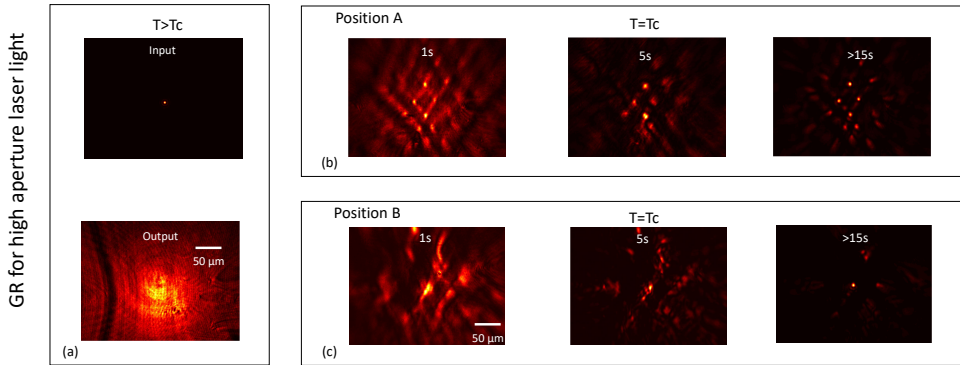


Figure 3.7. GR for high aperture laser light. (a) Input and output beam distribution for $T > T_C$. (b, c) Output intensity distributions as the crystal settles to T_C for two different launch positions, Position B corresponding to a GR that involves only a micrometric section of the sample that coincides with a single polarization vertex.

This confirms the huge values of n already encountered in the white-light refraction experiments, huge values that suggest that at T_C local fields play a principal role. We point out that, physically, in a system where the dielectric susceptibility is dominated by weakly-interacting atoms or molecules, an $n \gg 1$ across the visible spectrum appears incompatible with the constraints on atomic/molecular polarizability. In these conditions, GR would require operation in proximity of a resonance, where, however dispersion and absorption make imaging unfeasible. In turn, in the strongly correlated perovskite where susceptibility is dominated by local fields, n can be anomalously enhanced through self-action. In a simplified isotropic approximation, a description is given by the Lorentz-Lorenz relation $n^2 = (1 + (8/3)\pi N\alpha)/(1 - (4/3)\pi N\alpha)$, where N is the density of atoms and α is the atomic polarizability: conditions in which $(4/3)\pi N\alpha \sim 1$, as would occur in proximity of a phase-transition, then allow GR [75, 78]. The giant index value here reported is noticeably lower than giant refraction reported at microwaves [71], as the longer wavelengths involve more components to the susceptibility and lead to a larger linear response. Numerical simulations indicate that rescaling a microwave giant index of refraction to the near-visible spectrum leads to a giant refraction comparable with the one reported here, and what is termed giant will depend on the region of the spectrum investigated [71].

3.1.6

Giant Refraction and Anisotropy

Giant Refraction implies refraction along the normal to the boundary of the medium, no chromatic aberration, and no diffraction. In turn, the boundary conditions for an isotropic material with GR also imply that very little light can actually enter or leave it, as rendered explicit by the standard Fresnel equations. For example, in the case of normal incidence, the coefficient $R = |(1 - n)/(1 + n)|^2 \rightarrow 1$ as $n \rightarrow \infty$.

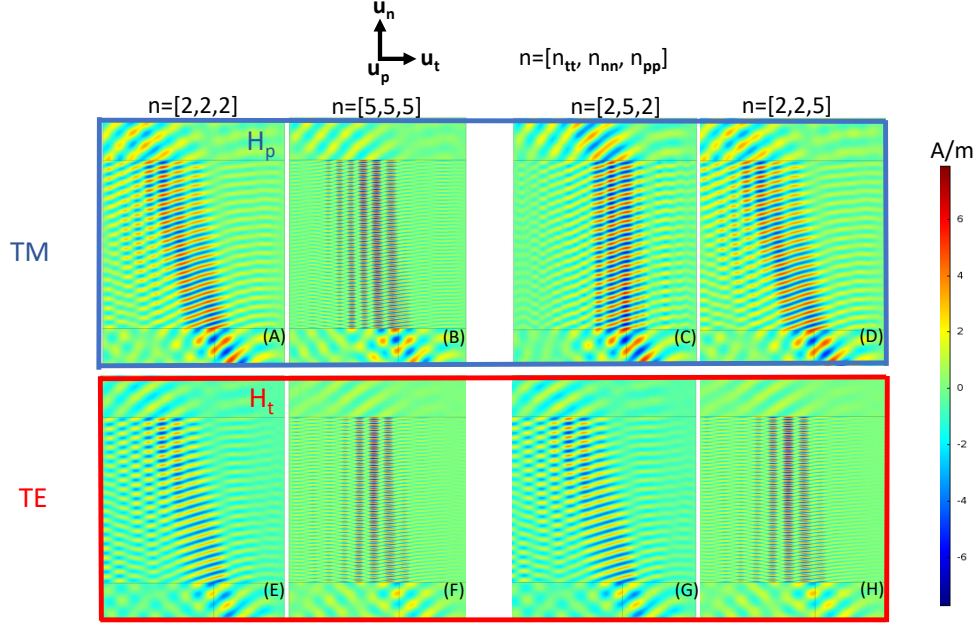


Figure 3.8. Numerical analysis (using an FDTD algorithm) of refraction and reflection in various conditions (see text). The wave has $\lambda = 632.8$ nm, an input width of $1.75 \mu\text{m}$, $\theta_1 = 45^\circ$, and is allowed to propagate in the refracting material that is $6 \mu\text{m}$ in length along \mathbf{u}_n .

An analogous anomalous reflection also occurs on exiting the material, where now the relative index of refraction is $(1/n) \ll 1$. Fresnel reflection, in turn, does not hamper GR in anisotropic systems [79]. In Fig. 3.8 we report 1+1D FDTD numerical results for reflection and refraction for the TM and TE modes, where \mathbf{u}_t is the unit vector parallel to the boundary in the incidence plane, \mathbf{u}_n is the unit vector normal to the boundary, and \mathbf{u}_p is the one normal to the incidence plane. In Fig. 3.8 (a) standard refraction and reflection can be found for a homogeneous $n = 2$ TM case, while, as reported in Fig 3.8 (b), for $n = 5$, both refraction and reflection are stronger. In Fig. 3.8 (c), (d) we report the cases with $n_{tt} = 2$, $n_{nn} = 5$, $n_{pp} = 2$ and $n_{tt} = 2$, $n_{nn} = 2$, $n_{pp} = 5$, respectively. The picture is radically modified in Fig. 3.8 (c) where the diagonal index matrix has $n_{tt} = 2$, $n_{nn} = 5$, $n_{pp} = 2$: enhanced refraction is found without the enhanced reflection. The TE case is reported in Fig. 3.8 (e-h), where enhanced refraction is observed in the case of $n_{tt} = 2$, $n_{nn} = 2$, $n_{pp} = 5$ (Fig. 3.8 (h)) and, as for the homogeneous case of Fig. 3.8 (h), also enhanced

reflection is found. In the TM case refraction is associated to the matching of the wave-vector across the boundary along \mathbf{u}_t , and this involves the component of the optical electric field that oscillates along \mathbf{u}_n so that, in order to have GR, $n_{nn} \gg 1$ is required. In turn, the Fresnel equations involve the susceptibility along \mathbf{u}_t , so that a standard n_{tt} leads to standard reflection. In the TE case, GR involves the optical component of the electric field that oscillates along \mathbf{u}_p , so that $n_{pp} \gg 1$ is needed. Since, however, in this case the Fresnel equation involves n_{pp} , GR is accompanied by strong reflection.

3.1.7

Index of refraction evaluation from diffraction

Experiments in Figs. 3.7 (d-f) report beam propagation in conditions of elevated numerical aperture where non-paraxial corrections become relevant. However, if we self-consistently assume that $n \gg 1$, then the non-paraxial regime ceases to exist, as the effective wavelength λ/n shrinks far below any reasonable transverse size of the beam. Applying the standard diffraction laws of Gaussian beams, we then have that the width of the beam at a given position z along propagation $w(z)$ is related to the input minimum spot size w_0 by the relationship $w(z) = w_0 \sqrt{1 + (z/z_0)^2}$, where $z_0 = n\pi w_0^2/\lambda$ is the Rayleigh length, so that $n = (L_z \lambda / \pi w_0^2) (w(L_z)^2 / w_0^2 - 1)^{-1/2}$. The residual spreading from the 4.7 μm input to 6.8 μm output reported in Fig. 3.7 (f) indicates that two 4.7 μm spots displaced by less than 3.4 μm at input will manifest strong overlap and cannot be fully distinguished at output.

3.2

Broadband giant index of refraction

GR suggests a solution to overcome chromatic dispersion in image transmission that sides other recent pioneering solutions, such as those based on metasurfaces [80], while offering new flexibility to presently available micro and nanoscale photonics for applications in optical components, lithography [81], and transformation optics [82]. The very idea that white-light is transferred, irrespective of its launch direction, along the normal to the sample can play a role in developing self-aligning white-light photonics, as would be required to harness, for example, sunlight during a day. The vanishing effective wavelength $(\lambda/n) \rightarrow 0$ ($n \gg 1$) implies at once that the laws of achromatic geometrical optics hold and that light energy can be localized to presently inaccessible submicrometric scales. For example, a microscope housed inside a medium manifesting GR will be able to detect features down to a vanishing Abbe limit $d = \lambda/(2NA)$, as the numerical aperture $NA \propto n$ diverges [75]. Furthermore, ultra-tight transverse localization of light, that scales with $(\lambda/n)^2$, can potentially reduce the active material required in detectors or solar-panels, reducing the costs associated to the use of innovative materials, such as photovoltaic perovskites [1]. In terms of subwavelength quantum photonics, strong localization can also form the ideal setting for photon-by-photon nonlinear optics [83, 84].

Nonlinear response in the super-crystal phase

Nonlinear response in a material increases with its index of refraction as n^4 . Hence giant broadband refraction, i.e., an index of refraction $n \gg 1$ across the visible and near infrared spectrum, emerges as a direct route to strongly enhanced nonlinear response. In this Chapter, we report second-harmonic-generation experiments in a ferroelectric super-crystal manifesting giant refraction. Enhanced response allows the process to occur through bulk nonlinear Cherenkov radiation even for highly focused non-phase-matched beams, a method to achieve constraint-free wavelength conversion.

4.1 Constraint-free wavelength conversion supported by giant optical refraction

Frequency conversion and parametric amplification are fundamental ingredients for a wide family of applications, including light sources, detection, optical processing, and quantum-state-generation [85–88]. For quantum technology, a versatile and super-efficient nonlinear process is the key to photon-based quantum computing [83, 89, 90]. In most schemes, optical nonlinearity can only be effectively harnessed when the coupling mechanism is driven by a cumulative wave interaction based on constructive interference. This imposes specific constraints on the available conversion schemes, so-called phase-matching conditions that depend both on the polarization, wavelength, and direction of propagation of the interacting waves and on the specific nonlinear susceptibility of the medium [85]. These constraints can be overcome in engineered ferroelectric crystals with a full 3D periodic spontaneous polarization distribution through quasi-phase-matching [49, 91–94] and Cherenkov phase-matching [95–102]. As mentioned in section 1.3.2 and in Chapter 3, a super-crystal (SC) is also accompanied by a giant broadband optical refraction [103]. This

has a direct effect on nonlinear scattering. Considering material polarization P in terms of the Taylor series expansion in the propagating optical field E_{opt} , i.e., $P = \epsilon_0 (\chi^{(1)} E_{opt} + \chi^{(2)} E_{opt}^2 + \dots)$ [85, 104], the first term describes linear response through the first order susceptibility $\chi^{(1)} = n^2 - 1$, while higher-order terms describe nonlinear effects. The validity of the expansion implies $\chi^{(m+1)}/\chi^{(m)} \sim 1/E_{at}$, where E_{at} is the scale of the atomic electric field of the substance. It follows that the intensity of an arbitrary allowed nonlinear scattering processes scales with $(\chi^{(m)})^2 (E_{opt})^{2m} \sim (\chi^{(1)} E_{opt})^2 (E_{opt}/E_{at})^{2m}$, and the intensity of any higher order scattering processes scales with n^4 [87]. In these terms, giant refraction opens up a new avenue to strongly enhanced nonlinear response.

4.1.1

Giant refraction Cherenkov Phase-matching

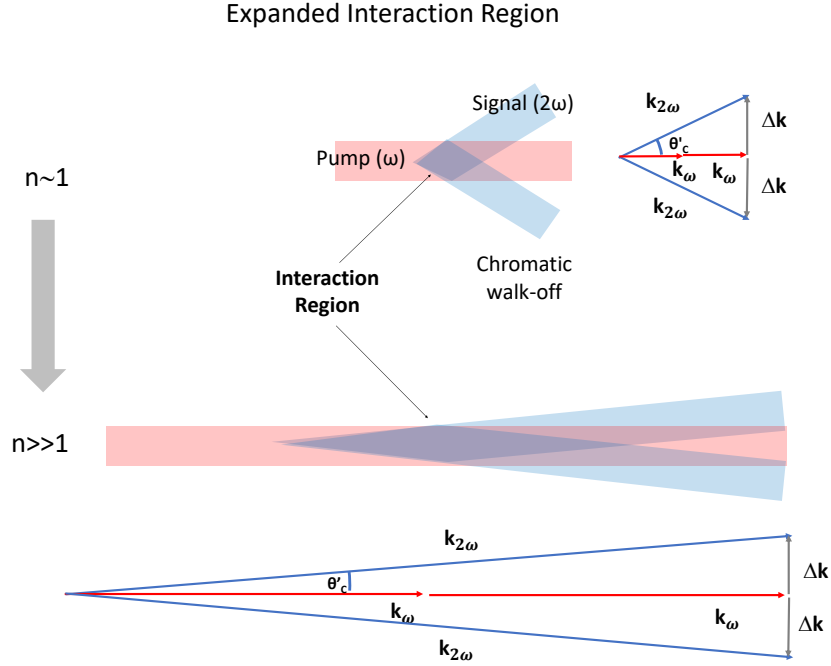


Figure 4.1. Giant refraction Cherenkov Phase-matching. For $n \sim 1$, a finite Cherenkov phase-matching θ'_C leads to a limited beam interaction region associated to a finite beam width and chromatic walk-off. For $n \gg 1$, chromatic walk-off $\theta'_C \simeq 0$, so that the interaction region is expanded.

In the paradigm nonlinear optical process, second-harmonic-generation (SHG), waves are generated at wavelength $\lambda/2$ (and angular frequency 2ω) by the anharmonic response of dipoles driven by the pump at wavelength λ [105]. The process occurs most efficiently when the converted signal interferes constructively with the pump

itself, a phase-matching condition that embodies momentum conservation for the interaction. For any given material, dispersion causes phase-matching to occur naturally in the direction of the pump only for converted light (signal beam) whose wavevector $\mathbf{k}_{2\omega}$ forms a finite angle θ'_C relative to the pump itself \mathbf{k}_ω . This leads to wavelength-dependent constraints on the process geometry while the wavevector mismatch $\Delta\mathbf{k} = \mathbf{k}_{2\omega} - 2\mathbf{k}_\omega$ is accompanied by chromatic walk-off [86] (see Fig. 4.1 top panels). Collinear phase-matching ($\Delta\mathbf{k} = 0$) can, in turn, be achieved using material birefringence, which introduces wavelength and polarization constraints [85], and quasi-phase-matching, that requires periodic material microstructuring and is also wavelength-selective [106, 107]. In a material with giant broadband refraction, $n_\omega, n_{2\omega} \gg 1$, and at the sample input facet the plane-wave components of the pump refract according to the Snell law $\theta_r = \arcsin(\sin\theta_i/n_\omega) \simeq 0$, where θ_i, θ_r are the incidence and refraction angle. Cherenkov phase-matching occurs for SHG wavevectors at an angle relative to the pump $\theta'_C = \arccos(n_\omega/n_{2\omega}) \simeq 0$, insomuch that $\Delta n = (n_{2\omega} - n_\omega)/n_\omega \ll 1$, even for a finite $n_{2\omega} - n_\omega$. Thus, the angle at which Cherenkov phase-matching occurs is greatly reduced ($\theta'_C \simeq 0$) so that chromatic walk-off does not intervene (see Fig. 4.1 (bottom panels)).

4.1.2

Giant refraction Cherenkov SHG

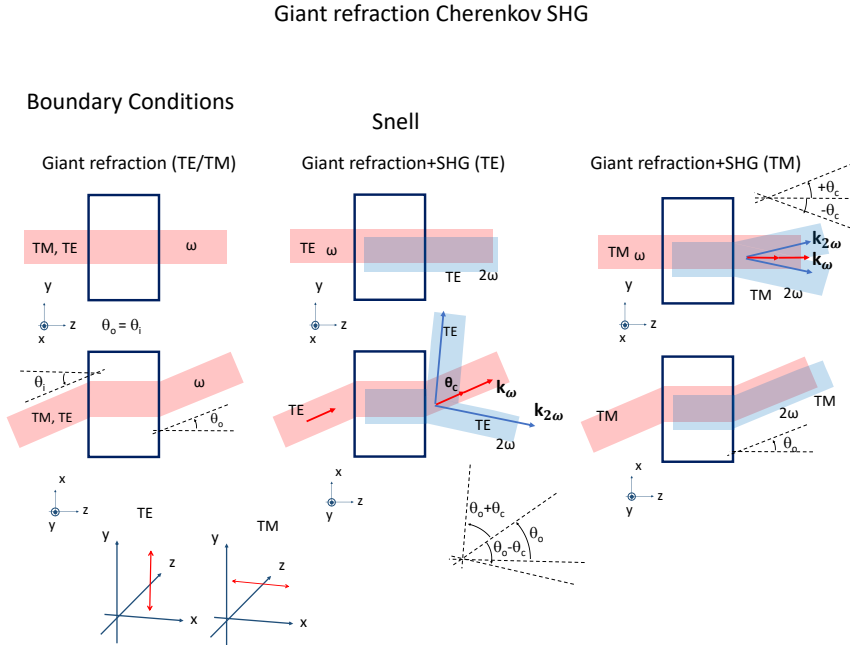


Figure 4.2. Giant refraction Cherenkov SHG. Geometry of giant refraction Cherenkov SHG for the TE and TM cases.

The specific geometrical structure of Cherenkov SHG combined with giant refraction is illustrated in Fig. 4.2. The pump propagates inside the sample along the normal to its input facet irrespective of launch angle θ_i (left panels) and the Cherenkov SHG copropagates with the pump inside the sample ($\theta'_C \simeq 0$, central panels). At the output facet the pump and signal separate at a now finite angle θ_C , as illustrated for the two cases of transverse electric (TE) and transverse magnetic (TM) polarizations (central and right panels, respectively). SHG polarization is $P_i^{2\omega} = d_{ijk} E_j^\omega E_k^\omega$, where \mathbf{E}^ω is the pump field and d_{ijk} is the nonlinear optical susceptibility tensor, that has nonzero components d_{31} , d_{33} , and d_{15} for the tetragonal 4mm symmetry of KTN:Li [108]. Considering the TE case for a spontaneous polarization parallel to the optical polarization (along the y axis), $P_y^{2\omega} = d_{33}(E_y^\omega)^2$. The emitted Cherenkov radiation must then have a $\mathbf{k}_{2\omega}$ in a plane orthogonal to $\mathbf{P}^{2\omega}$, i.e., in the incidence plane (xz) (central panels in Fig. 4.2). So, while the pump exits with an angle to the normal $\theta_0 = \theta_i$, the Cherenkov SHG forms two beams angled with respect to the pump by $\theta_0 \pm \theta_C$. Analogously for the TM case, in which, for a spontaneous polarization parallel to the optical polarization (along the x axis), the nonlinear polarization is dominated by the x component $P_x^{2\omega} = d_{33}(E_x^\omega)^2$, so that Cherenkov SHG occurs in the yz plane (right panels in Fig. 4.2). In the TM case, a SHG contribution arises also for a domain with a spontaneous polarization along the z axis, i.e., $P_x^{2\omega} = 2d_{15}E_x^\omega E_z^\omega$ and $P_z^{2\omega} = d_{31}(E_x^\omega)^2 + d_{33}(E_z^\omega)^2$. The emitted Cherenkov SHG will then be TM polarized and have a $\mathbf{k}_{2\omega}$ orthogonal to $\mathbf{P}^{2\omega}$ in the incidence plane xz (i.e., along the y axis). In turn, the SHG Cherenkov radiation separates at the output in the orthogonal plane (the yz plane).

4.1.3

Materials and super-crystal preparation

The SHG experiments are performed in two samples of nanodisordered oxide ferroelectric perovskites manifesting GR with record-high broadband index of refraction ($n > 26$) at visible wavelengths. The two samples (sample 1 and sample 2) are zero-cut polished lithium-enriched solid-solutions of potassium-tantalate-niobate (KTN:Li). They have the same composition $\text{K}_{0.997}\text{Ta}_{0.64}\text{Nb}_{0.36}\text{O}_3:\text{Li}_{0.003}$, while in the flux of sample 2 traces of Mo impurities are introduced. Sample 1 measures along its three axes $4.62^{(a)} \times 3.86^{(b)} \times 1.6^{(c)}$ mm while sample 2 is $6.96^{(a)} \times 3.86^{(b)} \times 1.6^{(c)}$ mm. The samples form perovskites with room-temperature cubic-to-tetragonal (m3m to 4mm) ferroelectric phase-transition temperatures $T_{C,1} = 315$ K and $T_{C,2} = 333$ K. Both are grown through the top-seeded method that causes them to have a built-in spatially periodic oscillation in composition along the growth axis (the a axis) that translates into an approximately periodic $\Lambda = 50 \mu\text{m}$ striation grating (for sample 2) that then determines the lattice constant of the underlying super-crystal [51]. To better achieve the super-crystal phase, each sample, initially equilibrated at $T = 298\text{K}$ and unbiased, is heated to $\simeq 373$ K at a rate of 0.6 K/min and is DC-biased by an electric field that increases at a constant rate from 0 to 4 kV cm^{-1} . The sample is then cooled back down to $T = 298\text{K}$ while the bias field remains constant at 4 kV cm^{-1} . The DC field is applied between the two parallel faces along the a axis (growth axis). To minimize the temperature gradient, the sample is

dipped into a Teflon holder that contains temperature resistant mineral oil. The super-crystal can now be further modified having the sample undergo successive thermal cycles, composed of a first stage in which the unbiased sample is heated to $T_C + 10K$ at a rate of $0.35Ks^{-1}$ immediately followed by a second cooling stage to $T_C - 35K$ at a rate of $0.1 Ks^{-1}$. Once the thermal protocol is completed, each sample is used for optical experiments at a given temperature $T < T_C$.

4.1.4

Experimental setup and SHG conversion efficiency

SHG experiments (see scheme and photo of apparatus in Fig. 4.3 (a-b)) are carried out in the 790-880 nm range using a Tsunami Spectra Physics Ti:Sa CW mode-locked laser (maximum output power of 0.6W at $\lambda = 810 \pm 7$ nm), with a repetition rate of 80 MHz and a pulsewidth of 190 fs. Laser beam linear polarization, TM or TE, or a superposition of the two, is set using a $\lambda/2$ waveplate. The beam is focused onto the input facet of the θ_0 -rotated sample using a 50-mm-focal-length lens. The pump beam is focused to an input FWHM $\simeq 15\mu m$.

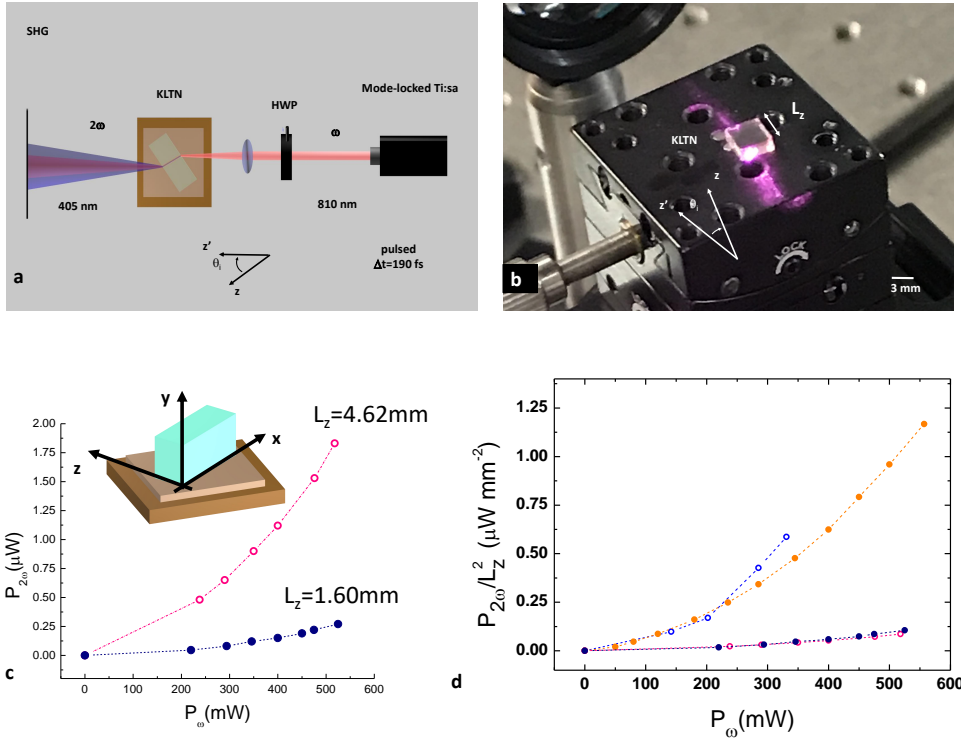


Figure 4.3. Experimental setup and SHG conversion. (a-b) SHG is observed using a mode-locked Ti:sa laser (c) Average output SHG power versus pump input power along two different lengths of one sample (sample 1). Conversion scales with P_ω^2 and with L_z^2 as would occur for bulk SHG conversion [104]. (d) Output SHG power $P_{2\omega}$ normalized to L_z^2 versus input pump P_ω at a $\lambda = 810\text{nm}$ and $\theta_0 = 0$ for sample 1 and sample 2.

The SHG pattern is detected on a white screen placed at $d=7.0$ cm from the output facet of the sample using a Canon EOS 50d. In Fig. 4.3 (c) we report output SHG power versus pump input power. The observed scaling $P_{2\omega} \propto (P_\omega)^2 L_z^2$, where L_z is the length of the sample in the z direction, is reminiscent of the undepleted pump regime of standard SHG [85, 104]. The $P_{2\omega}/P_\omega$ ratio is independent of input polarization, and output polarization is found to coincide with the input. Furthermore, SHG power $P_{2\omega}$ is measured filtering and focusing converted light onto a power meter for a TM pump (and SHG). We also provide a comparison of the wavelength conversion in the two samples to identify possible growth and composition related effects. We found that sample 1 and 2 manifest the same geometrical behavior as regards to giant refraction and Cherenkov SHG, while their net SHG conversion efficiency is considerably different, as reported in Fig. 4.3 (d). This may be connected to the different values of Curie temperature and/or different values of Λ ($70 \mu\text{m}$ for sample 1 and $50 \mu\text{m}$ for sample 2).

4.1.5

3D nonlinear lattice

Wavelength conversion is mediated by the second-order nonlinear susceptibility response $\chi^{(2)}$ of the KTN:Li perovskite in its noncentrosymmetric tetragonal 4mm state. In distinction to single-domain or to quasi-phase-matching schemes, the nonlinear process is mediated by a super-crystal with its specific 3D geometry, giant refraction, and underlying ferroelectric domain structure [99, 109]. Hence, while giant refraction causes conversion efficiency to be essentially independent of polarization, input angle, and wavelength, the details of the SHG output strongly depend on input parameters and the super-crystal structure. As illustrated in Fig. 4.4 (a), the structure of the 3D super-crystal is a volume lattice of 3D polarization vortices that emerge as the cubic symmetry is broken and polarization charge is screened [51, 103]. The super-crystal forms from the periodic compositional disorder along the growth direction (the a axis). Each domain has its spontaneous polarization along one of the 6 principal directions (the direction of the spontaneous polarization is labeled using different colors, see white arrows and colored solids in Fig. 4.4 (a)). In each domain (of a given color), the corresponding nonlinear susceptibility tensor d depends on its orientation. Consider now the pump focused into a vortex site on the a, b facet of the super-crystal (Fig. 4.4 (b-c)). For a TM polarization, most of the component solids lead to a net zero $\chi^{(2)}$ effect, as light experiences a sequence of oppositely polarized tetrahedrals. The tetrahedrals that dominate $\chi^{(2)}$ response are those with a spontaneous polarization in the a direction, if light propagates along the c direction shifted in the b direction above and below a single polarization vortex. Here conversion occurs through a sequence of solids with identically oriented polarization (see Fig. 4.4 (b)). In the TE case, the situation is analogous, but the SHG signal is now produced for light propagating in the c direction in regions shifted in the a direction in proximity of the vortex (see Fig. 4.4 (c)). Focusing the pump on the ab facet into a polarization vortex leads to the output intensity distribution reported in Fig. 4.4 (d-f).

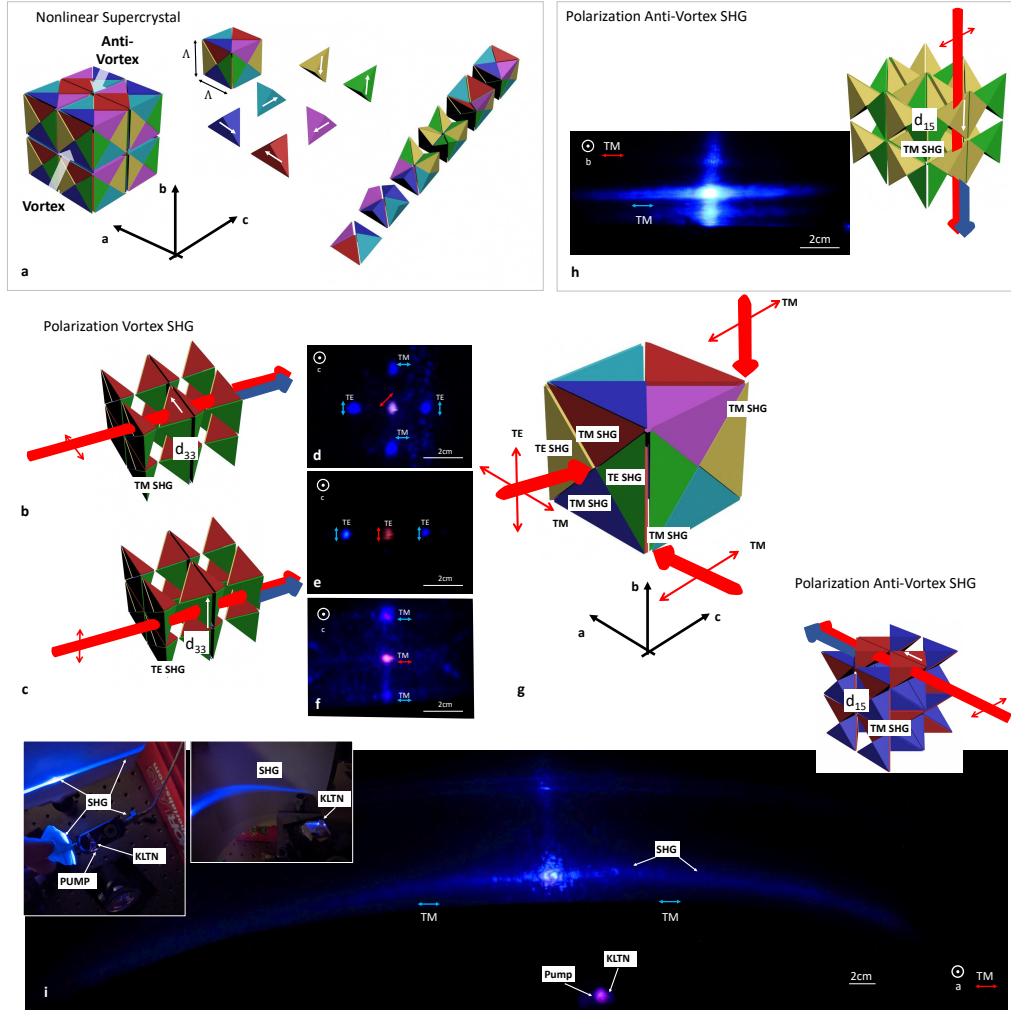


Figure 4.4. SHG in a super-crystal. (a) Illustration of a specific realization of a super-crystal. The spontaneous polarization, the white arrows, determines the specific $\chi^{(2)}$ response of each composing tetrahedral (a color coding is implemented). The actual structure of a fundamental $\Lambda \times \Lambda \times \Lambda$ cube is illustrated through a sequential build-up adding groups of tetrahedral domains. The lattice constant Λ ($\simeq 50\mu\text{m}$) is fixed by the built sample growth process (see section 4.1.3). The super-crystal can have many different chiral realizations. The one illustrated here serves to explain the specific results found, relative to the crystal growth axis a . Indicated are the regions leading to strongest SHG, i.e., the core of polarization vortices in the ab facet and the core of anti-vortices in the ac and bc facets. (b), (c) Non-zero contributions to $\chi^{(2)}$ are illustrated for the TM (b) and TE cases (c). (d-f) Output spatial distribution and polarization distribution for a pump polarized at 45 degrees (d), TE (e), and TM (f). (g) Schematic illustration of the experiments for a pump focused into a single polarization-vortex in the ab facet and into an anti-vortex both in the bc and ac facets. (h) SHG for a pump focused in an anti-vortex in the ac facet. As illustrated in the inset, the only finite contribution to SHG is mediated by b polarized domains through the d_{15} component for TM. (i) SHG for a pump focused in an anti-vortex in the bc facet. Results are analogous to the ac facet, while here a full angle Cherenkov emission is clearly visible ($2\theta_C = \pi$). Note how, in distinction to random-phase-matching, no lateral emission is observed [16, 17, 110], and all SHG is originating, as expected, solely from the output facet (see inset photographs).

For a $\lambda = 810$ nm pump beam polarized at 45 degrees with respect to the crystal a and b axes, a signature SHG Cherenkov output peaked at $\lambda/2 = 405$ nm is detected formed by two TE components in the a direction and two TM components in the b direction, the pump beam being at the center of this diamond-like distribution (Fig. 4.4 (d)). For a TE pump, two TE components in the a direction are dominant (Fig. 4.4 (e)), while for a TM pump, two TM components along the b axis form (Fig. 4.4 (f)). Similar results are observed in both samples 1 and 2. An illustration of the SHG experiments for a pump focused into a single polarization-vortex in the ab facet and into an anti-vortex both in the bc and ac facets is reported in Fig. 4.4 (g). The situation for a pump focused onto the ac facet is reported in Fig. 4.4 (h). Here, only the b oriented ferroelectric tetrahedrals can contribute to giant refraction Cherenkov SHG, and this only for the TM polarization, a condition that is achieved focusing the pump on an anti-vortex as opposed to a vortex. The output structure preserves the TM polarization and has a greatly enhanced output angular spectrum that no longer manifests localized peaks. A similar situation occurs also for light focused onto the bc facet, as reported in Fig. 4.4 (i), where the output SHG is emitted at all available angles (see Fig. 4.4 (i) inset photographs). The observed SHG follows the basic giant refraction SHG Cherenkov mechanism illustrated in Fig. 4.2. In particular, for results reported in Fig. 4.4 (h) and Fig. 4.4 (i), the spontaneous polarization is oriented orthogonal to the input facet, so that while the pump is prevalently experiencing a standard index of refraction n_ω , the SHG is dominated by d_{33} and has a stronger component along the direction of spontaneous polarization. The result then is that $n_\omega/n_{2\omega} \ll 1$, so that θ'_C inside the sample remains finite, while all waves still have their Poynting vectors along the normal to the input facet (giant refraction). This causes this angular amplification caused by the angular spectrum of the focused pump to populate in a continuous manner a wide angle of SHG emission around the pump average propagation direction that, on output, can ever occupy the entire angular spectrum ($2\theta_C = \pi$, Fig. 4.4 (i)). Results on Cherenkov SHG reported in Fig. 4.4, these including conversion for light propagating along all three principal crystal axes, provide a nonlinear corroboration of evidence of a 3D ferroelectric lattice associated to transmission microscopy [51, 103] and polarization transmission microscopy [77].

4.1.6

Cherenkov SHG Experiment

Results on Cherenkov SHG also provide, through a direct measurement of θ_C , an estimate of the super-crystal $2\Delta n n_{2\omega} = (\sin \theta_C)^2$. The phase-matching scheme requires in the case of Cherenkov emission that $\cos(\theta'_C) = (2k_\omega/k_{2\omega}) = n_\omega/n_{2\omega}$. For normal dispersion ($n_{2\omega} > n_\omega$) $n_\omega = n_{2\omega} - \Delta n$, so that since $\theta'_C \ll 1$, $\theta'_C \simeq \sqrt{2\Delta n/n_{2\omega}}$. Outside the sample, $\sin(\theta_C) = n_{2\omega} \sin \theta'_C \simeq n_{2\omega} \theta'_C$. Measuring θ_C leads to an estimate of $\Delta n = (\sin(\theta_C))^2/(2n_{2\omega})$. For light focused on the ac facet in Fig. 4.4 (h) and bc facet in Fig. 4.4 (i), SHG is generated from tetrahedral domains oriented along the b and a axis, respectively, i.e., with a spontaneous polarization orthogonal to the input facet. Involving both d_{31}, d_{33}, d_{15} , the result is a TM SHG in the bc and ac plane, respectively. The observed $\theta_C \simeq \pi/2$ (see detailed photos in the

inset of Fig. 4.4 (i)), corresponding to a $\sqrt{2\Delta n n_{2\omega}} \simeq 1$. A similar contribution associated to d_{15} in the case reported in Fig. 4.4 (b-c), where d_{33} contributions are dominant, and leads to the “spurious” SHG scattering in the TM case (Fig. 4.4 (f)) as opposed to the TE case (Fig. 4.4 (e)). For a pump focused on the ab facet in Fig. 4.4 (b), for both the TE and TM cases, the two SH beams emerge in the x - z (i.e., ac) and y - z (i.e., bc) planes at an angle $\theta_C \simeq 0.28$ rad with respect to the pump (for all accessible values of θ_i). According to the Cherenkov model, this implies that $\sqrt{2\Delta n n_{2\omega}} \simeq 0.28$, so that $2\Delta n n_{2\omega} \simeq 0.08$. Snell refraction experiments in this direction provide $n_{2\omega} > 26$, so that we expect a $\Delta n < 0.001$, corresponding to an ultra-low approximate dispersion of $dn/d\lambda < -0.002\mu\text{m}^{-1}$. The prediction fits in well with our understanding of the super-crystal phase, for which chromatic dispersion is expected to be strongly reduced.

4.1.7

Super-crystal chromatic dispersion

To further investigate our predictions, we directly measured super-crystal chromatic dispersion using group-velocity dispersion [111] for $T > T_C$, where no super-crystal forms, and $T < T_C$, where the super-crystal forms. Results are reported in Fig. 4.5. As expected, the onset of the super-crystal structure is accompanied by a sharp reduction in average values of dispersion, from $dn/d\lambda \simeq -0.10\mu\text{m}^{-1}$ to $dn/d\lambda \simeq -0.06\mu\text{m}^{-1}$.

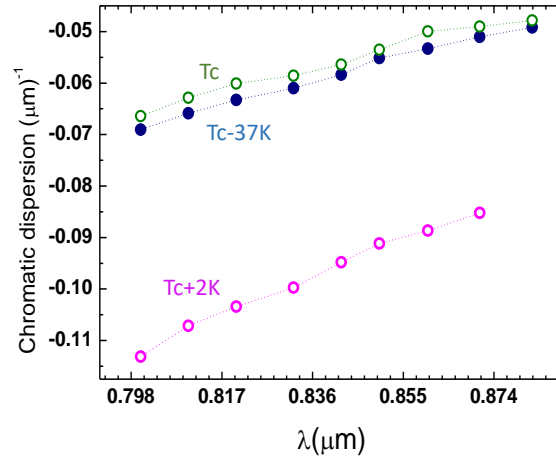


Figure 4.5. Chromatic dispersion. Super-crystal versus cubic phase chromatic dispersion measured using group velocity dispersion experiments in sample 2.

This, in turn, is not sufficiently small to circumvent the need for Cherenkov phase-matching ($\theta_C \simeq 0.28$ in Figs. 4.4 (d-f)). Strong SHG conversion does not allow a local vortex and anti-vortex dispersion measurement.

4.1.8

Spectral and angular acceptance

The angle at which Cherenkov phase-matching is achieved is wavelength-dependent ($\theta_C(\lambda)$). To characterize this we report in Fig. 4.6 (a) measurements of spectral acceptance ($\theta_0 = 0$) for a detector able to collect light only from a limited cone at two fixed angles θ_1 (yellow dots) and θ_2 (magenta dots). The result is a spectral bandwidth whose peak follows $\theta_C(\lambda)$ and whose width is in agreement with the angular acceptance. To test this we maximized SHG efficiency, i.e., Cherenkov phase-matching is established for the specific pump wavelength λ , and the SHG signal detector is placed so as to capture a single output diffraction-limited mode. As reported in Fig. 4.6 (a), changing the pump wavelength without altering the crystal and detector geometry leads to a relative spectral acceptance $\Delta\lambda/\lambda \simeq 0.047$ that is in agreement with the input pump numerical aperture $2\lambda/\pi w_0 \simeq 0.05$. Since giant refraction allows no diffraction or pump-signal walk-off, Cherenkov phase-matching will occur for all wavelengths. In turn, not all Cherenkov SHG can actually leave the output facet of the sample, as total internal reflection occurs for wavevectors that have an internal incidence angle $\theta'_i > 1/n_{2\omega}$ with the output facet. Hence, for a $\theta_i = 0$, $\theta'_i = \theta'_C = \arccos(n_\omega/n_{2\omega})$, a zero emitted SHG will result for $\arccos(n_\omega/n_{2\omega}) > 1/n_{2\omega}$. The effect can be appreciated from the full angle-integrated measurement, reported in Fig. 4.6 (a) (blue circles), where the output SHG is collected by a lens and focused onto a power meter. For a given pump wavelength, the same effect will occur as a function of θ_0 (θ_i). Total internal reflection of the SHG signal occurs at the output facet when approximately $\theta'_C + \theta_r > 1/n$, where $\theta_r = \sin(\theta_0)/n$.

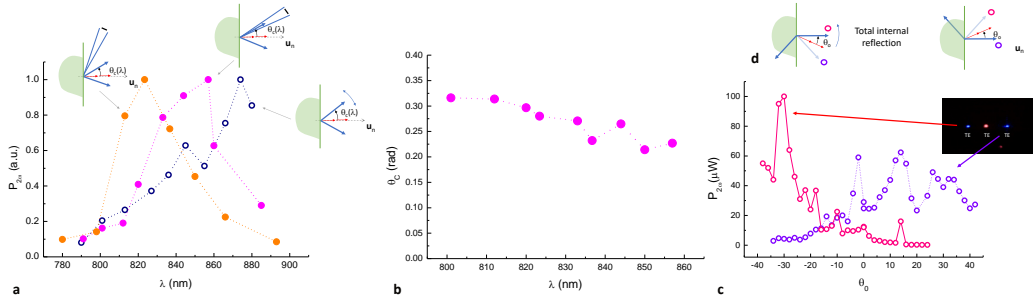


Figure 4.6. Cherenkov spectral and angular acceptance. (a) Spectral acceptance for a detector placed at two fixed angles (yellow and magenta circles) compared to the super-broad spectral acceptance capturing all emitted light (blue circles). (b) Observed Cherenkov angle versus wavelength. (c) Angular acceptance considering the two TE Cherenkov radiation beams separately (magenta and violet circles). (d) Illustration of the geometry leading to SHG suppression caused by total internal reflection of the Cherenkov radiation.

Since $\theta'_C = \sqrt{2\Delta n/n_{2\omega}}$, we have that total internal reflection occurs for $|\sin(\theta_0)| > 1 - \sqrt{2\Delta n n_{2\omega}}$. Assuming the previously evaluated $\sqrt{2\Delta n n_{2\omega}} \simeq 0.28$, we expect to observe a total internal reflection for an input $|\theta_0| > 46^\circ$. Measured values of $\theta_C(\lambda)$ are reported in Fig. 4.6 (b) and are in agreement with chromatic dispersion results of Fig. 4.5. In Fig. 4.6 (c) we report SHG output, for a $\lambda = 810\text{nm}$ pump, for different pump launch angles distinguishing between the two Cherenkov components $+\theta_C$ (violet circles) and $-\theta_C$ (magenta circles). SHG suppression is observed for $|\theta_0| > 25^\circ$. Illustration of the geometry leading to SHG suppression caused by total internal reflection of the Cherenkov radiation is reported in Fig. 4.6 (d). Once again, the broad spectral and angular acceptance underline how the Cherenkov mechanism in action is not Bragg in nature nor does it relate to quasi-phase-matching.

4.1.9

Limitation caused by the Enhanced Fresnel reflection

The $n \gg 1$ regime leading to SHG (as discussed in Fig. 4.4) is accompanied by strong Fresnel reflection at the input and output facets. This does not allow a direct evaluation of enhanced wavelength conversion occurring inside the sample by detecting the converted light transmitted outside the sample. Fresnel reflection can be measured directly for the pump, that experiences a conventional $R \simeq 0.2$, compatible with an average index of refraction ~ 2.6 , as expected for light focused onto the vortex and antivortex core [103]. By aligning the pump in different positions, a maximum is observed $R \simeq 0.45$ compatible with an average $n \sim 5$. In these conditions, conversion can be analyzed through the observation of beam dynamics along the propagation direction. In a standard system, this leads an evolution governed by the so-called Manley-Rowe relationships [85, 104].

In Fig. 4.7 (a-b) we report scattered SHG light from the body of the sample. Observed scattering in our experiment disappears altogether only when the sample is heated above the Curie point T_C (Fig. 4.7 (c)) and for $T < T_C$ leads to an almost constant SHG signal from the input facet of the sample to the output facet. Analysis of the scattered light versus propagation distance in the sample for different temperatures is reported in Fig. 4.7 (d). The transition from SHG to supercontinuum generation is achieved by doubling the input pump numerical, as reported in Fig. 4.7 (e-f). Experiments are carried out replacing the 50mm lens with a 25mm one. The pump is now focused in proximity of the input facet of sample 2 (Fig. 4.7 (e)) and a characteristic white plume is detected. The origin of this broadband emission and its relation to specific nonlinear processes is still unclear.

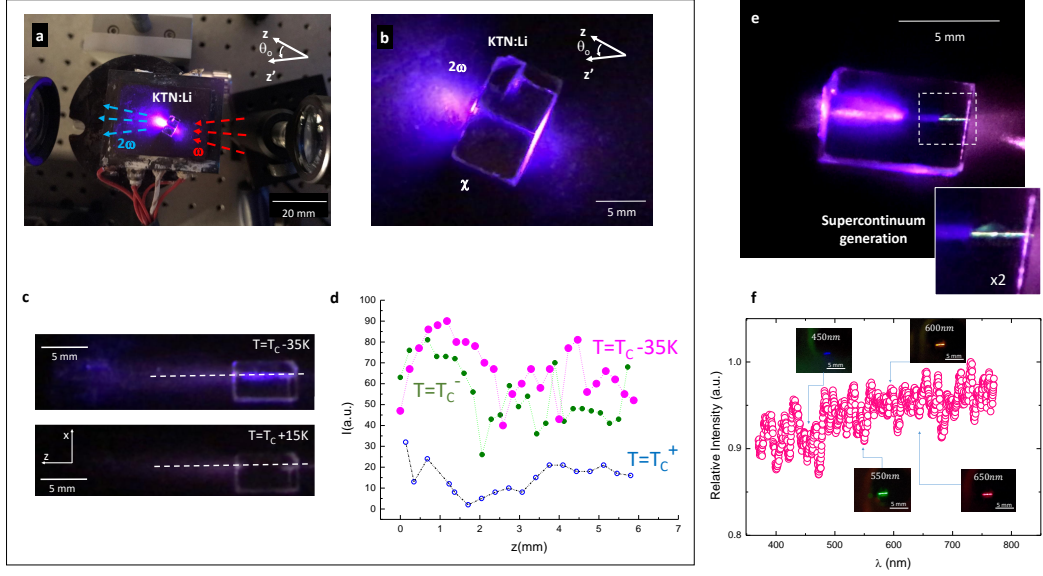


Figure 4.7. Strong SHG conversion versus limited net conversion efficiency. (a), (b) Top view of pump and SHG signal scattered light ($T = T_C - 35K$, sample 2). (c) Scattered light from the body of sample 2 of SHG signal, almost constant for $T < T_C$ from the input facet of the sample to the output facet, while disappears when the sample is heated above the Curie point T_C . (d) Analysis of the scattered light versus propagation distance in the sample for different temperatures indicates a characteristic absence of propagation dynamics for the ferroelectric case ($T = T_C - 35K$, magenta full circles), for the Curie temperature on heating from the ferroelectric phase (T_C^- , heating from $T_C - 35K$ to T_C) and on cooling from the paraelectric phase (T_C^+ , cooling from $T_C + 10K$ to T_C). (e) Evidence of supercontinuum generation. (f) Spectrum and multispectral images (~ 10 nJ/pulse pump at input).

We recall that SHG with remarkably wide angular and spectral acceptance can be observed in multidomains ferroelectrics [110, 112]. The enhanced tunability in these studies is associated to phase-matching supported by the underlying disordered domains structure, while in our experiments, phase-mismatch (the transverse component Δk in Fig. 4.1) persists. The tunability here is then a product of giant refraction that does not involves Bragg scattering. It serves to further compare our findings to highly versatile SHG in nonlinear photonic crystals [113, 114]. Here the physical origin of efficient SHG is phase-matching mediated by vector components of the reciprocal lattice in the linear or nonlinear response. It follows that the extent of the pump beam must be larger than the lattice constant. In our case the $15 \mu\text{m}$ beam hardly occupies even a single lattice site ($\Lambda \simeq 50 \mu\text{m}$).

4.1.10

Extreme nonlinearity

To provide an estimate of the effective nonlinear susceptibility $\chi_{GR}^{(2)}$ we can make use of the simplified plane-wave model (diffraction is absent in the GR regime) described in Ref. [85], pages 77-79. For sample 1, the time averaged powers at the output are $P_\omega = 510mW$ and $P_{2\omega} = 2\mu W$ for the 190 fs pulse train operating at 80 MHz repetition rate, while the beam waste is taken to be $w_0 \simeq 15\mu m$. For the purpose of the evaluation of peak intensity and Fresnel reflection, the regions leading to SHG for the TM case have $n_\omega \sim n_{2\omega} \sim n_{GR}$, where $n_{GR} \gg 1$. Of the input pump beam, only a portion actually interact with the tetrahedral structures allowing SHG (the d_{33} solids in Fig. 4.4 (b)). The fraction of active area can be evaluated measuring the Fresnel reflection at input and output facets, comparing it to what expected for regions with standard reflection (i.e., for $n \simeq 2.2$) and those regions that have d_{33} and hence an enhanced reflection associated to n_{GR} . While longitudinal phase-matching is guaranteed by the Cherenkov-like geometry (Fig. 4.1), the aperture of the pump and SHG beams remains finite ($\Delta\theta' \sim \Delta\theta_{ext}/n_{GR}$, where $\Delta\theta_{ext} \simeq 0.07$). This introduces a residual longitudinal mismatch. The transverse wavevector mismatch can be evaluated considering $\theta_c \simeq 0.28$ rad measured outside the sample, leading to $\Delta k \simeq 4.4\mu m^{-1}$. The result is $\chi_{GR}^{(2)} \simeq 5.2$ pm V⁻¹ n^2_{GR} . Considering even the minimum value of n_{GR} as measured from diffraction and Snell refraction ($n_{GR} \simeq 26$), we obtain an effective $\chi_{GR}^{(2)} \simeq 3.5 \times 10^3$ pm V⁻¹, to be compared to the measured value of standard KTN, i.e., $\chi_{KTN}^{(2)} \simeq 168$ pm V⁻¹ ($n \simeq 2.3$) [115].

4.2

Future developments

The $n \gg 1$ regime forwards a wide range of hereto unobserved and highly versatile nonlinear effects that side other pioneering experiments, such as mismatch-free nonlinear propagation in zero-index materials [116]. In our investigation of SHG in conditions of giant refraction, the converted light appears in the form of Cherenkov radiation even in the presence of phase-mismatch. This reduces constraints on launch angle, a feature that can considerably mitigate alignment requirements in nonlinear-based light sources. Furthermore, the SHG manifests increased tolerances in wavelength and polarization, a property that can be implemented to support multiple simultaneous nonlinear processes, with specific impact, for example, in the conversion of infrared images to the visible spectrum. While preliminary findings in ferroelectric KTN:Li indicate a route to strongly enhance nonlinear response, this goal is curtailed in present schemes by the residual presence of a strong transverse wave-vector mismatch. This limitation not only reduces the overall achievable SHG efficiency, but more importantly hampers the exploration of the more general class of nonlinear processes, these including parametric and even higher-order effects.

Dynamics of the super-crystal phase: clustering and percolation analysis

In order to investigate the physical mechanisms allowing GR in nanodisordered perovskites, especially the role played by ferroelectric clusters and polar-nanoregions, in this Chapter we experimentally explored the ferroelectric cluster dynamics during a structural transition. In particular, using giant broadband optical refraction, we performed 3D orthographic projection imaging in ferroelectric KTN:Li to provide, for the first time, direct evidence of fractal percolation.

5.1

Observation of Fractal-Dimensional Percolation in the 3D Cluster Dynamics

A basic open question is if there exist a general class of dynamics at the microscopic scale that characterizes the transition of a system from one macroscopic state to another. While continuous phase-transitions are macroscopically characterized by universal power laws that can be deduced from scale-invariance in their statistical field description, no analogous universality is known to exist in the microscopic details of how the transition occurs, i.e., in its underlying space-time dynamics [117]. The issue has been investigated in ferroelectrics where the transition is from a non-polar or paraelectric crystal state to a polar ferroelectric one [6, 118]. One candidate microscopic process driving the transition is polar cluster percolation [32, 33], a mechanism that being self-similar, has intriguing and hereto unexplored analogies to statistical scale-invariance [119]. Ferroelectrics form an ideal setting for the study of percolation. For one, the process is triggered by changes in the average cluster size and can therefore be activated by changes in temperature, pressure

and external electric fields. Furthermore, since ferroelectrics naturally form also bulk macroscopic crystals, percolation can be analyzed in a full 3D environment, that is, for clusters that interact and reorient in all three spatial directions [120–124]. Dielectric spectroscopy has allowed the indirect identification of percolation in ferroelectric transitions of bulk crystals [125]. Direct evidence of percolation dynamics in a full 3D geometry is yet unavailable. The basic experimental difficulty lies in extracting geometrical cluster data from a volume, and this for different external parameters. While microscopic details of a percolation can be observed from a volume by sectioning the sample and scanning the surface [126, 127], a full statistical analysis as a function of temperature and electric bias requires a non-invasive imaging approach. Ferroelectric clusters can be optically imaged using crossed-polarizers [29], a technique based on the fact that a polar cluster can change the state of polarization of propagating light due to its birefringence. The problem is that each single cluster can form in a volume with a size that can range from tens to hundreds of nanometers. This makes direct wide-area imaging generally unfeasible, as the clusters can occupy any position in the volume and transmitted light will normally pass through different arbitrarily oriented domains. As we have seen in section 1.3.2, recent studies have shown that some ferroelectrics form highly organized three-dimensional cluster distributions, ferroelectric super-crystals (SCs) [51, 128, 129]. Furthermore, as mentioned in Chapter 3, light propagating through these suffers a GR, where waves travel along the principal axes of the crystal without diffracting and separating into polarization maintaining components (see Chapter 2), amounting to a natural 3D orthographic projection. This opens up the possibility of observing optically the microscopic details of SC cluster percolation even though it is taking place on the micrometer scale in a full 3D volume.

5.1.1

3D orthographic cross-polarizer projection

The experimental setup is illustrated in Fig. 5.1 (a). Laser light ($\lambda = 532$ nm) is made to propagate along the z axis through the zero-cut KTN:Li crystal sandwiched inbetween two crossed polarizers (P1 and P2). The $2.33(x) \times 1.96(y) \times 2.03(z)$ mm³ sample has an average composition $\text{K}_{0.997}\text{Ta}_{0.64}\text{Nb}_{0.36}\text{O}_3:\text{Li}_{0.003}$ and is biased by a time-constant electric field E along the x axis.

Crystal temperature T is set by a current-controlled Peltier junction in contact with one of the y -facets. Light from the crystal output facet is imaged by lens (L1), which forms an image of the output crystal plane onto the front-view CCD (Charge Coupled Device) camera. The 3D orthographic cross-polarizer projection technique that allows the observation of cluster percolation is illustrated in Fig. 5.1 (b). The fundamental cell of the SC is illustrated in Fig. 5.1 (b) (top left panels): a total of 24 ferroelectric domains are interlocked together forming a cubic structure, where 4 domains have a spontaneous polarization (\mathbf{P}_s , white arrows) oriented along one of the 6 specific directions compatible with the tetragonal phase.

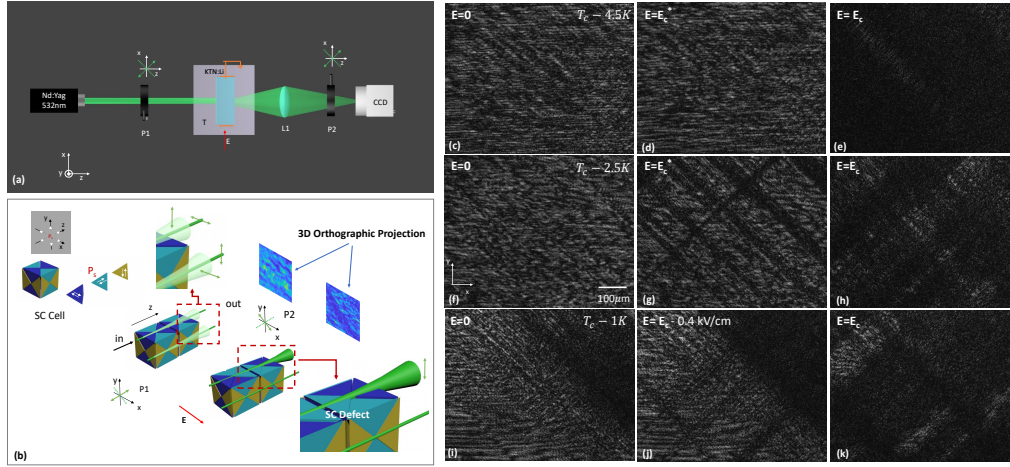


Figure 5.1. Direct imaging of SC ferroelectric cluster dynamics. (a) Experimental setup. (b) 3D Orthographic crossed-polarizer projection technique (see text). (c-k) Crossed-polarizer transmission microscopy images in various conditions of temperature and bias electric field (see text).

The domains can then be classified into three different classes, those with spontaneous polarization parallel to the x axis (blue), to the y axis (yellow), and to the z axis (light blue). As illustrated in the central panel, light propagating with a linear polarization (green double-arrow) at 45 degrees with respect to the x and y axes (as transmitted by polarizer P1) will suffer GR only for the component of the polarization parallel to the local spontaneous polarization \mathbf{P}_s . For each SC cell, this field component will propagate with negligible diffraction along the z axis of the sample normal to the input facet (dark-green component), while the component of the field with a polarization orthogonal to the local SC spontaneous polarization will suffer standard diffraction and refraction [77] (light-green component). The transmitted light at output will then be a checkerboard-like polarization pattern, with an alternating linear polarization parallel to the x and y axes, superimposed on a diffracted background component with a polarization parallel to the input polarization. The output linear polarizer P2, oriented so as to allow light polarized orthogonal to the input linear polarization to pass, will then block the component not suffering GR and allow the transmission of 50 % of the component suffering GR. The situation is altered when the sample is subject to an external electric field E directed along a crystal principal axis (bias field red arrow in Fig. 5.1 (b)). The vortex structure, now subject to a directional (x -directed) stimulus, undergoes a characteristic distortion (SC Defect in Fig. 5.1 (b)) [130]. The result is that the specific portion of the field undergoing GR that encounters the defect in the volume finds itself with a polarization that no longer supports GR, diffracts, and leads to a dark region in the transmission pattern. The region is, in turn, still well defined in the transmission image as the cells supporting GR that surround it allow light to proceed undistorted and unaffected to the output (right panel in

Fig. 5.1 (b)). Basic phenomenology is reported in Fig. 5.1 (c-k), where polarization transmission images through the sample are shown for various temperatures below $T_C = 294\text{K}$. As reported in Fig. 5.1 (c-e), for temperatures deep into the ferroelectric phase ($T = T_C - 4.5\text{K}$), crossed polarizer images indicate the existence of a single bias-induced transition at $E_c = 2.85\text{ kV/cm}$, with no specific anisotropic features. At this critical field, the crossed polarizer image becomes wholly opaque, and hence the SC structure, that generates an overall unpolarized transmitted beam, is lost. A very different picture emerges at $T = T_C - 2.5\text{K}$, as reported in Fig. 5.1 (f-h). Here at the field value $E_c^* = 2.45\text{ kV/cm}$ crossed-polarizer transmission begins to decrease along specific directions at 45 degrees with respect to the crystal x and y axes. The SC structure appears to suffer bias-induced distortions preferentially along these slanted directions. The overall picture still allows light transmission (Fig. 5.1 (g)). Increasing the bias field further, the dark regions grow along the oriented directions and ultimately expand to encompass the entire transmitted image at $E_c = 2.80\text{ kV/cm}$ (Fig. 5.1 (h)). In turn, even closer to the Curie point, at $T = T_C - 1.0\text{K}$, the two-step dynamic is no longer discernible (Fig. 5.1 (j)), and a single anisotropic/fully dark transmission intervenes above $E_c = 2.40\text{ kV/cm}$ (Fig. 5.1 (k)).

5.1.2

Percolation analysis

Percolation analysis of the transition from a regime of light transmission to one of no-light transmission through the cross-polarizers, associated with the breakdown of the SC structure, is reported in Fig. 5.2. Observed images (Fig. 5.2 (a-c)) are processed for analysis. In order to delineate the percolative region, we first binarize the collected images selecting a threshold intensity: a pixel is considered in state 1 if it has an intensity lower than the threshold and in state 0 otherwise. The threshold intensity is taken to be the background intensity of the unbiased SC pattern (average intensity of the dark regions in Fig. 5.2 (a)). To identify the clusters size in the binarized transmission images, we define connected pixels that make up a cluster using the Von Neumann neighbourhood criterium: square-shaped pixels are considered connected when they share their binarized state along an edge, while pixels that share a vertex, i.e., are adjacent and have the same state along the diagonal of the pixel lattice, are not considered connected.

The processed images thus partitioned into clusters are reported in Fig. 5.2 (d-f). Now the mean cluster size S (system susceptibility) is defined as $S = \sum_s w_s s$, where w_s is the probability that an image pixel belongs to a cluster of size s (the ratio of the number of pixels belonging to clusters of size s divided by the total number of pixels). A cluster is taken to be percolating (the infinite cluster) when it is found to spread from one external boundary of the processed image to another, as occurring in the x-y direction for the anisotropic dynamics of Fig. 5.2 (e) and Fig. 5.2 (f). For this cluster we then determined its so-called strength $P_\infty = n_\infty/N$, where n_∞ is the number of pixels in state 1 that belong to it and N the total number of pixels in the processed image. Dynamics are analyzed in terms of the composition p , i.e., the probability that a site in the lattice is in the 1 state. In these terms, the average cluster size will diverge following the power law $|p_c - p|^{-\gamma}$ at the percolation threshold p_c , and P_∞ will grow for a composition above p_c as $(p - p_c)^\beta$ [119]. The

exponents γ and β depend on the dimensionality and type of underlying lattice [119]. Results for S are reported in Fig. 5.2 (g) as a function of bias electric field E . Fitting the data with a $|E_c - E|^{-\gamma}$ law gives a critical exponent $\gamma = 1.24 \pm 0.10$ and $E_c = 2.82$ kV/cm. Cluster strength P_∞ versus E is reported in Fig. 5.2 (h). Data can be fitted for fields $E > E_c^*$ by $(E - E_c^*)^\beta$, with $\beta = 0.67 \pm 0.05$ and $E_c^* = 2.45$ kV/cm, i.e., with a threshold field $E_c^* \neq E_c$.

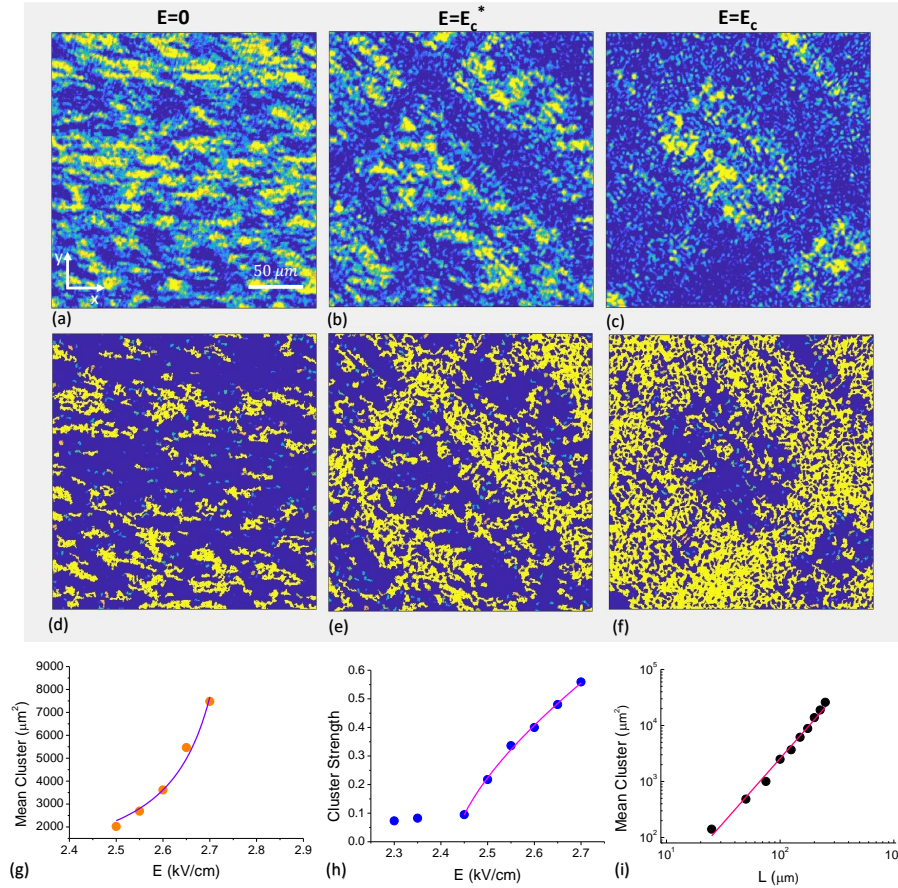


Figure 5.2. Percolation analysis of SC breakdown. (a)-(c) Crossed polarizer wide-area transmission images for different bias electric fields at $T_C = 2.5\text{K}$ and (d-f) binarization (see text). (g-i) Critical exponent analysis (see text).

This signals the existence of two distinct percolative transitions, the lower field transition occurring at E_c^* preferentially along directions at 45 degrees relative to the principal x and y axis (Fig. 5.2 (e)), and the isotropic transition occurring at the higher field E_c . In Fig. 5.2 (i) we report the mean cluster S at the critical value E_c as a function of the length scale L . Results are fitted by a power law for $L > 20\mu\text{m}$ (1 pixel = $0.5\mu\text{m}$), with an exponent $\gamma/\nu = 1.94 \pm 0.10$. The result is in agreement with predictions for finite-system susceptibility at the percolation critical point, that scales as $S \propto L^{\gamma/\nu}$, where L is the size of the system [131]. Percolation analysis is consistent with results obtained in [33] for electric field-induced percolation in $\text{Ba}(\text{Zr}, \text{Ti})\text{O}_3$ and also with values assumed in [32] for temperature-induced percolation in $\text{Pb}(\text{Mg}, \text{Nb})\text{O}_3$.

5.2

Self-similarity

A basic consequence of the appearance of critical exponent behavior is that the field-induced transition from the SC state is characterized by scale-invariance, a feature it shares with conventional phase-transitions. In turn, percolation also manifest self-similarity, by which the actual geometry of the percolating cluster is the same as seen on different magnification scales. In these terms, the size of the largest cluster will in general scale $\propto L^{\mathcal{D}}$, with $\mathcal{D} < d$, i.e., smaller than the spatial dimension of the hosting space ($d = 3$). Since we are observing the 2D projection of the cluster percolation, we can measure the fractal dimension of the percolating cluster only for $\mathcal{D} < 2$ [132–134]. In Fig. 5.3 we provide a Kolmogorov capacity analysis of the transmission images using the box counting method [132, 135]. As reported in Fig. 5.3 (a), while for fields above and below the threshold field E_c^* the local slope changes for different box scales, for $E \simeq E_c^*$ it has an almost constant value, as expected for a fractal-dimensional percolation.

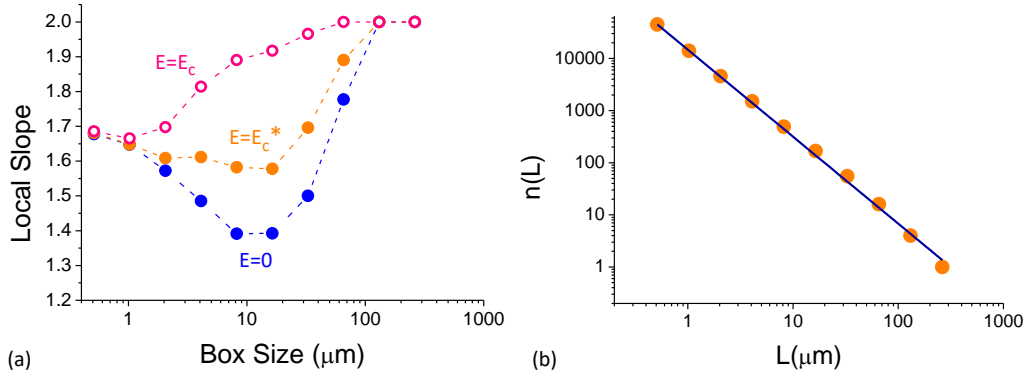


Figure 5.3. Fractal dimensional nature of the percolation transition. (a) Local slope versus box-size. (b) Number of boxes needed to cover the set as a function the size of the boxes of L (see text).

As reported in Fig. 5.3 (b), fitting the number of boxes $n(L) \propto L^{-\mathcal{D}}$ needed to cover the infinite cluster P_∞ versus the length scale L gives a fractal dimension $\mathcal{D} = 1.65$ ($\mathcal{D} < 2$). Interestingly, observed fractal dimension is in agreement with interpretative models of dielectric spectroscopy response in analogous materials and, indeed, with numerical simulations of other complex relaxor materials [125, 136]. In turn, fractal-dimensional analysis of the second percolative process associated to E_c yields $\mathcal{D} = 2$, so that the fractal nature of this second transition cannot be detected in our (projective) setup.

5.2.1

Role of the 3D vortex structure

The interpretation of results can be formulated assuming the 3D vortex structure of a ferroelectric SC, as originally formulated in Chapter 3.

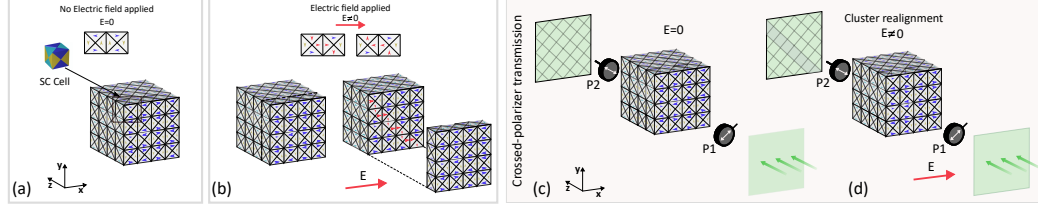


Figure 5.4. Percolation picture in a biased SC. (a),(b) Illustration of directional percolation and (c-d) its effect on crossed-polarizer transmission (see text).

In the 3D SC matrix, illustrated in Fig. 5.4 (a), the application of an external bias electric field will then distort the domain mosaic in a domino-like effect: the defect will propagate along the diagonal direction, as schematically illustrated in Fig. 5.4 (b). Since the defect in general enucleates inside the unperturbed SC in a random position in the volume along the z axis, this will cause a dark region in the crossed polarizer images (Fig. 5.4 (c-d)). Hence, once the first percolation transition is reached at E_c^* the diagonal defects, that cause dark regions in the transmitted image, expand from one edge of the investigated volume to the other. In turn, the second percolative transition occurs as all the tassels in the mosaic align with the external field, a condition in which the entire transmitted image becomes darker. The percolative chain, as in Fig. 5.4 (b), forming at a given position z^* along the propagation axis z , will halt GR at that z^* and cause the light originally transmitted by that specific SC cell to diffract and be blocked by the output polarizer (Fig. 5.4 (d)). This interpretation is corroborated by experimental results on the observation of the behaviour of the GR under the effect of an external electric field, as we will see in the next section.

5.2.2

Effects of super-crystal breakdown on giant refraction

The effects of SC percolative-breakdown on GR for focused light beams is analyzed using a high-aperture long-working distance microscope objective (OBJ, Edmund Optics -100X- 3mm working distance -achromatic- NA= 0.8).

While the sample is optically transparent above T_C (absorption coefficient $\alpha \simeq 2\text{cm}^{-1}$), scattering associated to ferroelectric clustering increases below T_C ($\alpha \simeq 10\text{cm}^{-1}$ at $T_C - 4.5\text{K}$). This allows the observation of beam dynamics inside the sample through top-view images of stray scattering, as reported in Fig. 5.5. An important parameter to separate light undergoing GR from the one not suffering GR in top-view experiments is the rotation angle of the KTN:Li sample around the

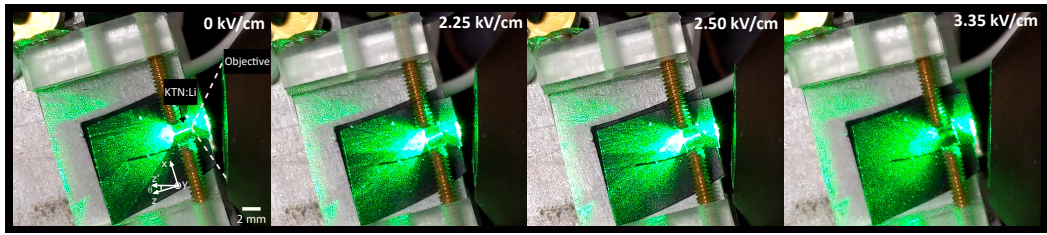


Figure 5.5. Top-view images of scattered light across the percolative transition (see text).

vertical y axis, θ (see Fig. 5.5, first panel), i.e., the angle between the normal to the sample input facet (z) and the experiment propagation axis (z'). The breakdown of GR for $E > 2.50$ kV/cm coincides with the onset of cluster percolations.

5.3

Microscopic origin of self-similarity

Findings shed light on the nature and susceptibility of ferroelectric super-crystals [51, 77, 93, 103]. They suggest a specific role of organized 3D polarization structures below the Curie temperature [14, 63, 137]. In more general terms, the direct observation, in the transparent volume, of percolating cluster dynamics sheds light on the microscopic origins of self-similarity in natural 3D systems. Furthermore, 3D polarization vortices can have profound repercussions on our understanding of volume samples and the development of future energy and information storing technology [53, 138].

Characterization of bulk KTN

While numerous results are found on the super-crystal phase associated with the macroscopic optical, dielectric and piezoelectric response, little is known about the effect that the coherent mosaic of micrometer-scale domains has on the average atomic structure. In this Chapter we report an indepth 3D structural investigation of bulk KTN cooled below its Curie point using X-ray diffraction data. To correlate average atomic structure data to macroscopic (micrometer and above) SC patterns, we also performed optical diffraction, optical second-harmonic-generation, dielectric measurements and calorimetry measurements. Results indicate that the emergence of the ordered 3D ferroelectric cluster patterns is accompanied by a previously unreported large scale and coherent lattice deformation. The signature is that the standard perovskite sequence of lattice symmetries on cooling, i.e., cubic-to-tetragonal, tetragonal-to-orthorhombic, orthorhombic-to-rhombohedral [7], is transformed to cubic-to-orthorhombic, orthorhombic-to-tetragonal, and tetragonal-to-rhombohedral. In our modeling, we describe how this unconventional deformation in the average atomic structure is compatible with the strain field caused by the vortex polar domain distribution typical of a super-crystal.

6.1

Observation of an exotic lattice structure

6.1.1

Experiments

Materials

The investigated sample is a single-crystal solid-solution KTN ($\text{KTa}_{1-x}\text{Nb}_x\text{O}_3$, $x = 0.36$) compound was grown through the top-seeded solution method. The concentration of Potassium, Tantalum and Niobium in the crystal was determined by electron microprobe analysis. Two c -direction-pulled zero-cut samples are extracted

from the original rod, a $1.8 \times 1.8 \times 2.3$ mm specimen to perform dielectric spectroscopy measurements, and a $0.5 \times 0.5 \times 1.6$ mm specimen that formed the starting batch material for X-ray diffraction (XRD) and calorimetry (DSC) measurements.

X-ray diffraction

A 100+ Bragg-peak X-ray 3D structural investigation of a single-crystal KTN is reported in Fig. 6.1 (a-c). The starting batch consisted of a transparent, hard and brittle mm-long rod of the freshly synthesized KTN material. The opposite extremities were cut with a stainless steel microblade. Irregular crystals of micrometer dimensions were obtained. Twelve of them were discarded after preliminary checks due to heavy twinning. Eventually, one high-quality non-pleochroic specimen was selected for the data collection. The linear size does not exceed $100 \mu\text{m}$ to alleviate the very high absorption of KTN ($\mu \simeq 29 \text{ mm}^{-1}$) at the X-ray wavelength here employed ($\lambda = 0.71073 \text{ \AA}$).

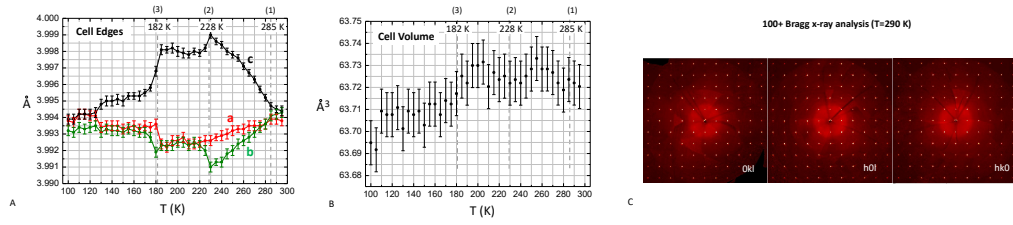


Figure 6.1. Coherent lattice distortion in ferroelectric KTN. (a) Cell edge lengths (\AA), a (red dots), b (green dots) and c (black dots) of KTN as a function of T . Each point was estimated by single-crystal X-ray diffraction from a least-squares fitting against ~ 110 reflections within $2\theta \simeq 34^\circ$. Error bars correspond to one estimated standard deviation (e.s.d.). Vertical dashed lines mark the first-order phase transitions that were detected by differential scanning calorimetry (DSC) and dielectric spectroscopy (see Fig. 6.3 (a-b) in section 6.1.1). (b) Volume (\AA^3) of the crystallographic unit cell of KTN as a function of T . Due to the anisotropic response of the cell axes, the overall thermal expansion is zero down to the low- T transition at 182 K. (c) Reconstructed precession images of three equatorial sections of the KTN reciprocal lattice at room temperature, as viewed down the a^* , b^* and c^* reciprocal cell edges. Changes in the positions of the peaks as the sample is cooled down are not appreciable by the naked eye.

Each crystal was mounted on the top of a glass capillary fiber with bicomponent epoxy glue and placed in very close proximity of the cold nitrogen nozzle. A three-circle Bruker AXS Smart diffractometer equipped with an APEX II CCD detector and an Oxford Cryosystem N_2 gas blower was used throughout. Graphite-monochromated Mo K_α radiation ($\lambda = 0.71073 \text{ \AA}$) at a nominal power of the generator of $50 \text{ kV} \times 30 \text{ mA}$ was employed. Diffraction amplitudes were collected in the ω -scan mode from the hemisphere up to a maximum Bragg angle of $\simeq 37^\circ$ (area detector fixed at $2\theta = 0^\circ$, sample rotating around the goniometer z-axis by varying ω) and the temperature was changed stepwise from 295 K to 100 K, with $\Delta T = 5 \text{ K}$; before starting any data acquisition, the sample was equilibrated in the cold N_2 stream for $\simeq 10'$. Possible hysteresis phenomena were excluded by repeating

data collections at specific temperatures after having warmed back the specimen at room temperature [139–142]. Data integration and reduction were carried out by the SAINT+ suite of programs. The 0.5 mm diameter probe is positioned 50 mm from the sample: illuminating the whole sample gives an average lattice analysis on the entire sample. The diffraction data were uniformly distributed in the reciprocal lattice up to $\max[\sin(\theta)/\lambda] = 0.45^\circ \text{\AA}^{-1}$ (see below), and each of them represents the scattering output from the entire volume of the bulk material. We were thus able to measure very precisely the cell edge length down to 100 K, obtaining for the first time reliable estimates of the T-driven lattice distortions in KTN. Eventually, we collected a total of 100+ X-ray Bragg peaks at each temperature. The lattice constants were computed by minimizing the average square deviations between the measured reflection centroids and those predicted on the basis of the lattice model. In the standard least-squares procedure, lattice constants are varied together with instrumental parameters, which include possible detector misplacements and centering errors of the crystal. In KTN, T-driven distortions of cell edge lengths are very small ($\leq 0.1\%$), and of the same order of magnitude as the least-squares estimated adjustments affecting the instrumental parameters. This results in high correlations, which imply an odd dependence of the instrumental parameters on the cell edges and vice-versa, as well as very high estimated standard deviations of the final least-squares variables. To limit these problems, we measured the positions of the Bragg peaks in the reciprocal reference frame using a very small scan width in ω ($\Delta\omega = 0.15^\circ$). Possible systematic errors in the position of the instrumental zero were minimized by collecting reflections at both positive and negative 2θ . Fast exposure times (3 s/frame) were used to ensure that counting statistics always remain in the linearity region of the CCD detector device. Finally, instrumental parameters were optimized at RT and then kept fixed in least-squares refinements at lower T (more details in the Supporting Information). This way, the diffraction maxima can be accurately located, even for the most intense reflections. The very low (< 0.001) cell microstrain (Fig. 6.1 (a-c)) implies that transition-induced crystal twinning, if any, is not detectable. This is because the associated reciprocal space splitting of the Bragg peaks would be lower than 0.002 rad, corresponding to a deviation comparable with the detector pixel size (0.12 mm). Cell volume across the entire range of inspected temperatures is reported in Fig. 6.1 (b) [13, 143–149].

Optical diffraction

The macroscopic formation of extended 3D ferroelectric cluster patterns below T_C in the KTN sample are observed using visible light propagation, as reported in Fig. 6.2 [51]. While domains in KTN can be directly observed using transmission polarization microscopy in thin plates [150], periodic domain patterns in the volume can be optically detected using coherent scattering, as originally demonstrated in KTN by Bouziane et al. [151].

We note that the patterns occur spontaneously, i.e., without fabrication or post-processing protocols (such as laser-induced domain pattern orientation), on cooling through T_C . Light transmission is analyzed illuminating the sample with a polarized plane-wave from a frequency-doubled Nd-YAG laser ($\lambda = 532$ nm). Transmitted light parallel to a specific crystal axis is collimated and imaged onto millimeter paper placed

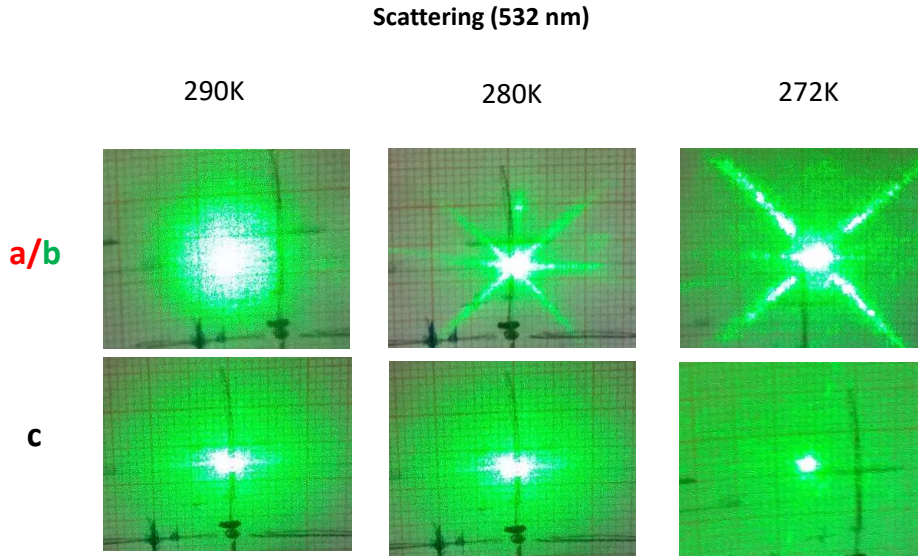


Figure 6.2. Output of light scattering experiments close to the Curie point.

after the sample. Different directions are inspected rotating the sample. Crystal temperature in the range 265-300K is fixed through a water-cooled current-driven Peltier junction placed below the sample holder. Temperatures are measured relative to T_C that is evaluated optically through cross-polarizer transmission microscopy. To avoid strong water condensation, optical diffraction is investigated for temperatures down to 270 K. Optical diffraction patterns are evident for two directions, while the diffraction peaks are accompanied by background scattering. Far-field images provide the angular scale of the Bragg diffraction. The angular peak-to-peak distance identifies a spatial scale $\Lambda \simeq 5.2\mu\text{m}$, which is in agreement with scale of the growth striations associated to the standard bulk sample pulling process [51]. Results are incompatible with propagation through a disordered mosaic of ferroelectric clusters and in agreement with the slow metastable relaxation into the fully ordered 3D SC cluster mosaic previously observed in other samples in proximity of the Curie point [51].

Calorimetry and dielectric measurements

Calorimetric measurements of the KTN sample are reported in Fig. 6.3 (a). Differential scanning calorimetric (DSC) measurements were carried out in the 143 K-room-temperature (RT) range using a Mettler Toledo DSC1 apparatus with Star^e software (version 11.0). The entire crystal was placed into a 40 μl aluminum pan, carefully positioned flat on the bottom in order to maximize heat transfer with the instrument. The sample is thermalized 5 minutes at 143 K, heated to 323 K, and finally cooled back to 143 K at 2, 5, 10 and 15 K/min rate. Sharp transitions were located by averaging the onset temperature measured during heating and cooling

ramps at various rates [152–154].

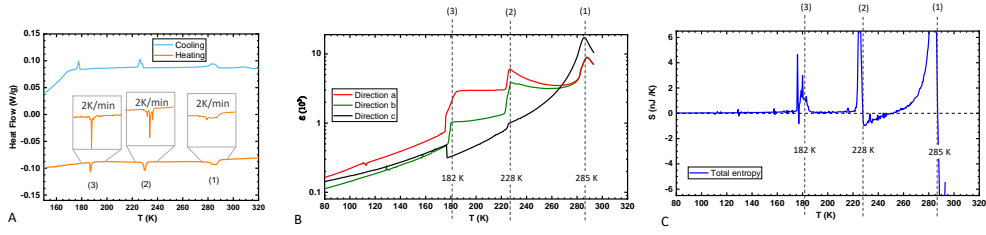


Figure 6.3. Macroscopic response. (a) DSC thermogram of KTN in the 143 K-RT range of T ; (1), (2) and (3) indicate endothermic first-order phenomena at 285, 228 and 182 K. Insets represent a close up of the transitions when studied at 2 K/min. (b) Dielectric response as a function of T along three orthogonal main crystalline axes at the sample frequency of 10 kHz. (c) Total entropy calculated through the sum of the induced Fröhlich entropy $S_E = S_E(T)$ along the three crystalline axes [155, 156] as a function of T .

Dielectric response for the KTN sample in the 228-285 K range is reported Fig. 6.3 (b). The real part of the permittivity versus temperature T is measured by a precision LCR meter (Agilent-4284A) applying a probing electric field of 1 V/cm between plane parallel electrodes deposited on the sample facets. Temperature variation in the 75-320 K range is obtained employing a closed two-stage helium cryostat. The thermal variation rate is 1 K/min and monitored through a calibrated silicon diode sensor (0.01 K in precision). The dielectric response is measured along the three crystalline main directions a , b , c , in three different consecutive scan stages, keeping all experimental parameters constant, especially the thermal variation rate and the strength of the probing field. Each set of measurements is carried out for the frequencies 1, 10, 100 and 1000 kHz and the acquisition rate is two measurement points for 1 K [5, 34].

Second-Harmonic generation experiments

Second-harmonic-generation (SHG) experiments are performed in a $7.0 \times 3.9 \times 1.6$ mm sample designed to have a higher T_C ($T_C = 333$ K) adding a small concentration (<0.01) of Li to the melt (KTN:Li). The details of the local polar domain structure of the SC are analyzed using SHG experiments reported in Chapter 4.

6.1.2

Discussion of the X-ray experiments results

Cell-size analysis for the KTN sample reported in Fig. 6.1 (a) indicates that while the standard cubic to tetragonal transition is observed in cooling the sample below $T_C = 285$ K, this symmetry is superseded at 270 K by a stable orthorhombic distortion that persists to lower temperatures, down to $\simeq 230$ K. Here, cooling below $T = 228$ K, symmetry is found to increase as a low- T tetragonal phase emerges from the high T orthorhombic one. Since the statistical significance of the observed distortion of the unit cell refers to a redundant analysis of Bragg

peaks, each collecting the scattering contribution from the whole sample, this implies that the lattice distortion, which includes the anomalous increase in symmetry on cooling, coherently pervades the entire bulk material. An increase in symmetry on cooling is not forbidden on absolute grounds. In fact, according to Group Theory, it is only required that low-symmetry phases lie both in a symmetry subgroup of the high- T prototype one [157]. Even so, while short-range distortions are known to locally lower the symmetry, it is unusual to observe an increase in long-range symmetry upon cooling in the context of perovskite research. In detail, mainstream theories, including the Landau theory, describe non-reconstructive structural phase transitions in homogeneous systems identifying an order parameter. Experimentally, such transitions imply the occurrence of a symmetry relationship relating the involved phases. In ferroic transformations, like in ferroelectrics, this relationship is strictly a point group-subgroup one. According to Aizu [158] (and references therein), the crystal structures of transition-related phases must all be described by slight distortions of a prototype reference structure, necessarily the most symmetric one. A distortion here means that the ferroelectric phase (the low- T one, i.e. that existing below the Curie temperature) is expected to bear a lower symmetry, i.e. to belong to a point group of lower order. Mixed perovskites, in turn, such as the Mg/Pb niobates that have attracted continued attention in recent years, are known to be chemically and structurally heterogeneous on different length scales at the same time [13]. This leads to an anomalous physical response, over a broad range of temperatures, that cannot be fully described by a Landau-like approach. For one, no obvious order parameter can be identified. As regards specifically to our results in KTN, the phase sequence from RT to 100 K (Fig. 6.2 (a)) is cubic-orthorhombic-tetragonal-tetragonal-rhombohedral, which corresponds to an alleged sequence of point groups $m3m \supset [mm2 \subset (4mm = 4mm \supset 3m)]$. All the low- T phases thus belong to a subgroup of the prototype $m3m$ one, a circumstance that apparently agrees with the Aizu paradigm. In fact, two fundamental differences emerge: First, a non-ferroic transition occurs at low T , which relates two different tetragonal ferroelectric phases; Second, all the phases below ~ 230 K are supergroups of $mm2$, the one appearing just below the Curie point. To the best of our knowledge, this phenomenon has never been reported for BaTiO₃ and BaTiO₃-type single-crystal ferroelectric materials, which rather follow the expected sequence $m3m \supset [4mm \supset (mm2 \subset 3m)]$. That is, in ordinary perovskite ferroelectrics the low T $mm2$ and $3m$ phases can also be rationalized as small distortions of a prototype ferroelectric phase ($4mm$). Rather, in KTN, the only meaningful prototype is the paraelectric cubic one ($m3m$), implying that, below the Curie point, a very strong and unexpected cubic to orthorhombic symmetry-breaking occurs. Unexpected XRD findings can arise as artifacts of apparent pseudo-symmetries generated by a crystallographic multidomain structure. To exclude this and ensure that we were observing an actual spontaneous symmetry breaking at the atomic-scale (followed by the significant symmetry gain on cooling), we took great care in selecting true single crystals, that is, crystallographically homogeneous (single-lattice) specimens. For sure, grain boundaries and extended defects exist in our specimens, but in a much lower concentration than in a multidomain system (twinned, powdered). Moreover, X-ray diffraction outcomes (Fig. 6.1 (c)) confirm that lattice parameters have the same orientation throughout the whole bulk sample, that is, defect-bounded

crystallites are all iso-oriented. Anomalous symmetrization could be associated to a so-called reentrant transition, a thermodynamic characterization that is, in our case, not applicable. First, it is not obvious what order parameter should be defined in the allegedly “ordered” orthorhombic phase, as KTN is an intrinsically disordered solid solution already at high T . The disorder in KTN is occupational and temperature-invariant. Moreover, the very small distortions of the cell parameters (Fig. 6.1) ensure that atomic displacement is too small to produce a significant entropic drive for the transition. As we will see in the next sections, DSC results (Fig. 6.3) point out that the first-order transitions we detect upon cooling are all endothermic ($\Delta H > 0$). Accordingly, this implies that some “hidden mechanism” should exist to allow for the spontaneity of the process ($\Delta G < 0$) [159].

6.1.3

Origin of the anisotropic strain field

Model

While theoretically possible, the switching of orthorhombic and tetragonal phases upon cooling is anomalous and bears deep physical and chemical significance. In what follows we discuss how the 3D SC model is able to provide an interpretative picture of XRD data corroborated by the optical diffraction, dielectric spectroscopy, and calorimetry measurements. Ferroelectric perovskites suffer a spontaneous symmetry breaking from the cubic phase to the polar tetragonal phase at T_C . Here a strong spontaneous polarization emerges along one of the six principal crystal axes [7, 66, 160]. As a textbook example of a solid-solid phase-transition, the passage from the nonpolar or paraelectric phase to the polar or ferroelectric phase has always been thought to spontaneously give rise to a disordered distribution of polar domains in which free-energy is minimized taking into account both defects, inhomogeneities, and the actual finite size and shape of the sample [13, 45]. Optical scattering experiments in bulk KTN:Li samples suggest an entirely different picture [51, 77]. To explain what can best be described as the optical equivalent of X-ray diffraction from a crystal lattice, polar clusters appear to spontaneously organize into a macroscopic coherent 3D mosaic with a micrometric periodicity, the ferroelectric SC. A model for the phenomenon is based on the formation of a superlattice of polarization vortices. A polarization vortex is a topological defect that emerges in reaching a state of equilibrium from the non-polar to the polar phase (see illustration in Fig. 6.4 (a)). In detail, the reduction of volume/surface charge and strain leads to two basic polarization domain patterns, the 180° alternate domain sequence with a domain wall parallel to the crystal axes, and the 90° pattern, in which the wall is at 45° to the crystal axes. These two types of patterns will in general combine into complex patterns with a rich and varied phenomenology [45, 161]. The vortex is now a combination of four separate domains with a spontaneous polarization that wraps around a localized singularity where the four 45° -oriented domain-walls meet. Even though strain compatibility reduces stress at each domain wall [162], the vortex structure can cause a rotational stress associated to a finite toroidal moment that can dominate response close to the Curie point [163].

Polarization vortices in the bulk, in thin and layered geometries are known to

remain stable even below the Curie point, both as single isolated defects and in large arrays of stacked two-dimensional super-lattices [49, 51, 103, 164]. In these, they appear as reconfigurable localized domain structures for electrically controllable energy and information storage and processing (see illustration of the 2D SC in Fig. 6.4 (b)). As a result of a combination of tetragonal units, each vortex has an equally elaborate associated strain configuration that also depends on its surroundings, a phenomenon typically used to encode ferroelectric memory devices [53].

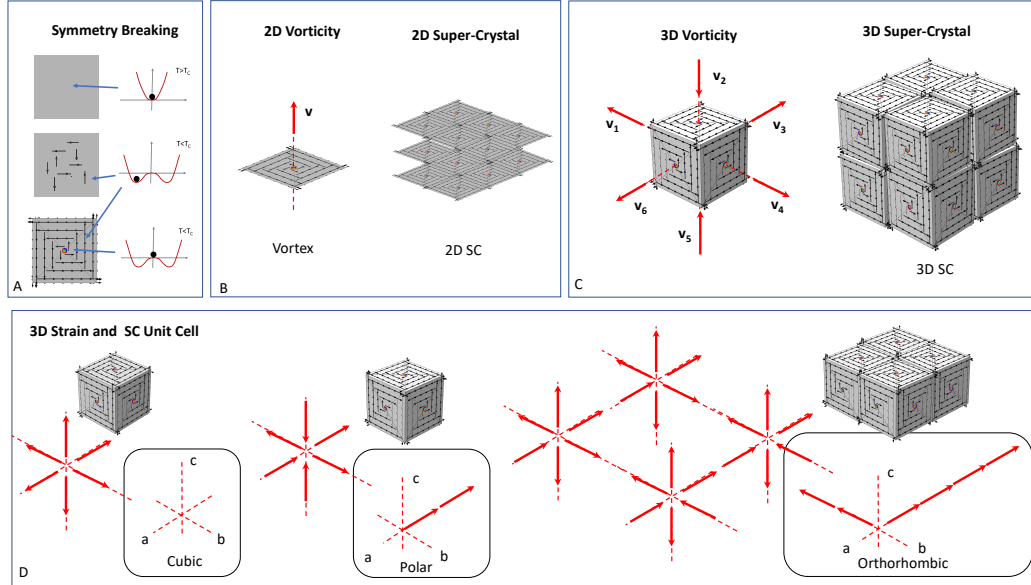


Figure 6.4. The 3D SC model and a possible origin of the anisotropic strain field. (a) Spontaneous polarization (black arrows) is formed as the Gibbs potential G vs P (dark red curve) passes from having a single minimum (top row) to having a characteristic double-minimum below the Curie point at $T = T_C$ (center). The resulting multidomain structure expands and preserves an unpolarized state in the form of a topological defect vortex (bottom). Since spontaneous polarization can only form along the crystal principal axes, the physics resembles that of Heisenberg magnets. (b) In 2D, topological defects inherit a higher-dimensional 3D vortex structure (left) that can then form a 2D SC (right). The red vector \mathbf{v} represents the local vorticity of the polarization field. (c) In the volume, defects inherit a 4D structure, forming a 3D hypervortex (left), that can then form 3D SCs (right). (d) Each unit hypervortex (left) is formed by 6 independent vortices that wrap around the central point. These can combine to form SC unit cells with a resulting strain field (boxed panels) that can be both Cubic (left, zero strain along a, b, c), Polar (center, +2 strain along a , zero strain along b, c), and Orthorhombic (right, +4 along a , +2 along b , zero along c). Since each component vortex has an associated strain principally in the plane orthogonal to its vorticity vector, in the orthorhombic case we expect a larger lattice distortion along one specific axis (i.e., the c direction).

Numerical studies of perovskites in the tetragonal phase indicate that vortex

structures are stable also in volume systems with no dominant external stimuli [124]. The formation of the 3D SC is then modeled as the 3D generalization of the 2D SC to 3D, as illustrated in Fig. 6.4 (c). The screening of volume and surface charge causes the tetragonal domains to combine into a cube-like structure formed by 6 independent vortices. In these terms, each unit cell of the 3D SC has an associated stress field caused by the specific combination of the single component vorticities. Combining different types of unit cells, it is possible to design cubic, polar, and even orthorhombic strain fields from a single tetragonal building-block (see Fig. 6.4 (d)). Hence, the exotic lattice structure can arise as a result of the anisotropic 3D stress field that accompanies the specific 3D polar cluster configuration. The effect also dominates the cell structure below the second phase-transition, at 228 K, where the perovskite passes from an orthorhombic to a tetragonal phase. Here the natural orthorhombic phase [7, 148] is superseded by an anomalous tetragonal phase below 210 K. This anomaly, that persists down to the third phase-transition temperature at 182 K, would then be the result of the stress field associated to having the single constituent parts of the SC pass from the tetragonal to the orthorhombic phase. In other words, the SC leads to an orthorhombic strain field when it is made of orthorhombic unit solids. The average distortions we report are smaller than the uncertainty of previous studies [148, 165, 166]. These have, congruently, failed to identify the structural anomaly reported in Fig. 6.1 (a). While this may reflect a strain-stress mechanism specific to the family of KTN samples inspected, or even the specific composition of our samples, it could equally represent a general trait common to other perovskites. This is because previous studies performed XRD monitoring a limited number of reflections, and if single-crystal X-ray and neutron detection is limited to the monitoring of a small number of reflections, no significant evidence of a shift from the basic high-temperature cubic lattice can be observed [166–168]. In other words, the lattice distortions reported in Fig. 6.1 (a-b) are detected only when the number of accurately measured Bragg peaks is radically increased. In any case, the distortions here discussed are also composition-dependent to some extent, as the phase sequence in perovskite solid solutions often changes with composition. The present results should thus encourage to perform accurate single crystal X-ray diffraction experiments to check whether and to what extent these structural transitions are common in the KTN class of materials.

Experimental corroboration of the physical picture

As reported in Fig. 6.1 (b), the exotic orthorhombic phase from 270 K to 228 K and the exotic tetragonal phase from 210 K to 182 K are accompanied by an anomalous compressibility. The macroscopic thermal response is strongly anisotropic, as one unit cell vector undergoes a large negative thermal expansion ($\alpha_p(c) = -1.95(1) \cdot 10^{-5} \text{ K}^{-1}$). The result is a material with an overall negligible thermal expansion ($\alpha_p(V) = +1.78(1) \cdot 10^{-8} \text{ K}^{-1}$) over the whole 100 K range, and a zero thermal expansion in the 182-285 K region. In terms of the 3D SC strain-stress field, this may be a manifestation in 3D of the negative linear response observed in layered 2D systems where the inverted potential at the vortex core (see Fig. 6.4 (a), bottom) leads to negative capacitance [48, 169]. The physical picture is corroborated by the

optical diffraction experiments reported in Fig. 6.1 (d) and the SHG experiments in Fig. 4.4 (b-c). In fact, for temperatures slightly above and below the point at which the lattice anomaly occurs, the characteristic optical Bragg diffraction that accompanies the emergent SC is found. In turn, the SHG emerges as highly structured and polarization-dependent Cherenkov radiation [97, 99], a direct signature of an underlying organized polar cluster structure specific to the 3D SC [128]. The picture is further supported repeating the XRD analysis for different portions of the original bulk crystal. Cell edge vs T anomalies are found to have different onset temperatures [170–173], indicating that the effect is driven by defects and inhomogeneities specific to the sample, as expected to occur in the formation of the 3D SC [51]. On a macroscopic scale, the idea that a strain field associated to the 3D SC drives the anomalous cell behavior implies that the underlying perovskite suffers a standard sequence of phase transitions at the three critical temperature T_1 , T_2 , T_3 . This is confirmed through calorimetric measurements of the material reported in Fig. 6.3 (a), that show a standard sequence of three solid-solid transitions typical of perovskites. Specifically, no latent heat is found in the regions between 285 and 228 K and 210 and 185 K, where the anomalous lattice structure emerges (see Fig. 6.1), thus excluding a first-order phase transition. The absence of a temperature resonance in the dielectric response in the 285–228 K range reported Fig. 6.4 (b) also excludes a second-order type transition [76]. In other words, the passage below 285 K from the tetragonal to the orthorhombic structure does not occur through a transition, but through an ordering of tetragonal clusters into the model 3D SC (and equally for the second orthorhombic to tetragonal anomaly below 210 K) [174]. Dielectric measurements further reveal strong differences along the three principal perovskite axes a , b , and c in the relative real permittivity $\epsilon = \epsilon(T)$ (Fig. 6.3 (b)). Since permittivity for polydomains samples is strongly affected by domains size, orientations, by domain walls, and even domain wall motion [165], this macroscopic anisotropy corroborates the idea of an anisotropic ferroelectric domain distribution typical of the 3D SC. The response analyzed in terms of dielectric or Fröhlich Entropy (see Fig. 6.3 (c) and [175–181]) indicates a temperature interval that overlaps with the 3D SC hypothesis (230 – 250 K) in which the reorientational entropy changes sign far from the critical points T_1 and T_2 [155, 156]. This agrees with the scenario described in Fig. 6.4 (d) (right) where two directions, a and b , have a finite resultant vorticity while the third c direction does not. Congruently, the a and b directions have a positive reorientational entropy, while a negative entropy is found in the c direction. What happens at lower temperatures, i.e., for $T < T_3$, is still under study. For example, while we expect the system to naturally proceed towards an isotropic lattice through what should be a rhombohedral phase, an unexpected structural change occurs at $T \simeq 125$ K, a rearrangement that is also detected in dielectric spectroscopy data (see Fig. 6.3 (b-c)).

Role played by topological defects

Since $\text{KTa}_{0.64}\text{Nb}_{0.36}\text{O}_3$ (KTN) is a variant of other solid solution potassium-based perovskites that are relaxors, our study sheds light on the role played by topological defects in determining complexity-driven phenomena and non-ergodicity. In the language of relaxor physics, the average ordered high T perovskite structure can host a population of uncorrelated polar nano-regions (PNR) [13]. Upon cooling, different PNRs start to interact persistently with each other and, below the Curie temperature, they can produce self-organized macroscopic polarization domains. The 3D vortex pattern is then that PNR structure that screens volume and surface charge and minimizes stress, while different vortices can self-organize into the SC that eventually occupies the whole bulk volume. It is this meso-scale structure of polarization domains that ultimately lowers the average lattice symmetry at the atomic scale, producing an anisotropic chiral stress field that induces the detectable orthorhombic distortion deep in the tetragonal phase, a remarkably strong microscopic-macroscopic correlation that binds X-ray data to dielectric spectroscopy data.

Part II

Nonlinear waves in
nanodisordered Ferroelectric
Perovskites

Beam propagation in photorefractive media

Ferroelectric KLTN crystal is also a fundamental material to study the physics of nonlinear waves. In this Chapter, we introduce the basic physical concepts on which rely part of the phenomena investigated in the following chapters. In particular, the general concept of nonlinear wave is briefly introduced and applied in detail to optical spatial propagation in photorefractive media. First, we will focus on the photorefractive effect, a nonlinear optical mechanism due to the local self-modulation of the refraction index. Then, we highlight the role of the paraxial Helmholtz equation in describing propagation and including a nonlinearity, we obtain the nonlinear Schrödinger equation. Finally, we introduce some of the main nonlinear phenomena: solitons and rogue waves.

7.1

Introduction

Generally, the dynamics of a system near a stationary configuration is studied expanding the relevant physical quantities around the equilibrium point. The dynamics is thus modelled by linear differential equations, from which emerges the fundamental physical concept of normal mode as a tool to describe the dynamics. The linearity of the problem allows to express any solution as a superposition of its normal modes. Exciting the system through a localized perturbation, the system will evolve broadening its structure, since a specific eigenvalue or phase velocity characterizes each mode. In optics this leads to the typical phenomena of diffraction and dispersion, characteristic of any continuous system, linearly approximated. Conversely, when the interactions in the system are such that the energy and momentum exchanged are comparable to the energy that binds it to equilibrium, the system evolution cannot be described in terms of oscillations around an equilibrium point, and nonlinear

phenomenology emerges. Different modes can be made to interact and nonlinearity can transfer energy and momentum from one mode to the other. In the case of nonlinear optics, for example, we have the effect of second-harmonic-generation, or more generally, the interaction between waves at different frequencies [85]. However, when the anharmonic response is so strong, the concept of mode no longer applies. The strong correlations make the system respond collectively, and its behaviour, to be described, requires the introduction of new, qualitatively different constituent objects without an analogue in a linear theory. Solitons are the most important ones. Optical solitons are highly-localized electromagnetic perturbations that propagate in the supporting medium without spreading their spatial or temporal structure [182]. In fact, nonlinear interaction exactly balances the dispersive character of the pulse. They emerges as the optical intensity is able to change the index of refraction spatial distribution of the medium, the so-called Kerr effect, governed in centrosymmetric media by the susceptibility tensor $\chi^{(3)}$ [85]. In what follows, the picture will be described for waves interacting through a saturable nonlinearity, as the one occurring in photorefractive media.

7.2

Photorefractive effect

The photorefractive effect is the self-local modulation of the refractive index of a medium induced by an optical field proportional to the light intensity [183]. In particular, a process occurring in materials manifesting both photoconductivity and electro-optic response [184, 185]. In these media interaction with optical radiation leads to local charge separation, with the corresponding generation of a space-charge field that modulates the index of refraction via an electro-optic effect induced by the electromagnetic field. It is common in ferroelectrics with deep in-band donor/acceptor impurities. Impurities energy levels must be sufficiently far in energy from the valence and conduction bands so ionization is not dominant. The nanodisordered ferroelectric perovskite samples described extensively in the previous Chapters, support photorefractive effect through Copper and Vanadium impurities. In the next paragraph, we briefly introduce the model that is commonly adopted to describe the photorefractive effect.

7.2.1

Band-transport model

The basic phenomenology is reported in Fig. 7.1. We consider a dielectric medium with in-band deep acceptors and photosensitive donor impurities, their density are respectively N_a and N_d and typically $N_d \gg N_a$. When light propagates inside the crystal with a non-uniform intensity distribution $I(\mathbf{r})$, the charge carriers of the donor sites in the bright areas are excited and, then, they drift and/or diffuse till they recombine in the acceptor sites in the dark area. The result is a spatial charge

field that depends on the light pattern [184]. The standard model of photorefraction is based on semiclassical nonlinear rate equations and assumes a constant number of impurities [186].

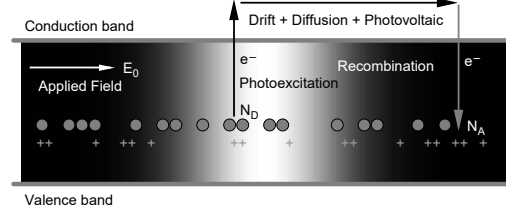


Figure 7.1. Scheme of the band structure of a typical photorefractive material and sketch of the charge carriers separation (recombination) in the illuminated (dark) zone of the crystal (From Ref. [184]).

$$\frac{\partial}{\partial t} N_d^+ = (\beta + sI(\vec{r}))(N_d - N_d^+) - \gamma N_e N_d^+, \quad (7.1)$$

where N_d^+ is the ionized donor density, N_e is the free electron concentration, β is the thermal ionization coefficient, s is the photo-ionization coefficient related to the absorption cross-section and γ electron-donor recombination constant according to Langevin theory [184]. Under the hypothesis that the average carrier motion occurs on temporal scales much larger than the ones related to the electron free path, drift and diffusion processes gives the macroscopic electric current density

$$\mathbf{J} = e\mu N_e \mathbf{E} + k_b T \mu \nabla N_e, \quad (7.2)$$

where e is the electronic charge, μ is the carrier mobility, $k_b T$ is the thermal energy and $\mathbf{E} = \mathbf{E}(r, t)$ the quasi-static electric field distribution. The second term in Eq. (7.2) represents the diffusive current according with the Einstein relation $D = (\mu k_b T) / e$. The above relations are connected through the continuity equation

$$\frac{\partial}{\partial t} \rho + \nabla \cdot \mathbf{J} = 0, \quad (7.3)$$

with the average charge density distribution $\rho = e(N_d^+ - N_a - N_e)$. Finally, the electric field satisfies the Maxwell equations

$$\begin{cases} \nabla \cdot (\varepsilon \mathbf{E}) = \rho \\ \nabla \times \mathbf{E} = 0. \end{cases} \quad (7.4)$$

The solution for the above set of nonlinear equations gives the field \mathbf{E} that rules the nonlinearity acting on the optical beam. However, the system is not analytically solvable and a several approximations are needed. We address the issue in the next section through the space-charge field approach [187, 188].

7.2.2

Self-induced space-charge field

We start considering that two time scales intervene: the charge recombination time τ_r , which takes into account local excitation events and the dielectric relaxation time τ_d , related to the macroscopic dielectric response, that is the average time needed to screen an arbitrary electric field distribution inside the material. Generally, $\tau_r \ll \tau_d$, so that the microscopic process can be considered at equilibrium with $\frac{\partial N_d^+}{\partial t} = 0$ [188]. This statement, with also the consideration based on the typical experimental conditions of low intensity regime, in which $N_e \ll N_a$ and $\alpha \equiv (N_d - N_a)/N_a \gg 1$, allows us to manage Eq. (7.1) and ρ to get:

$$N_e = \frac{(\beta + sI)}{\gamma} \left[\frac{N_d - p/e}{p/e + N_a} \right], \quad (7.5)$$

and, substituting this to (7.3), we obtain

$$\begin{aligned} \nabla \left[\frac{\gamma}{e\mu s\alpha} \frac{\partial(\underline{\varepsilon}(0)\mathbf{E})}{\partial t} + \mathbf{E}(\beta/s + I) \frac{1 - \frac{\nabla \cdot (\underline{\varepsilon}(0)\mathbf{E})}{\alpha N_a e}}{1 + \frac{\nabla \cdot (\underline{\varepsilon}(0)\mathbf{E})}{N_a e}} + \right. \\ \left. + \frac{k_B T}{e} \nabla \cdot \left((\beta/s + I) \frac{1 - \frac{\nabla \cdot (\underline{\varepsilon}(0)\mathbf{E})}{\alpha N_a e}}{1 + \frac{\nabla \cdot (\underline{\varepsilon}(0)\mathbf{E})}{N_a e}} \right) \right] = 0, \end{aligned} \quad (7.6)$$

where we use $\underline{\varepsilon}(0)$ to underline that the dielectric response is quasi-static for the considered time scales. We can define the dark intensity $I_d \equiv \beta/s$, which represents the light-independent thermal contribution to the charge ionization. I_d is part of the more general background illumination I_b that takes into account all the secondary intensities that intervene during the process. Since $\alpha \gg 1$, the first term in Eq. (7.6) is negligible, so that in the quasi-stationary case ($\partial \mathbf{E}/\partial t \approx 0$), Eq. (7.6) reduces to

$$\mathbf{E}(I_b + I) \frac{1}{1 + \frac{\nabla \cdot (\underline{\varepsilon}\mathbf{E})}{eN_a}} + \frac{k_b T}{e} \nabla \cdot \left((I_b + I) \frac{1}{1 + \frac{\nabla \cdot (\underline{\varepsilon}\mathbf{E})}{eN_a}} \right) = g, \quad (7.7)$$

where g is a boundary-condition-dependent constant. For instance, the unbiased case, $V = 0$ implies $g = 0$ and the the diffusive electric field reduces to $\mathbf{E} = -\frac{k_b T}{e} \frac{\nabla I}{I_b + I}$. A more complex picture arises if $g \neq 0$ which means that there is an external bias electric field $E_0 \neq 0$. We start the perturbative treatment for one-dimensional waves (1+1D), introducing the following dimensionless quantities:

$$Y \equiv \frac{|\mathbf{E}|}{E_0} \quad Q \equiv \frac{I_b + I}{I_b} \quad \xi \equiv \frac{x}{x_q} = x \frac{eN_a}{\varepsilon E_0}, \quad (7.8)$$

where x_q is the saturation length. Typically the illuminated region of the crystal l is much smaller than the whole crystal length $L \gg l$, consequently $E_0 \simeq V/L$. Through these variables, Eq. (7.7) can be rewritten as

$$\frac{YQ}{1 + Y'} + a \left[\frac{Q'}{1 + Y'} - \frac{Q}{(1 + Y')^2} Y'' \right] = G, \quad (7.9)$$

with $a = N_a k_b T / \varepsilon E_0^2$ e $G = g / E_0 I_b$ and where the symbol ' indicates $d/d\xi$.

Explicating the equation (7.9):

$$Y = \frac{G}{Q} - a \frac{Q'}{Q} + \frac{GY'}{Q} + a \frac{Y''}{1 + Y'}. \quad (7.10)$$

The first term indicates the local contributions whereas terms with the derivative takes into account the nonlocal contributions. Assuming $l \gg x_q$, the nonlocal effects play a minor role and we can follow a perturbative approach. Since the derivatives scale with $\eta = x_q/l \sim 0.01$ whereas a is typically of the order of units [188] we can expand in orders of η . At the zero-th order we have

$$Y^{(0)} = \frac{G}{Q} + o(\eta), \quad (7.11)$$

and, iterating, we obtain the first order

$$Y^{(1)} = \frac{G}{Q} - a \frac{Q'}{Q} - \frac{Q'}{Q} \left(\frac{G}{Q} \right)^2 + o(\eta^2). \quad (7.12)$$

The first term, which is dominant in biased conditions, gives the so-called Kerr-saturated or screening nonlinearity and governs the soliton formation. It is a local term since the field in a given position depends only from the optical intensity in that position. Since the charges rearrange to screen the external field, typically $G \simeq -1$, and this term makes $|\mathbf{E}| < E_0$. The second term is the diffusion field whereas the third emerges from the coupling between the diffusion field and the screening field: both are nonlocal terms and they give rise to asymmetrical contributions to the space-charge field that can distort beam propagation, as for example the soliton bending [189].

7.3

Electro-optic effect in photorefractive crystals

In the previous section, we derived the space-charge field \vec{E} which leads to a modulation of the index of refraction through the electro-optic effect. However, in order to have significant variations of Δn , a large electro-optic response of the material is required. It can be obtained in non-centrosymmetric phases, such as in poled ferroelectrics, and in centrosymmetric paraelectric phases in proximity of the ferroelectric phase transition. The electro-optic response emerges from the coupling between a low-frequency electric field, in our case the quasi-static photorefractive \mathbf{E} , and high-frequency electromagnetic field \mathbf{E}_{opt} , i.e. the light beam. The physical mechanism of the coupling can be explained assuming that the material reacts to the presence of \mathbf{E} changing locally its dielectric properties. This means a variation of the high-frequency polarization that affects also the propagation of \mathbf{E}_{opt} . To describe the electro-optic effect, we consider the tensor $\varepsilon = \varepsilon_0 n^2$ or the strictly correlated tensor $1/n^2$ [188]. We define $(1/n^2) = (1/n^2)|_{\mathbf{E}=0} + \Delta \left(\frac{1}{n^2} \right)$. The tensor variation $\Delta \left(\frac{1}{n^2} \right)$

is therefore caused by the low-frequency \mathbf{E} via the nonlinear components of the susceptibility of the medium, i.e., its polarization and electric displacement vector. We note that $\Delta\left(\frac{1}{n^2}\right)$ can be considered a local variation, if it is compared to the spatial and temporal nonlocality of the charge migration [188]. The E -dependence of $\Delta\left(\frac{1}{n^2}\right)$ can be summarized by the following tensorial expression:

$$\Delta\left(\frac{1}{n^2}\right)_{ij} = r_{ijk}E_k + s_{ijkl}E_kE_l, \quad (7.13)$$

with r_{ijk} and s_{ijkl} , respectively, the linear and quadratic electro-optic coefficients. In this section we focus our attention on the case in which the linear term in Eq. (7.13) vanishes, i.e., we deal with centrosymmetric media. The quadratic electro-optic effect can be observed only in crystals having a dielectric constant ε that strongly depends on the actual temperature. In this situation, it is more appropriate to consider polarization \vec{P} instead of \vec{E} . We can rewrite Eq. (7.13) as:

$$\Delta\left(\frac{1}{n^2}\right)_{ij} = g_{ijkl}P_kP_l, \quad (7.14)$$

with g_{ijkl} the element of the electro-optic tensor referred to \vec{P} . We point out that g_{ijkl} is temperature independent since all the dependence in temperature is enclosed in ε . From (7.14) we get the second order variation of the refractive index $\Delta n(E)$

$$\Delta n(E) = -\frac{1}{2}n_0^3g_{eff}\varepsilon_0^2(\varepsilon_r - 1)^2 E^2 \quad (7.15)$$

where we have introduced g_{eff} , that is the effective electro-optic parameter. Through the photorefractive effect, we have found the expression for $|\mathbf{E}|$ (Eq. (7.11)) and substituting it in (7.15), we obtain we the canonical Kerr-saturated nonlinearity:

$$\Delta n(I) = -\Delta n_0 \frac{1}{(1 + I/I_b)^2} \quad (7.16)$$

with $\Delta n_0 = (1/2)n_0^3g_{eff}\varepsilon_0^2(\varepsilon_r - 1)^2 E_0^2$. The type of nonlinearity is governed by the sign of g_{eff} , and may have a focusing or defocusing effect on the propagating beam for $g_{eff} > 0$ and $g_{eff} < 0$, respectively. The fact that the intensity appears only through the ratio I/I_b relies in the cumulative response and is the basis for the low powers needed for nonlinear optics in photorefractive media.

7.3.1

Cumulative nature of photorefractive response

Under quite general assumptions, typical of most experimental conditions, and in the accessible 1+1D case, that is, when the optical field depends only on one transverse axis (say the x axis), the photo-excitation/migration/recombination mechanism reaches a steady-state for an electric field that is well approximated by

$$E(x) = \frac{E_0}{1 + \frac{I(x)}{I_d}}, \quad (7.17)$$

where I is the optical intensity and I_d is the dark illumination. The dark illumination is the intensity equivalent to the low residual thermal conductivity in the absence of the optical field. It can be artificially increased illuminating the sample with a second plane-wave optical field, the so-called background illumination. This model is termed the steady-state screening model for photorefractive solitons. For a linear electro-optic response, that is, in conditions in which $\Delta n(E) \propto E$, this leads to the saturated response $\Delta n = -\Delta n_0(1 + I/I_s)^{-1}$, with $I_s \equiv I_d$ while, for a quadratic electro-optic response with $\Delta n(E) \propto E^2$, to the saturated Kerr response $\Delta n = -\Delta n_0(1 + I/I_s)^{-2}$. At steady-state, the small fraction of light absorbed by the donor impurities promotes to the conduction band the same number of electrons per unit of time that recombine throughout the sample, while on consequence of the space-charge field, diffusion, and external bias, the net charge migration per unit time in all regions is zero. This steady-state is reached only after a transient regime in which the space-charge is built-up in time, or accumulated, ultimately to form the steady-state distribution. In this transient, nonlinear response is accumulated, the crystal passing from being a homogeneous system to one with a growing Δn . The build-up process, in conditions in which the crystal is subject to a constant external bias and is illuminated by a constant optical field, involves a complex temporally nonlocal optical response [190]. A good approximation to the transient can be achieved on time scales larger than the electron-recombination time, i.e., in conditions in which the excitation-recombination process has reached locally an equilibrium. Here the transient is governed by the charge relaxation process associated to charge conservation, $\partial_t \rho + \nabla \cdot \mathbf{J} = 0$, where ρ and \mathbf{J} are respectively the charge and current densities. The build-up then obeys

$$t_d \frac{\partial E}{\partial t} + \left(1 + \frac{I}{I_d}\right) E = E_0, \quad (7.18)$$

where t_d is the dielectric relaxation time. The model can be further simplified by considering situations of weak diffraction, that is, conditions in which the build-up is essentially constant along the propagation axis [188], so that

$$E = E_0 e^{-\left(1 + \frac{I}{I_d}\right) \frac{t}{t_d}}. \quad (7.19)$$

For a quadratic electro-optic response, the resulting nonlinearity is

$$\Delta n = -\Delta n_0 e^{-\left(1 + \frac{I}{I_d}\right) \frac{2t}{t_d}} \simeq -\Delta n_0 e^{-\frac{2It}{I_d t_d}} \equiv -\Delta n_0 e^{-\frac{I}{I_s(t)}} \quad (7.20)$$

as $I \gg I_d$ in the regions of interest for the propagation and having defined $I_s(t) \equiv I_d t_d / 2t$.

7.4

Nonlinear wave equation

To understand nonlinear waves dynamics, we show how an index variation induced by photorefraction (Eq. (7.16)) modifies beam propagation. Consider a monochromatic electromagnetic wave $\mathbf{E}_{opt}(\mathbf{r}, t) = \mathbf{E}_\omega(\mathbf{r})e^{i\omega t} + c.c.$, with frequency $\omega = \frac{2\pi c}{\lambda}$. From Maxwell equations, its propagation in an homogeneous media on scales of the order of λ , follows the scalar Helmholtz equation [75]

$$\nabla^2 \mathbf{E}_\omega + k_0^2 n^2(\mathbf{r}) \mathbf{E}_\omega = 0, \quad (7.21)$$

where $k_0 = \omega/c$ and $n(\mathbf{r}) = n_0 + \Delta n(\mathbf{r})$, expressed as a small perturbation to the linear index of refraction, which depends on the spatial coordinates via the electro-optic effect.

In our experiments the longitudinal size of the beam l_z is much larger than its transverse size l_{xy} , typically $l_z \sim 1 \div 3$ m and $l_{xy} \sim 10 \div 1000$ μm , thus the beam is spatially localized in the transverse plane. In these conditions, the paraxial approximation holds, and for a propagation along the z-direction, the field can be expressed as $\mathbf{E}_\omega(\mathbf{r}) = \mathbf{A}_\omega(\mathbf{r}_\perp, z)e^{-ik(\omega)z}$, with $k(\omega) = k_0 n(\omega) = \frac{\omega}{c} n(\omega)$. Under the Slowly Varying Envelope Approximation, that implies $\partial_{zz} A(\omega) \approx 0$, from (7.21) we thus obtain the paraxial Helmholtz equation:

$$\frac{\partial \mathbf{A}_\omega}{\partial z} + \frac{i}{2k} \nabla_\perp^2 \mathbf{A}_\omega = -ik \frac{\Delta n(\vec{r})}{n_0} \mathbf{A}_\omega. \quad (7.22)$$

This equation is known as generalized Nonlinear Schrödinger Equation (GNLSE) and describes paraxial nonlinear wave propagation in the spatial domain. Formally it is similar to the Schrödinger Equation, where the longitudinal length variable z plays the role of time and the nonlinear term plays the role of an effective potential for the light beam. The second term describes diffraction, i.e. the beam spreading, and can be exactly balanced for specific values of the nonlinearity depending on the external parameters. This compensation leads to an amplitude solution \mathbf{A}_ω spatially-localized and stationary: a spatial soliton. In particular, with a nonlinearity given by Eq. (7.16), we obtain photorefractive screening solitons.

Photorefractive soliton

Solitons, in general, are localized waves that do not spread in time or space. They are ubiquitous in nature and can be found in several systems such as optical fibers [191, 192], semiconductor microcavities [193], Bose-Einstein condensates [194], water [195], crystals [18] and lattices [9]. From a mathematical point of view, spatial solitons emerge when the diffraction is exactly compensated by the nonlinearity so that the beam is shape-invariant along propagation, namely the z axis. The solution is analytic for pure Kerr nonlinearity and for (1+1D) soliton, that is a soliton with only one transverse dimension, i.e. x -axis, that propagates along another dimension, i.e. z -axis. The soliton, to preserve the shape of the beam during propagation, needs that the z -dependent factor is confined only in a phase factor. We, therefore, look for solutions of the form

$$A(x, z) = u(x)e^{i\Gamma z} \sqrt{I_b + I_d} \quad (7.23)$$

with Γ the solitonic propagation constant and, as discussed above, $I_d \ll I_b$. We renormalize the spatial coordinate x according to the following definitions

$$\xi \equiv \frac{x}{d} \quad d \equiv (\pm 2kb)^{-1/2} \quad b \equiv \frac{k}{n} \left[\frac{1}{2} n^3 g_{eff} \varepsilon_0^2 (\varepsilon_r - 1)^2 l \left(\frac{V}{L} \right)^2 \right]. \quad (7.24)$$

Considering the focusing case ($g_{eff} > 0$), we obtain the dimensionless equation for centrosymmetric bright screening (1+1)D soliton [8]:

$$\frac{d^2 u(\xi)}{d\xi^2} = - \left[\frac{1}{1 + u_0^2} - \frac{1}{(1 + u(\xi)^2)^2} \right] u(\xi) \quad (7.25)$$

where d is called nonlinear length and $u(\xi)$ is the soliton amplitude $u(x)$ normalized to the square root of the sum of background and dark irradiances. In the $u_0 \ll 1$ limit, the pure Kerr model is recovered, which is integrable, and the solution takes the shape of a hyperbolic secant [196, 197]. This means that for an input gaussian beam some intensity is radiated away to get the right secant-profile [198]. This solution represents an attractor to the system dynamics and it is stable to perturbations [199]. The main beam parameters that characterize the soliton solution are the normalized width $\Delta\xi$ (associated to the FWHM of the input beam) and the normalized intensity u_0 ; the relation between these two is unique [199]. The full problem can be solved integrating numerically Eq. (7.25) and the solution remains a bell-shaped function but it is neither a Gaussian nor a hyperbolic secant [199]. In this case the relation between $\Delta\xi$ and u_0 is no longer fixed but it is summarized by the so-called existence curve (an example of this is reported in Fig. 7.2).

In the simplified 1+1D model, the low-frequency photoinduced electric field E depends only on the transverse x -axis along which the bias field is applied. In a more

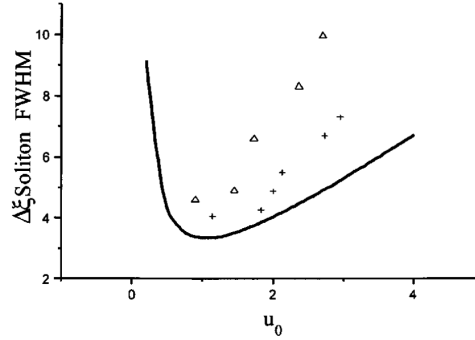


Figure 7.2. Soliton existence curve for photorefractive spatial solitons. The solid line is a theoretical prediction whereas the dots are experimental points. (From Ref. [8]).

general situation, as occurs for optical beams that are confined in two transverse directions in the (x, y) plane, the situation is more involved since the external field is delivered by two x -directed plane electrodes while the photoinduced electric field \mathbf{E} , obeying the quasi-static irrotational condition $\nabla \times \mathbf{E} \simeq 0$, will also have a y -directed component [188]. In typical experimental conditions, a prevalently x -directed field $\mathbf{E} \simeq E\mathbf{u}_x$ emerges in a manner analogous to what occurs when a dielectric cylinder (the illuminated region) is placed in a uniform electric field. As for the polarization charge in the dielectric, here the space-charge forms two lateral lobes along the x -axis. The lobes break the rotational symmetry of the nonlinearity. The lobes, that have been subject of intense debate and study, play a dominant role when diffraction is strong. In the weakly diffracting case, as the one investigated in this Thesis, they affect the finer details of the nonlinear dynamics. The anisotropy seems to theoretically allow, at least, only (2+1D) elliptic soliton and to prohibit the existence of perfectly cylindrical one [200]. In truth, circular soliton are also possible, where the key is the lobes suppression that occurs for enough small transverse dimension Δx and Δy [200]. In turn, we have to note that the two-dimensional soliton is unstable for pure Kerr nonlinearity but it is stable for the saturable nonlinearity as our photorefractive one [182]. One of the things that is connected to our present study of photorefractive solitons, is the identification of the origin of the so-called soliton rogue waves. In order to address this issue, we provide in the next section a brief introduction of rogue waves.

Brief introduction of rogue waves

Rogue waves are extreme events that can affect several wave-sustaining systems [201]. In particular, our attention is focused on spatial rogue waves that emerge in a photorefractive crystal due to the very strong cumulative nonlinearity. The first observations of rogue waves were done in ocean [202]. Since they represent a real danger for vessels, many efforts have been exercised to understand the phenomenon but with little success due to the intrinsic difficulty of observing in nature such rare events [21]. The need of available controllable experimental conditions has driven the search for rogue waves in different systems. In fact, despite they come from different mechanisms, all extreme events respond to an universal statistics and they fulfil the NLSE. The aim is to exploit more affordable systems as test benches for their ocean counterpart and, of these, a very suitable choice are ferroelectric crystals in proximity of the phase-transition due to their large photorefractive nonlinearity and their intrinsic random distribution of ferroelectric domains of different size and orientation [26]. The key signature of the extreme events is the presence of long-tail statistics, which indicates, for spatial experiments, the existence of high intensity peaks in the transverse profile. To clarify this point, we introduce the intensity distribution function, e.g. extrapolating the peak intensities over more than one thousand images. For a gaussian distribution we expect a decay following the function $P(I) = \exp(-I/\bar{I})/\bar{I}$ [203]. Large deviation from gaussian behavior means that the intensity distribution is described by a stretched exponential $P(I) = \exp(-cI^b - a)$ with $b < 1$ that indicates the presence of long tail statistics. Furthermore, to recognize a rogue wave, the hydrodynamic criterion is also commonly adopted, that is an extreme event is identified if its intensity exceed at least by a factor of two the mean amplitude of the highest one-third of the detected waves [204]. Both of these criteria are well satisfied by photorefractive ferroelectric crystals close to the Curie point. It is relevant, that the rogue phenomena disappear for crystals far above the phase transition, demonstrating the relevant role of nonlinearity in extreme events formation [21].

Using Bessel Beams to Induce Optical Waveguides

An interesting aspect of our study is connected to possible applications. Programmable waveguides scalable into highly integrated photonic circuits are key ingredients to the development of innovative optical technology in various rapidly growing fields, including linear quantum computation and optical information processing [205]. While present achievements are based on planar photonic circuits [206–208], optical networks can in principle operate in a fully three-dimensional volume, thus increasing the achievable number of interlinked gates and devices. Operating in a volume requires specific fabrication tools, such as direct optical writing [209–214]. At present, direct writing involves a step-by-step fabrication that becomes increasingly cumbersome as design complexity grows. Furthermore, as the details of the circuitry are scaled down to the optical wavelength, diffraction in the writing beams limits the available volume, ultimately compromising scalability. Previous studies have attempted to overcome diffractive distortion in optical writing through nonlinear beam propagation, as occurs in self-writing and spatial solitons [215–219]. This, however, causes optical writing to be dominated by light-light interaction, greatly complicating circuit design [220–223]. At present no scalable optical writing technique based solely on linear waves has been demonstrated in a full macroscopic volume. In what follows we demonstrate a scalable method to optically induce waveguides deep in a volume using Bessel beams. The method is used to fabricate waveguides in increasingly complex geometries, integrated multi-port splitters and miniaturized functional electro-optic gates.

8.1

Bessel Beam

In this section we briefly introduce one of the most significant non-diffractive solutions of the paraxial Helmholtz equation, i.e., Bessel beam. In particular, we limit our analysis to the linear part of Eq. (7.22), discarding all the nonlinear contributions, obtaining the linear paraxial Helmholtz equation

$$\frac{\partial \vec{A}_\omega}{\partial z} + \frac{i}{2k} \nabla_\perp^2 \vec{A}_\omega = 0. \quad (8.1)$$

Solutions of (8.1) are also plane waves, which have the property of being non-diffractive. Indeed, non-diffracting beams are volume interference patterns of plane waves and inherited their proprieties [10]. For example, these patterns exhibit self-healing, i.e. they reform after an obstacle, since their parent plane waves permeate all space. The Bessel Beam (BB), which belong to the category of non-diffractive beams, is an interference pattern that forms from the coherent superposition of plane waves at a fixed angle with the propagation axis [10, 224]. The conical distribution of wave vectors implies that each plane-wave component has the same phase velocity along the propagation axis, say, the z axis, so that no mutual phase slippage between components intervenes. The result is a localized central peak along z that does not diffract. Its equation is [225]

$$E(r, \phi, z) = A_0 \exp(ik_z z) J_n(k_r r) \exp(\pm in\phi), \quad (8.2)$$

with A_0 the amplitude, n is the order of the Bessel function J and ϕ is the azimuthal component.

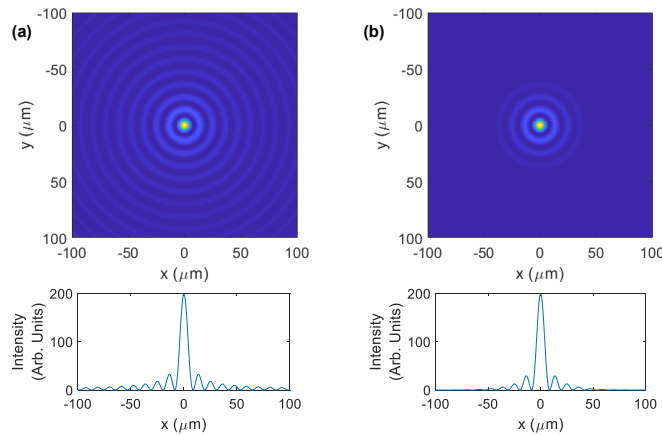


Figure 8.1. Numerical simulation of the transverse intensity of (a) Bessel and (b) Bessel-Gauss beam.

This peak, however, is accompanied by an elaborate and extended oscillating tail structure that actually contains most of the beam power [224, 226], as reported in Fig. 8.1 (a). A consequence of this is that BB are not physically achievable because they carry infinite energy. A realization consists in considering a BB with a gaussian envelope. These new solutions, the so called Bessel-Gauss beam, maintain the properties of BB but only for finite distances suitable for experiments [227, 228]. To achieve the Bessel-Gauss equation we consider Eq. (8.2) and a gaussian envelope $\exp(-x^2/\sigma^2)$. Here we report the simplest case for $z = 0$ (the complete formula is provided in Ref. [228]):

$$E(r, z = 0) = A_0 J_n(k_r r) \exp(-r^2/\sigma^2) \quad (8.3)$$

with σ^2 the variance of the gaussian curve and smaller the σ , less the number of the Bessel rings, as shown in Fig. 8.1 (b).

8.2

Guiding in a Bessel Index of refraction pattern

We thus begin by addressing the basic question of if and how an index pattern that reproduces the intensity distribution of a BB, in its finite energy Bessel Gauss realization [228], can actually guide light along the z axis. Consider, for paraxial propagation, the inhomogeneous parabolic equation

$$\partial_z A - \frac{i}{2k} \nabla_{\perp}^2 A = \frac{ik}{n_0} \Delta n(I) A \quad (8.4)$$

where z is the propagation axis, (x, y) is the transverse plane, $\nabla_{\perp}^2 \equiv \partial_{xx}^2 + \partial_{yy}^2$, A is the slowly varying component of the optical field $E_{opt} = A(r_{\perp}, z) \exp(-ikz)$, $k = k_0 n_0$, n_0 is the unperturbed refractive index, and $k_0 = 2\pi/\lambda$, with λ the wavelength. The index of refraction is $n = n_0 + \Delta n$, with $\Delta n = \Delta n_0 |J_0(k_r r) \exp[-(r/\sigma)^2]|^2$, where J_0 is the zeroth-order Bessel function, $r = \sqrt{x^2 + y^2}$ the distance in the transverse (x, y) plane, and k_r and σ are fixed parameters (see the Bessel beam pattern in Figs. 8.2 (a), (b)). As demonstrated in Figs. 8.2 (c)-(f) through a numerical simulation of Eq. (8.4), the z -independent BB pattern will guide a naturally diffracting Gaussian beam focused on its input plane (i.e., $A(r, z = 0) = A_0 \exp[-(r/\sigma_G)^2]$) for a specific value of Δn_0 .

8.3

Waveguiding mechanism

8.3.1

Theory

We optically induce the BB pattern in a photorefractive crystal. Writing is carried out using a Bessel-Gauss beam with $A_w = A_{w0}J_0(k_r r) \exp[-(r/\sigma)^2]$, with k_r and σ chosen so that Rayleigh length $z_R = \pi n \sigma^2 / \lambda \gg L_z$ and the diffraction-free distance $z_D = \sigma / (k_r / k) \gg L_z$ [224], where L_z is the length of the sample along the propagation axis [228]. The photoexcitation of deep in-band impurities and charge transport leads to the formation of an optically-induced space-charge field $E_{sc}(I_w, t)$ given by [188]

$$E_{sc}(I_w, t) = E_{0w} \left(e^{-\left(1 + \frac{I_w}{I_d}\right) \frac{t}{t_d}} - 1 \right). \quad (8.5)$$

Here $I_w = |A_w|^2$ is the writing intensity distribution, t is the duration of writing process, I_d and t_d are constants, the dark-illumination (that can be changed by also illuminating the sample with a plane wave) and the dielectric relaxation time, respectively [188]. $E_0 = E_{0w}$ is, in turn, the constant external bias field applied to the sample along one transverse axis, say the x axis, during the writing phase. The electric field $E = E_{0w} + E_{sc}$ now changes locally the sample index of refraction through the electro-optic effect. Since the sample is heated above its room-temperature Curie point T_C , in the paraelectric phase, it manifests a quadratic electro-optic effect according to which $\Delta n = -(1/2)n_0^3 g_{eff} \epsilon_0^2 (\epsilon_r(T) - 1)^2 E^2 \equiv -\Delta n_{0,T} (E/E_0)^2$. Here, g_{eff} is the effective electro-optic coefficient, ϵ_0 is the vacuum dielectric constant, $\epsilon_r(T)$ is the low-frequency sample relative dielectric constant at the writing temperature T , and $\Delta n_{0,T} \equiv (1/2)n_0^3 g_{eff} \epsilon_0^2 (\epsilon_r(T) - 1)^2 E_0^2$ is the characteristic scale of the response for the given temperature and bias field E_0 . The presence of the dielectric anomaly at $T = T_C$ implies that the dielectric constant in the paraelectric phase is strongly temperature dependent, following the Curie-Weiss law $\epsilon_r(T) = C/(T - T_C)$ [187].

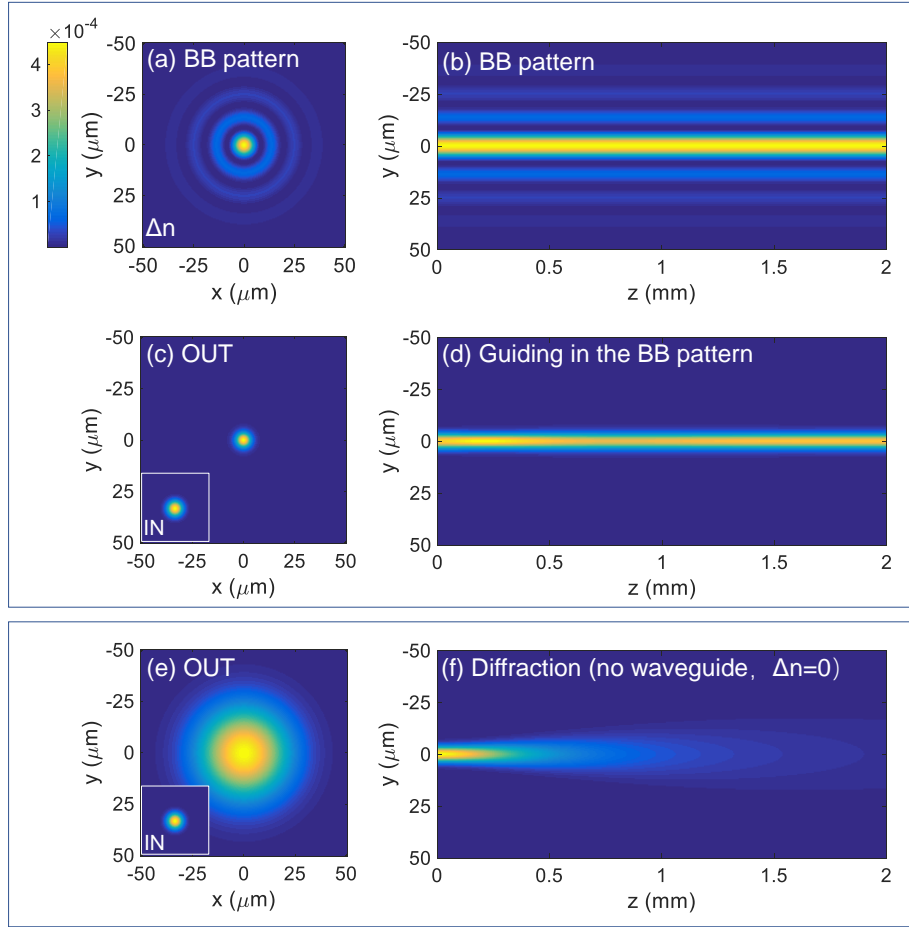


Figure 8.2. A Bessel beam waveguide. (a) $\Delta n(x, y, z = 0)$ and (b) $\Delta n(x = 0, y, z)$ distributions for $\Delta n = \Delta n_0 |J_0(k_r r) \exp[-(r/\sigma)^2]|^2$ (BB pattern). Input and output intensity distribution (c) and propagation dynamics (d) of a Gaussian beam focused on the $z = 0$ plane, i.e., $I(r, z = 0) = |A_0 \exp[-(r/\sigma_G)^2]|^2$, propagating through the pattern, as predicted through a beam-propagation-method simulation [229] for $\sigma = 60 \mu\text{m}$, $k_r = 0.28 \mu\text{m}^{-1}$, $\sigma_G = 5 \mu\text{m}$, $\lambda = 532 \text{ nm}$, and $n_0 = 2.3$. For $\Delta n_0 = 4.5 \times 10^{-4}$, the pattern is able to guide the beam that would otherwise diffract and spread for $\Delta n_0 = 0$ (e), (f).

Hence, heating the sample to a sufficiently high temperature $T_w > T_C$ causes the electro-optic response to drop and renders nonlinear beam effects and self-writing negligible [10, 230, 231]. The light-induced E_{sc} of Eq. (8.5) can now be used as a blue-print for the electro-optic activation of a waveguide. This is achieved by cooling the sample closer to the Curie point to T_g ($T_g < T_w$), leading to a strongly enhanced $\epsilon_r(T_g) > \epsilon_r(T_w)$, and applying an appropriate bias guiding electric field $E_0 = E_{0g}$. The resulting index pattern is

$$\Delta n(E_{0g}) = -(1/2)n_0^3 g_{eff} \epsilon_0^2 (\epsilon_r(T_g) - 1)^2 (E_{0g} + E_{sc})^2. \quad (8.6)$$

This index pattern can be used to guide and route an optical field A_g (Eq. (8.4))

with no further light-induced changes in E_{sc} . This can be achieved either using attenuated light ($I_g \equiv |A_g|^2 \ll I_w$), effectively halting the build-up process, or using longer wavelength light, for which the photoexcitation process becomes inefficient. For $E_{0g} = E_{0w}$ and for unsaturated conditions (i.e., $t \ll t_d$), Eqs. (8.5), (8.6) give $\Delta n \propto I_w$, reproducing the process analyzed in Fig. 8.2 (with $A_g(r, z = 0) = A_0 \exp[-(r/\sigma_G)^2]$). More generally, $E_{0g} \neq E_{0w}$ leads to a varied family of different guiding, routing, and antiguiding structures described by Eqs. (8.4), (8.6). This allows fast electro-optic control of the index of refraction pattern with no nonlinear propagation and without involving the slow charge migration processes required to alter the space-charge density [54, 232, 233].

8.3.2

Experiments

Experiments are carried out in a compositionally disordered photorefractive KLTN crystal (Potassium-Lithium-Tantalate-Niobate - $\text{K}_{0.95}\text{Li}_{0.05}\text{Ta}_{0.60}\text{Nb}_{0.40}\text{O}_3$) with the setup illustrated in Fig. 8.3 (a). The crystal was grown through the top-seeded solution method by extracting a zero-cut optical quality specimen that measures $L_x = 2.6$ mm, $L_y = 3.4$ mm, $L_z = 1.8$ mm along the x-y-z axes.

During fabrication of the waveguides, the sample is kept at $T_w = T_C + 20$ K above its ferroelectric Curie point at $T_C = 292$ K using a Peltier cell. The sample manifests a quadratic electro-optic effect with $n_0 = 2.3$, $g_{eff} = 0.14 \text{ m}^4\text{C}^{-2}$, and $\epsilon_r(T_w) \simeq 0.45 \times 10^4$. The bias field is obtained applying the voltage V_w to the x-facets, L_x apart, so that during this stage $E_{0w} = V_w/L_x = 1.7$ kV/cm. In these conditions, the characteristic scale of the electro-optic response is $\Delta n_0 \simeq 0.4 \times 10^{-4}$, appropriately low to not affect the propagation of the writing field A_w [234, 235]. There are numerous ways of generating a BB from a standard Gaussian laser beam [236, 237]. In our experiment, a continuous-wave $\lambda = 532$ nm frequency-doubled Nd:YAG laser is enlarged and made to propagate through a Spatial-Light-Modulator (SLM) that is programmed with an intensity mask that transmits a ring. Light is then focused by a lens onto the sample, forming the BB. The A_w is then an x-polarized zeroth-order Bessel-Gauss beam with $k_r = 0.16 \mu\text{m}^{-1}$ and $\sigma = 110 \mu\text{m}$ that is launched into the sample along the z axis. The input and output intensity distribution in the transverse x,y plane are imaged onto a CCD camera and reported in Figs. 8.3 (b) and (c), respectively. As expected, negligible diffractive distortion is observed for the $L_z = 1.8$ mm propagation through the sample. For a specific fabrication stage with a writing beam total input power of $1.1 \mu\text{W}$ and for an exposure time $t=360$ s, the waveguiding effect is reported in Figs. 8.3 (d)-(g). In the waveguiding stage, illustrated in Fig. 8.3 (d), $T_g = T_C + 6$ K leads to a higher $\epsilon_r(T_g) \simeq 1.5 \times 10^4$, so that for a waveguiding bias of $E_{0g} = V_g/L_x = 1.2$ kV/cm the characteristic amplitude of the index modulation $\Delta n_0 \simeq 2 \times 10^{-4}$ can now strongly affect diffraction. Figs. 8.3 (e)-(g) reports the waveguiding of an input focused 40 nW Gaussian beam (so that the ratio of the peak intensities is $I_g/I_w \simeq 0.07$) (Fig. 8.3 (e)) that is trapped to its input $12 \mu\text{m}$ Full-Width-at-Half-Maximum (FWHM) at the output (Fig. 8.3 (f)).

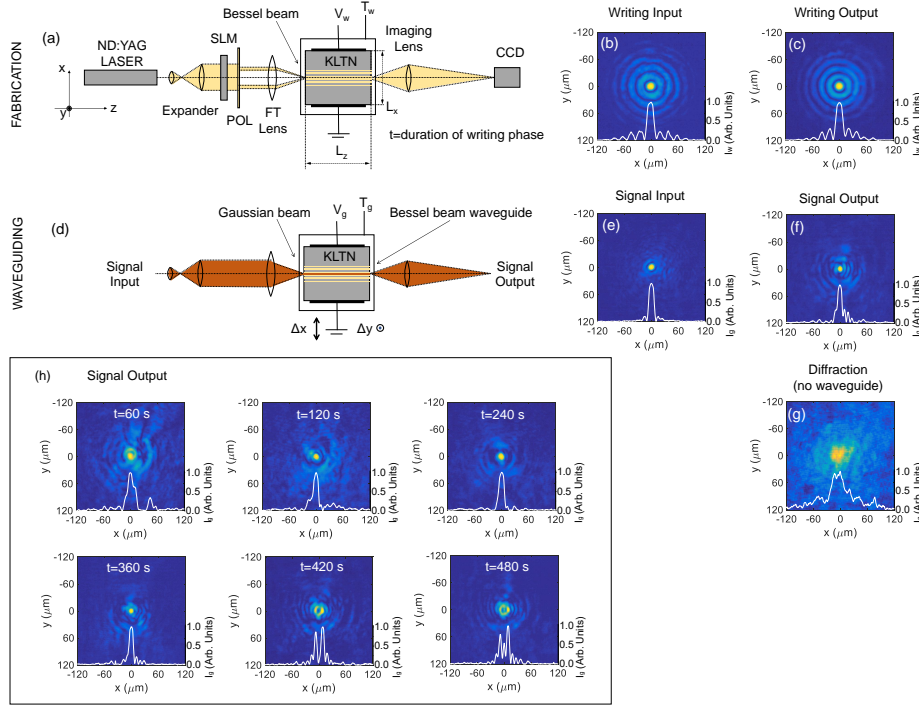


Figure 8.3. Demonstration of a BB waveguide in photorefractive KLTN. Fabrication : (a) scheme of the optical writing stage; (b) input and (c) output intensity distribution of the writing beam ($k_r = 0.16 \mu\text{m}^{-1}$ and $\sigma = 110 \mu\text{m}$). Waveguiding: (d) scheme of the optical guiding stage; (e) input and (f) output of a Gaussian guided beam (input FWHM = $12 \mu\text{m}$, $\sigma_G = 10 \mu\text{m}$) compared to (g) the diffracted output distribution with no waveguide (output FWHM = $39 \mu\text{m}$). Output intensity distribution (h) for different durations of the writing phase. Optimal guiding arises for $t = 240 - 360$ s (see panels $t = 240, 360$ s), while saturation introduces distortions for long exposure times (see panels $t = 420, 480$ s).

For comparison, in Fig. 8.3 (g), we report the same output intensity distribution if no fabrication stage is enacted and the BB waveguide is absent, where the beam spreads to an output FWHM of $39 \mu\text{m}$. As described in the model of (8.5) and (8.6), for a given I_w , the peak index modulation and shape of the light-induced waveguide also depends on the writing exposure time t , ultimately undergoing complete saturation for $t \gg t_d$. In our specific case of peak $I_w(0,0) \simeq 0.7 \text{ W/cm}^2$, the transverse output intensity distribution $I_g = |A_g(x, y, z = L_z)|^2$ for increasing values of t is reported in Fig. 8.3 (h). For $V_w = 450 \text{ V}$ and $V_g = 300 \text{ V}$, optimal guiding is achieved for $t = 240 - 360$ s. We note that each fabricated waveguide can be optically erased using a plane-wave illumination at T_w with an erasure time that is inversely proportional to the erasing intensity, allowing the optical reprogramming of the guiding structures. In our case, a BB waveguide will be completely erased by a low-intensity average 3 mW/cm^2 plane-wave illumination at T_w after 15 h.

8.3.3

Electro-optic control

In Fig. 8.4 we demonstrate the electro-optic control of a single BB waveguide. The output intensity distribution for a fixed T_g and a fixed A_g is found to strongly depend on V_g ($E_{0g} = V_g/L_x$), indicating that the guiding properties of the single waveguide can be activated through an external electric signal. For the present case of $V_w = 450$ V, peak $I_w(x, y, z = L_z)$, and $t = 360$ s, optimal waveguiding is achieved for $V_g = 300 - 500$ V (Figs. 8.4 (d)-(f)).

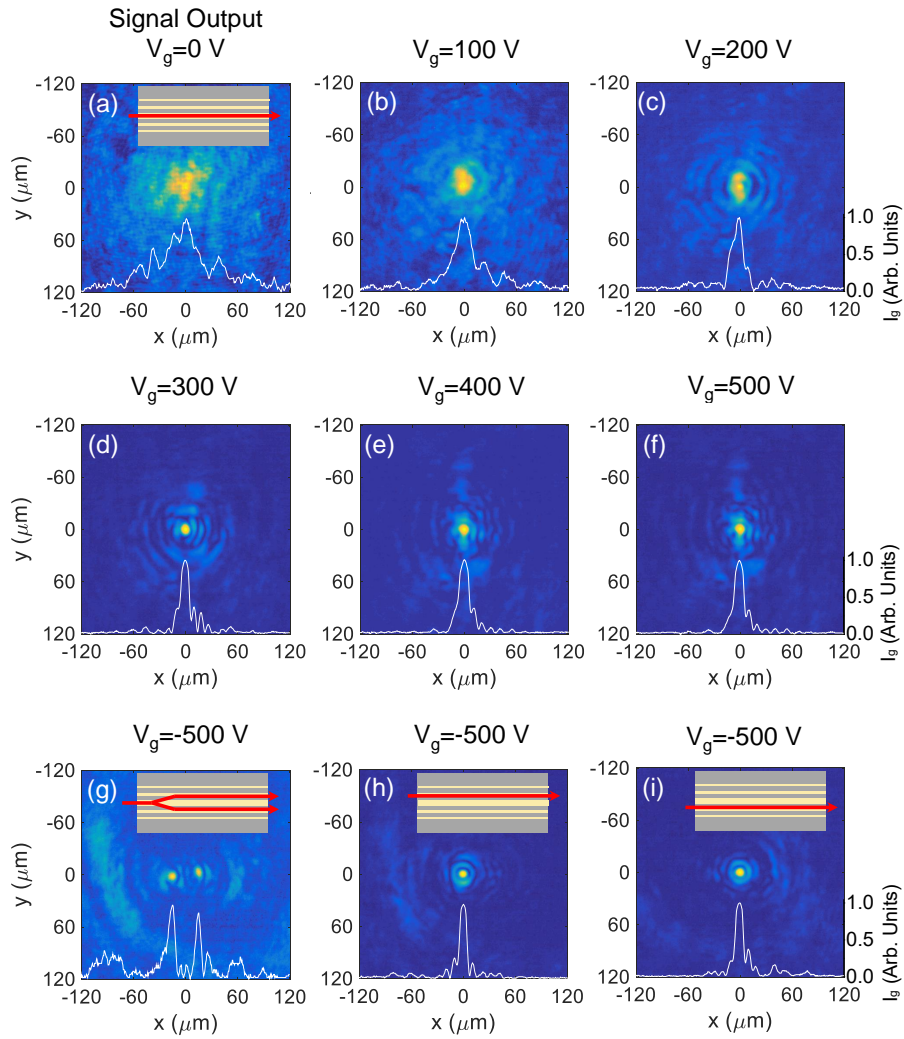


Figure 8.4. Electro-activating the BB waveguide. (a)-(f) Output signal for different values of $V_g = 0 - 500$ V (for $V_w = 450$ V, $t = 360$ s). (g)-(i) Double waveguide structure for $(V_g/V_w) < 0$. Launching the input signal with $\Delta x = \Delta y = 0$ causes it to scatter and in part be trapped into two parallel beams (g), while each is found to operate as a single waveguide by shifting the sample of $\Delta x = 9 \mu\text{m}$ (h) and $\Delta x = -9 \mu\text{m}$ (i), respectively.

Interestingly, the simplified model of Eq. (8.5) does not capture all the details of the physical processes that intervene during the writing stage. Principal among these is the intrinsic anisotropy in the space-charge, associated to the fact that while the writing intensity distribution I_w is approximately circular-symmetric with respect to the propagation axis z , the external electric bias is delivered through parallel plates on the x -facets of the sample [188]. As previously observed for negatively biased soliton-induced waveguides [238], this anisotropy, for $V_g < 0$, causes the pattern to morph into two parallel guiding structures shifted laterally that scatters and partially splits an input beam launched in the position of the original BB waveguide (Fig. 8.4 (g)), while each single lateral waveguide can itself guide independently (Figs. 8.4 (h), (i)).

8.3.4

Multiple waveguides and beam-splitter

In Fig. 8.5 we demonstrate the ability to write different structures independently in the same sample in close proximity. In our specific demonstration, we fabricated two parallel waveguides at different distances. For a larger interwaveguide distance of $20 \mu\text{m}$, each waveguide acts independently, and no mode coupling is detected for the length of the sample L_z (Figs. 8.5 (a), (b)). For a distance of $15 \mu\text{m}$, mode coupling intervenes, and the waveguide pair acts as a more elaborate mutual phase-dependent directional-coupler (Figs. 8.5 (c)-(e)).

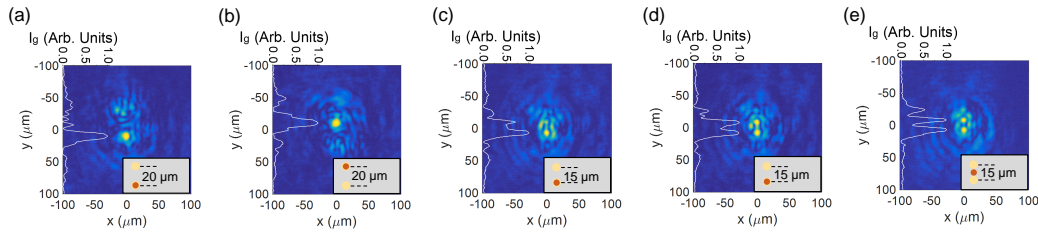


Figure 8.5. Coupling between two closely-packed parallel BB waveguides. Output signal intensity distribution for waveguides that are $20 \mu\text{m}$ apart when the signal input is launched into the first BB waveguide (a) with $\Delta y = 10 \mu\text{m}$ and into the second (b) with $\Delta y = -10 \mu\text{m}$. For our $L_z = 1.8 \text{ mm}$ sample, coupling between waveguides is found to be negligible. Reducing the interwaveguide distance now leads to coupling as shown in (c) and (d) where the same experiment is performed for waveguides that are $15 \mu\text{m}$ apart ($\Delta y = 7.5 \mu\text{m}$). Slight changes in T_g and V_g cause different coupling efficiency, as expected for directional coupling ((c) and (d) are taken with $\Delta T_g \simeq 0.5 \text{ K}$). (e) Output intensity distribution when the signal input is launched in between the two waveguides ($\Delta y = 0$). In the insets, yellow points represent the BB waveguides while red points indicate the input position of the signal Gaussian beam.

In Fig. 8.6 we demonstrate the use of BB waveguide writing to achieve 1×2 , 1×3 , and 1×4 splitters launching multiple angled BBs during the fabrication stage. The BBs are rendered mutually incoherent using a specific SLM time sequenced mask that turns on one BB at a time. This demonstrates how fabrication of complex

circuitry can also be achieved in a single illumination stage without having to mechanically shift and move the sample, as instead is required in direct writing scanning techniques.

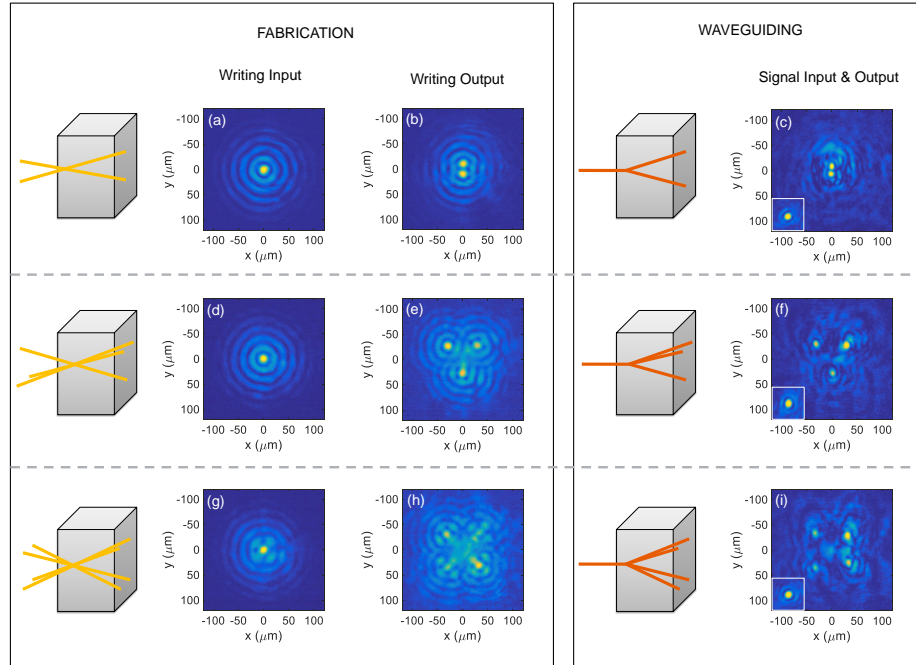


Figure 8.6. Multi-waveguide structures. (Left) Fabrication of a 1×2 (top), 1×3 (center), and 1×4 (bottom) splitter. 1×2 : (a) Input and (b) output intensity distributions of an incoherent superposition of two BBs with a mutual angle of 8.9 mrad. Fabrication writing input and output intensity distributions for a 1×3 (d),(e) and 1×4 (g),(h), where three and four incoherent BBs are launched at the input forming splitters with angles of 33.6 mrad and 35 mrad inside of the crystal, respectively. (Right) Output intensity distribution indicating the splitting of an input launch Gaussian beam at the center of the multi-beam pattern (see inset) for the 1×2 (c), 1×3 (f), and 1×4 (i) structures.

8.4

Reprogrammable optical networks

Previous studies have made use of diffraction-free Bessel beams to guide particles, atoms, and for material processing [239–244]. In this work we have demonstrated the use of single and multiple Bessel beams to optically write waveguides and electro-optic circuits in a bulk crystal. Our method is the first scalable method to realize reprogrammable optical networks in a full 3D setting.

Soliton interactions

One of the featuring properties of solitons is how they behave after a mutual interaction, a problem that is extensively studied for a great variety of different soliton [245–247]. Solitons manifest elastic and inelastic collision, so that, despite from their wave nature, they behave like particle. Furthermore, soliton interaction has seen a growing interest as a possible explanatory model for optical turbulence and rogue waves, one of the basic still-open questions in nonlinear wave physics [248–251]. In this Chapter, we investigate both single soliton collisions and three-soliton collisions, in photorefractive crystals, in conditions that can lead to RW formation.

9.1

Single soliton-soliton collisions

Long-tailed statistics and extreme phenomena observed in many different physical systems still lack a general explanatory picture [117, 252]. One established fact is that a microscopic nonreciprocal rectifying mechanism can cause anomalous fluctuations and ultimately bring about macroscopic, statistically improbable, events. This is well known for thermally agitated systems, where rectification is the driving mechanism of Brownian motors [253, 254]. Rogue waves (RWs) are localized extreme perturbations with impossibly high peak intensities and an associated long-tailed probability distribution [201, 249, 255–260]. It follows that a possible breakthrough in the understanding of RWs is the identification of an underlying dominant non-reciprocal energy exchange mechanism that acts to rectify fluctuations. In optical fibers and in photorefractive (PR) crystals, RWs form in time and in space, respectively, in conditions where wave propagation is dominated by interacting solitons [21, 261, 262]. While soliton collisions are elastic in a system obeying an integrable model, mixed systems [263] and non-integrable corrections allow energy and momentum exchange [264, 265]. This has been widely studied in open systems, such as for pulses propagating in externally pumped erbium-doped fibers [266, 267], and continuous-wave

ytterbium-doped fiber lasers [268]. For systems with no distributed amplification, typical of soliton and RW studies, local corrections, such as higher-order Kerr effects associated to saturation, are reciprocal and do not allow microscopic rectification. Non-reciprocal energy exchange between waves is mediated by the leading non-local nonlinear correction associated to Raman Scattering (RS) in fibers [269–272] and its equivalent in space, i.e., diffusion-driven two-wave-mixing (TWM) [273, 274]. Global non-reciprocity emerges as a consequence of time-nonlocality paired with causality in fibers and, equivalently, to the space-nonlocality paired with the direction of an external bias field. Previous studies into the effects of stimulated RS in soliton-soliton collisions have shown theoretically and experimentally how a weaker soliton can feed energy to a more intense one [275, 276]. Theoretical studies have generalized the picture to also include a limited soliton-soliton energy transfer [277], but still to date, no experimental evidence of a rectifying mechanism in soliton-soliton collisions has been reported. In the next sections, we investigate soliton-soliton collisions in PR crystals in conditions that can lead to RW formation [21].

9.1.1

Model

We consider light propagating in a biased crystal heated above the Curie temperature $T > T_C$, where anomalous dielectric response and structural metastability leads to a strong electro-optic effect [2, 3] with modulational instability, spatial solitons, and optical turbulence [21, 22, 278]. The system can be discussed in the simplified paraxial one-plus-one-dimensional (1+1D) case, that is, for beams that propagate along one axis, say the z axis, while they diffract and suffer self-focusing only in one transverse direction (the x -axis). The slowly varying amplitude A of the optical field obeys the Generalized-Nonlinear-Schrodinger-Equation (GNLSE)

$$i\partial_z A = -\frac{1}{2k}\partial_{xx}^2 A + \frac{k}{n_0}\Delta n(\bar{I})A, \quad (9.1)$$

where $k = 2\pi n_0/\lambda$, n_0 is the unperturbed crystal index of refraction, λ is the optical wavelength, and $\bar{I} = |A|^2/I_b$ is the optical intensity normalized to the homogeneous background illumination. The quadratic electro-optic effect leads to a nonlinear response $\Delta n(\bar{I})$ that reads [188, 279]

$$\Delta n(\bar{I}) = \Delta n_0 \left[\frac{1}{(1 + \bar{I})^2} + 2a \frac{\partial_x \bar{I}}{(1 + \bar{I})^2} + a^2 \left(\frac{\partial_x \bar{I}}{1 + \bar{I}} \right)^2 \right], \quad (9.2)$$

where $\Delta n_0 = (1/2)n_0^3 g_{eff} \varepsilon_0^2 \chi^2 E_0^2$, with g_{eff} the effective quadratic electro-optic coefficient, ε_0 the vacuum dielectric constant, $\chi = \epsilon_r - 1$ the low-frequency susceptibility, E_0 the bias electric field applied in the transverse x direction, and $a = k_B T / (q E_0)$, where k_B is the Boltzmann constant, T the sample temperature, and q the electron charge. The physical underpinnings involved are identified casting Eq. (9.2) in the dimensionless form

$$i\partial_\zeta u + \frac{1}{2}\partial_{\xi\xi}^2 u - \frac{1}{2} \frac{u}{(1 + |u|^2)^2} = t_d \frac{\partial_\xi |u|^2}{(1 + |u|^2)^2} u, \quad (9.3)$$

with $u = A/\sqrt{I_b}$, $|u|^2 = \bar{I}$, $\zeta = 2k\Delta n_0 z/n_0$, $\xi = kx\sqrt{2\Delta n_0/n_0}$, $t_d = ak\sqrt{2\Delta n_0/n_0}$, and the third term in Eq. (9.2), mediated solely by thermal charge diffusion, is neglected. This reduces to the Raman-modified Nonlinear-Schrodinger-Equation (NLSE) valid for conventional Kerr-like solitons in optical fiber in the unsaturated limit ($|u|^2 \ll 1$) [269]

$$i\partial_\zeta u + \frac{1}{2}\partial_{\xi\xi}^2 u + |u|^2 u = t_d \partial_\xi |u|^2 u. \quad (9.4)$$

The first term in Eq. (9.2), mediated by the PR screening of the external bias field caused by photoinduced charge drift, leads to the third term on the left-hand-side of Eqs. (9.3) and (9.4) and acts formally as Kerr self-focusing [188]. In turn, the second term in Eq. (9.2), mediated by the coupling of charge drift with charge thermal diffusion, leads to the term on the right-hand-side of Eqs. (9.3) and (9.4) and constitutes formally RS. In PR crystals both self-focusing and RS are caused by indirect steady-state photoinduced space-charge effects that have the same leading macroscopic nonlinear model of their counterparts encountered in fiber pulse propagation, while the microscopic origin is different in the two cases. Understandably, the unsaturated limit of Eq. (9.4) will be superseded by the full saturated version of the model in Eq. (9.3) in conditions leading to extreme wave amplitudes. The presence of a RS-like mechanism in Eq. (9.3) fundamentally alters the integrable NLSE in that it allows coherent energy exchange, or TWM, between solitons [280]. However, in distinction to other effects that break integrability, such as saturation in the response [281], here the transverse inversion symmetry $\xi \rightarrow -\xi$ is broken, and this introduces non-reciprocity in dynamics [273]. For example, in optical fiber, this broken symmetry is associated to causality in the response ($t_d > 0$) [269], so that RS is predicted to transfer energy to slower red-shifted giant-amplitude solitons [249, 261].

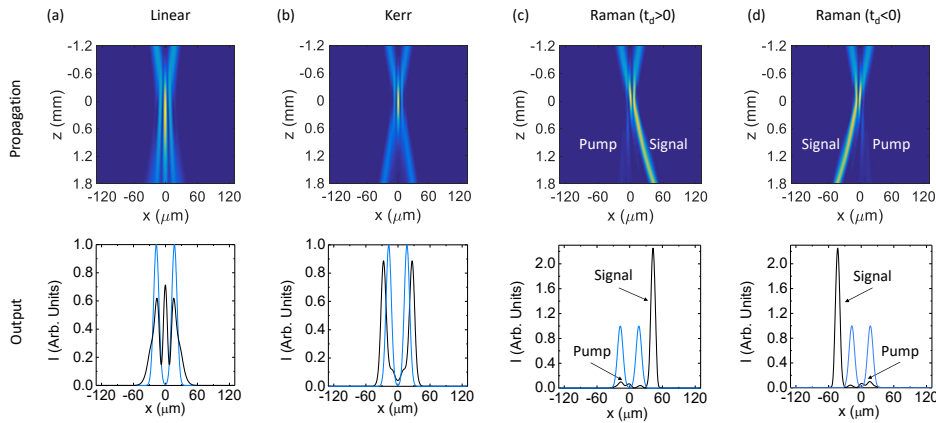


Figure 9.1. Strong non-reciprocal energy transfer in a soliton collision mediated by an RS-like correction. Top row: top-view intensity along propagation; second row: input (blue line) versus output (black line) transverse intensity profile. (a) Linear propagation for mutually coherent beams. (b) Nonlinear Kerr propagation in a model of negligible RS, compared to (c) and (d) where RS plays an important role.

In our present case, the non-reciprocity is associated to the sign of the external bias field E_0 , that determines the sign of a , and hence t_d , in Eq. (9.3). In Fig. 9.1 we show soliton TWM through a beam-propagation-method integration of Eq. (9.3) in the conditions investigated experimentally (see below). Energy exchange is associated to the RS-like correction (second versus third and fourth column) and occurs efficiently only for coherent collisions, while for incoherent collisions negligible energy transfer is found in all cases (see 9.1.4). The sign of t_d is determined by the relative orientation of the external bias field E_0 , for the specific photoinduced dominant ion charge q (electrons in our specific experiments), that then determines the direction of the non-reciprocal energy transfer (third and fourth columns) [185]. Note in Fig. 9.1 (c) and (d) how the solitons also self-bend during propagation in a direction fixed by t_d , a phenomenon associated to the RS-like correction that naturally leads to a redshift in the pulse spectrum [269, 275, 282, 283].

9.1.2

Experiments

Experiments are carried out in a compositionally disordered photorefractive KLTN crystal (Potassium-Lithium-Tantalate-Niobate - $\text{K}_{0.99}\text{Li}_{0.01}\text{Ta}_{0.60}\text{Nb}_{0.40}\text{O}_3$). The crystal was grown through the top-seeded solution method by extracting a zero-cut optical quality specimen that measures $L_x = 2.6$ mm, $L_y = 3.4$ mm, $L_z = 1.8$ mm along the x-y-z axes. It has an $n_0 = 2.3$ and a $g_{eff} = 0.14 \text{ m}^4\text{C}^{-2}$ when the optical polarization is parallel to one principal axis, say the x axis, also parallel to the external bias field $\mathbf{E}_0 = E_0\mathbf{u}_x$. The sample has a temperature-dependent quasi-static susceptibility: operating at a temperature close to the Curie point, $T = T_C + 6$ K, we achieve a high $\epsilon_r \simeq 1.5 \times 10^4$ that greatly enhances the electro-optic response. Soliton collisions are observed using the setup illustrated in Fig. 9.2. A $\lambda = 532$ nm continuous-wave 110 mW beam from a Nd:YAG laser is first expanded and made to propagate through a liquid-crystal spatial-light-modulator (SLM), sandwiched inbetween two crossed polarizers (POL1 and POL2).

A focusing lens (F1=60 mm) is used to image the transmitted light onto the input facet of the sample, with its principal axes along the x, y, z directions, generating the two colliding signal (I_s) and pump (I_p) beams. A voltage V is delivered to the opposite yz facets, so that $E_0 = V/L_x$. Propagation along the z axis, through the whole length of the sample L_z , is analyzed imaging the input and output facets through a second lens (F2=50 mm) onto a CCD camera.

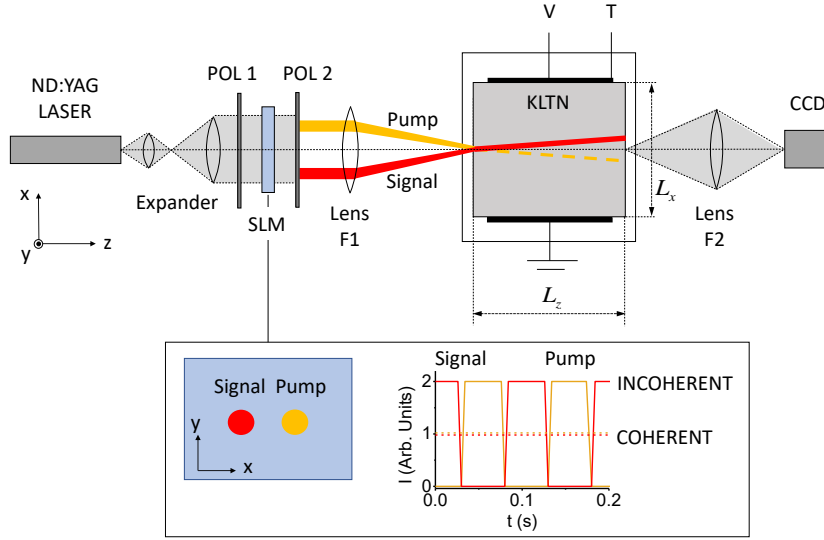


Figure 9.2. Experimental setup. The signal and pump beams are prepared in the transverse spatial wave-vector space using an intensity SLM. The inset shows temporal modulation of input signal and pump light that allows the study of incoherent collisions.

For the study of coherent collisions, both beams are transmitted by the SLM simultaneously (see the red and yellow illustrations in the inset of Fig. 9.2). For the study of incoherent collisions, each of the beams is alternatively switched on (with twice the intensity of the coherent experiment) and off so that at each instant in time only the signal or the pump are propagating through the sample. This amounts to an incoherent collision when the switching time (0.05 s) is much smaller than the characteristic response time of the nonlinearity (100 s, in our case).

9.1.3

Results

Results are reported in Fig. 9.3. The angle between the two crossing beams is $\theta = 12$ mrad (inside the sample) with their polarization parallel to the x-axis. The beams have the same power ($1 \mu\text{W}$), while the background illumination is 5% of each beam's peak intensity. When the two beams are coherent, for linear propagation (i.e., for $V = 0$), each $10 \mu\text{m}$ FWHM beam at the input (Fig. 9.3 (a)), spreads at the output to $45 \mu\text{m}$ (Fig. 9.3 (b)). A characteristic interference pattern forms (with a period $12 \mu\text{m}$ at input and $34 \mu\text{m}$ at output). For a $V = 330 \text{ V}$ ($t_d > 0$) a large portion of the energy from one soliton is transferred to the other, even though the two beams are only crossing for several hundred micrometers (Fig. 9.3 (c)).

Non-reciprocity is demonstrated by inverting the underlying asymmetry in the RS-like response, associated to the direction of the bias electric field. Congruently, for $V = -330 \text{ V}$ (i.e., $t_d < 0$), the same effect takes place but in the opposite direction (Fig. 9.3 (d)). The role of coherence is tested having the very same experiment take place but in conditions in which the two diffracting beams, and hence the resulting solitons, are mutually incoherent (see section 9.1.4).

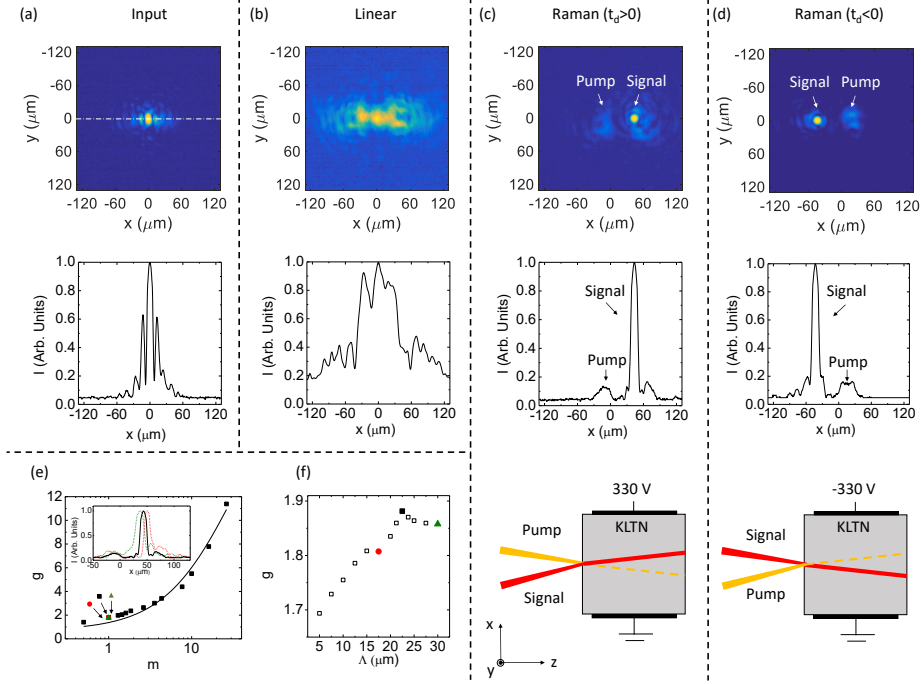


Figure 9.3. Extreme wave amplification through non-reciprocal energy transfer in a single soliton-soliton collision. (a) Input intensity distribution (top) and profile (bottom); (b) output intensity distribution and profile for linear propagation ($V = 0$). (c) Strong directional energy transfer for $t_d > 0$ and (d) $t_d < 0$. (e) TWM gain g versus input pump-signal m intensity ratio for a collision angle of $\theta = 12$ mrad (black squares). Red dot and green triangle are for $\theta = 15$ mrad and $\theta = 9$ mrad, respectively. The continuous line is the analytical prediction from Eq.(5). Inset: transverse intensity x -profiles for $m = 1$ and $\theta = 12$ mrad (black line), $\theta = 15$ mrad (red dashed line), $\theta = 9$ mrad (green dashed line). (f) TWM gain g versus interference grating period Λ for different inspected angles (red dot for $\theta = 15$ mrad, black square for $\theta = 12$ mrad, and green triangle for $\theta = 9$ mrad.) compared to those predicted (white squares) from numerical simulations.

Here the two solitons pass through each other with negligible exchange of energy and negligible dependence on the direction of the external bias. A signature of TWM is that the non-reciprocal amplification of the signal obeys the relationship [273]

$$g = \frac{I_s(L_z)}{I_s(0)} = \frac{1 + m}{1 + m e^{-\gamma L_i}} e^{-\alpha L_z} \quad (9.5)$$

where L_i is the interaction length and $m = I_p(0)/I_s(0)$ is the input pump/signal intensity ratio, γ is the two wave mixing gain coefficient, α is the absorption coefficient, and L_z is the length of the sample. In Fig. 9.3 (e) we report the measured soliton peak signal output-to-input intensity ratio g for different values of m (measured for peak input intensities) and the best fit to Eq. (9.5), for $L_i = 420 \mu\text{m}$, $L_z = 1.8$ mm, giving $\alpha = 2 \text{ cm}^{-1}$ and a giant soliton gain coefficient $\gamma = 80 \text{ cm}^{-1}$. The same experiment can be carried out with different collision angles θ , even if the available angles are limited in our scheme by the numerical aperture of the focusing lens

(NA=0.17). For comparison, in Fig. 9.3 (e) we include selected measurements with $\theta = 9$ mrad (green triangle) and 15 mrad (red dot), while in the inset of Fig. 9.3 (e) we compare the output soliton profiles for $\theta = 12$ mrad (black line) in Figs. 9.3 (c) and (d) ($m = 1$) to the results for $\theta = 9$ mrad (green dashed line) and 15 mrad (red dashed line). Results indicate the direction of non-reciprocal energy exchange ($g > 1$) is irrespective of m , so that on the sole basis of the sign of t_d (i.e., the direction of the external bias field), energy is transferred to the signal even when the signal itself is more intense than the pump. In Fig. 9.3 (f) we compare the values of TWM gain coefficient g versus transverse grating period Λ for $m = 1$ in the three measured cases of $\theta = 9$ (green triangle), 12 (black square), and 15 (red dot) mrad to the values predicted through numerical simulations (as in Fig. 9.1) (white squares). Even though the model is 1+1D while the experiment is 2+1D, and the TWM grating period is comparable to the transverse extent of the soliton collision (see the limited number of fringes in Figs. 9.1(c) and (d)), a good agreement is found.

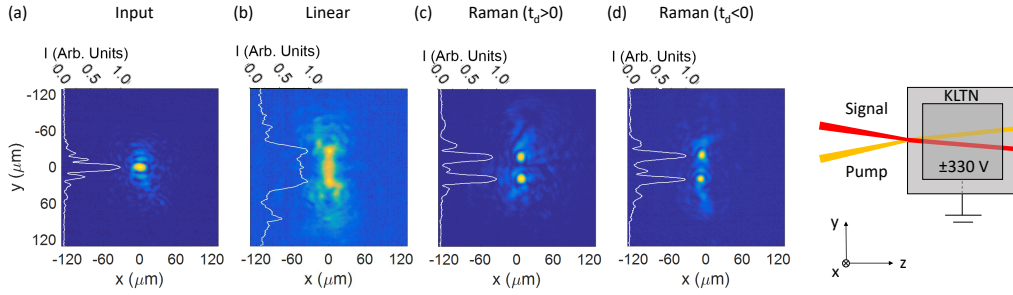


Figure 9.4. Absence of TWM when signal and pump solitons are physically not distinguished. (a) The input beams across inside the sample in the y direction and diffract for a linear propagation ($V = 0$) (b), leading to soliton formation with no non-reciprocal energy transfer for $t_d > 0$ (c), and $t_d < 0$ (d).

In Fig. 9.4 we report result for a collision that occurs in the yz plane, orthogonal to the x directed bias field. Since the geometry does not physically distinguish the signal and pump solitons, no TWM is observed. The comparison of collision in the xz and xy plane also indicates that the anisotropy that naturally accompanies two-dimensional PR solitons plays a negligible role in our experiments [238] (see section 9.1.4). In Fig. 9.5 we report the observation of reciprocal soliton fusion, i.e., the formation of a single output beam irrespective of the sign of t_d . The passage from a non-reciprocal to a reciprocal coherent interaction is achieved by matching the asymmetry introduced by the orientation of the external bias field along the x direction with a second asymmetry, achieved by shifting in the x direction the two transmitted spots on the SLM, thus rigidly rotating the two colliding beams around the y axis inside the sample.

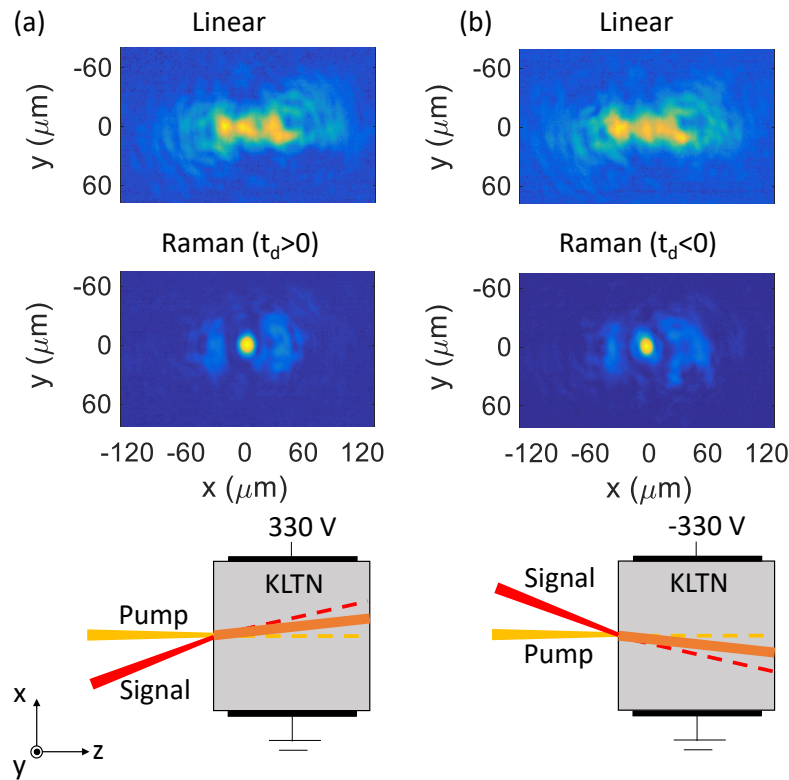


Figure 9.5. Soliton TWM and reciprocal fusion. For a colliding soliton-pair rigidly rotated around the y axis, pump and signal fuse into a single beam with (a) $t_d > 0$ (+6 mrad) and (b) $t_d < 0$ (-6 mrad). During the build-up of the nonlinear response, the originally crossing and diffracting beams at $t = 0$ fuse together at $t = 3$ min.

9.1.4

Numerical simulations

For each numerical and experimental result reported in the main text we carried out a comparative simulation and experiment using mutually incoherent pump and signal solitons. This allows us to identify the role of soliton TWM mediated by the nonlocal Raman-like mechanism, that can only intervene in the coherent case, and the role of conventional soliton-soliton energy exchange resulting from non-integrable corrections to the Kerr nonlinearity. Results are summarized in Fig. 9.6.

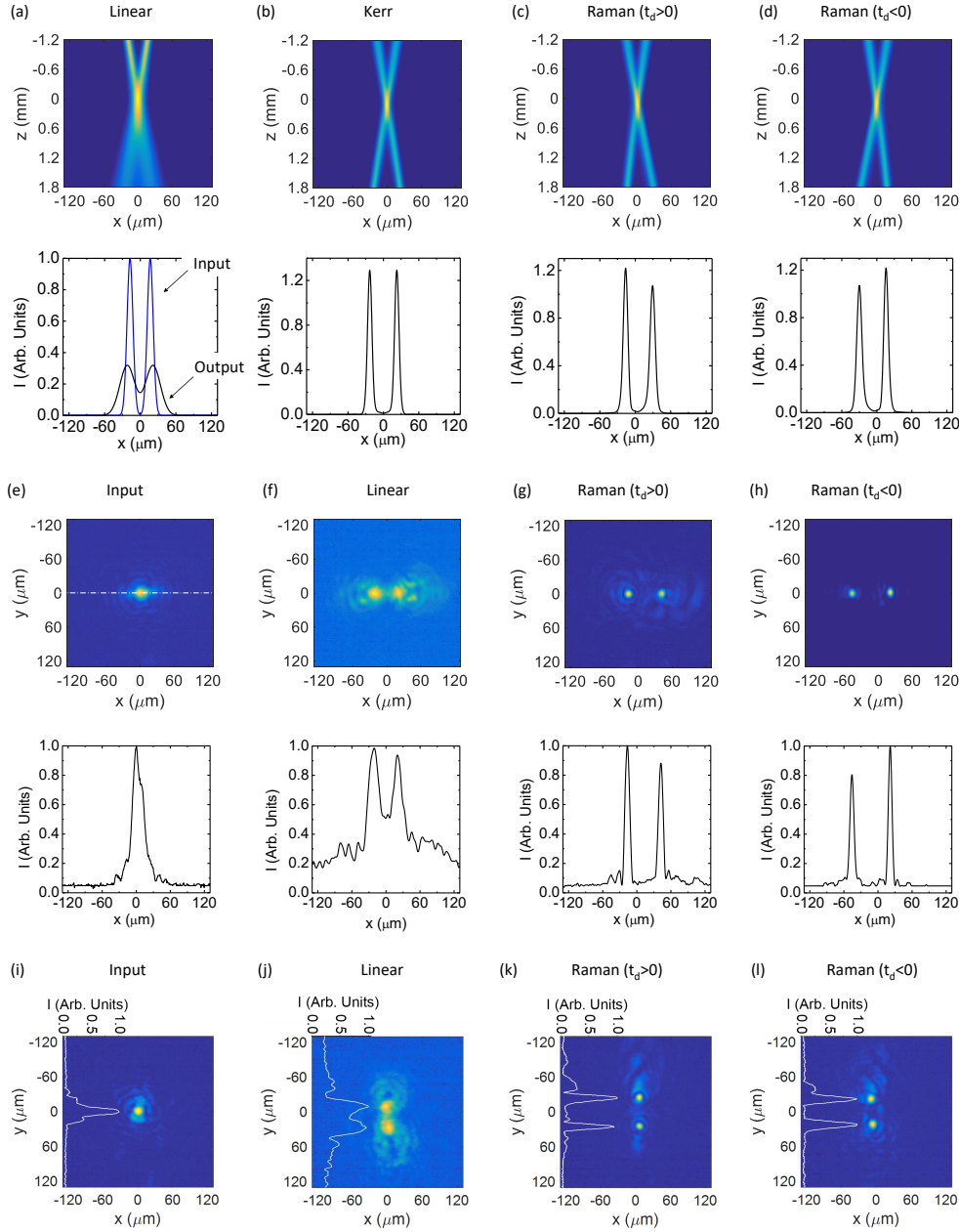


Figure 9.6. Incoherent soliton collisions. (a-d) Numerical 1+1D simulation of collisions between mutually incoherent solitons. (a) Linear propagation intensity distribution in the xz plane (top) and input/output x -profiles (bottom) compared to (b) Kerr, (c) Raman with $t_d > 0$, and (d) Raman with $t_d < 0$ models. (e-h) TWM experiments with mutually incoherent signal and pump solitons. (e) Input intensity distribution (top) and x -profile (bottom), (f) linear output, (g) and (h), nonlinear output for $t_d > 0$ and $t_d < 0$, respectively. (i-l) Incoherent soliton collisions in the yz plane, as for (e-h) but with y -profiles superimposed on the intensity distribution.

9.2

Microscopic rectification mechanism

Nonlinear waves can bounce off each other, spiral, and even fuse together. This leads to a rich wave phenomenology that includes counterintuitive effects such as optical turbulence [284] and wave condensation [285]. A basic hereto unsolved puzzle of nonlinear wave dynamics is the emergence of rogue waves, that in some systems form from a mixture of wave interaction, noise, and extreme nonlinear response, where dynamics are dominated by solitons [182, 286–289]. Our investigation indicates that in conditions where rogue waves form, soliton-soliton collisions are dominated by a non-reciprocal energy exchange with a giant two-wave-mixing gain up to 80 cm^{-1} . This provides a microscopic rectification mechanism, an asymmetric amplification, that can then explain out-of-equilibrium statistics not only in optics, but also in other wave systems such as sound and water waves.

9.3

Evidence of chaotic dynamics in three-soliton collisions

In the previous section we have seen that soliton-soliton nonreciprocal energy exchange mediated by the nonlinear Raman effect appears to play a key role in forming anomalously large red-shifted waves, amounting to a rectification mechanism for standard wave fluctuations [290, 291]. A missing trait in this explanatory picture is the absence of chaotic dynamics, a feature that, in turn, accompanies extreme wave formation [21, 262, 292–294]. The question naturally arises if chaos might arise out of three-soliton collisions in a manner that retraces what happens in classical mechanics, where chaos can emerge from collisions of three or more bodies [295, 296]. In fact, pioneering numerical [297] and experimental [298] studies into multi-soliton collisions have reported unusual output soliton behaviour and dependence on input parameters. Numerical evidence of a rich collisional soliton physics was also found in the interaction of so-called multi-soliton complexes, where coherence was found to play a dominant role [299–301]. An actual transition to chaos mediated by soliton interaction was first proposed for matter waves [302]. For these, solitons of the Gross-Pitaevskii Equation [303] were numerically found to manifest chaos in the aftermath of a three-soliton collision, while standard dynamics were found for a two-soliton collision. At present, such a transition to solitonic chaos in passing from two- to three-soliton collisions has not been reported. In the next sections we provide the experimental evidence of three-body-physics and a transition to chaos in the aftermath of a three-soliton collision in photorefractive KLTN. Chaotic behavior appears as the wave-system explores different soliton states, a solitonic chaos that is driven by coherent interaction mediated by the nonlinear Raman effect.

9.3.1

Experiments

Soliton collisions are investigated in a compositionally disordered photorefractive KLTN crystal (Potassium-Lithium-Tantalate-Niobate - $\text{K}_{0.99}\text{Li}_{0.01}\text{Ta}_{0.60}\text{Nb}_{0.40}\text{O}_3$). The crystal was grown through the top-seeded solution method by extracting a zero-cut optical quality specimen that measures $L_x = 2.6$ mm, $L_y = 3.4$ mm, $L_z = 1.8$ mm along the x-y-z axes.

Cu and V impurities give it a slight green color and cause a photorefractive response for visible light. The sample is kept in the paraelectric phase at $T = T_C + 6$ K, in proximity of its room-temperature Curie point $T_C = 292$ K, so that the resulting large $\epsilon_r \simeq 1.5 \times 10^4$ enhances the generally weak quadratic electro-optic response. In these conditions, it has an unperturbed index of refraction $n_0 = 2.3$ and an effective quadratic electro-optic coefficient $g_{eff} = g_{11} = 0.14 \text{ m}^4\text{C}^{-2}$ when the optical polarization is parallel to the externally applied bias electric field $E_0 = V/L_x$, delivered along the sample x direction. Experiments are performed using the setup illustrated in Fig. 9.7 (a). A laser beam from a doubled Nd:YAG laser ($\lambda = 532$ nm, CNI, model: MSL-FN-532-150mW) is first expanded and then made to propagate through a liquid-crystal spatial-light-modulator (SLM). The SLM is sandwiched inbetween two crossed polarizers (POL1 and POL2) so as to act as a 1024 by 1280 pixel computer-controlled intensity modulator. Modulation patterns are sent to the SLM to produce three separate Gaussian-like beams, illustrated in Fig. 9.7 (a) as beam 1, 2, and 3. These are then focused by a focal lens F1 (of focal length 75 mm) onto the input facet of the crystal, crossing inside it. The crystal is also illuminated with a background beam (not shown in Fig. 9.7 (a)), an expanded plane wave component from the laser of intensity I_b and polarization orthogonal to the soliton beams and bias field. It undergoes negligible nonlinear dynamics (the associated $g_{12} \ll g_{11}$), and serves to fix the saturation of the nonlinearity (see Ref. [188] for details). The intensity ratio between the peak intensity of each beam and the constant background illumination is $I_p/I_b \simeq 8$. Beam propagation along the z axis is analyzed imaging the input and output facets through a second lens (F2, 50 mm focal length) onto a CMOS camera (Thorlabs, DCC1545M). The resulting input and linear output intensity distributions are reported in Fig. 9.7 (b).

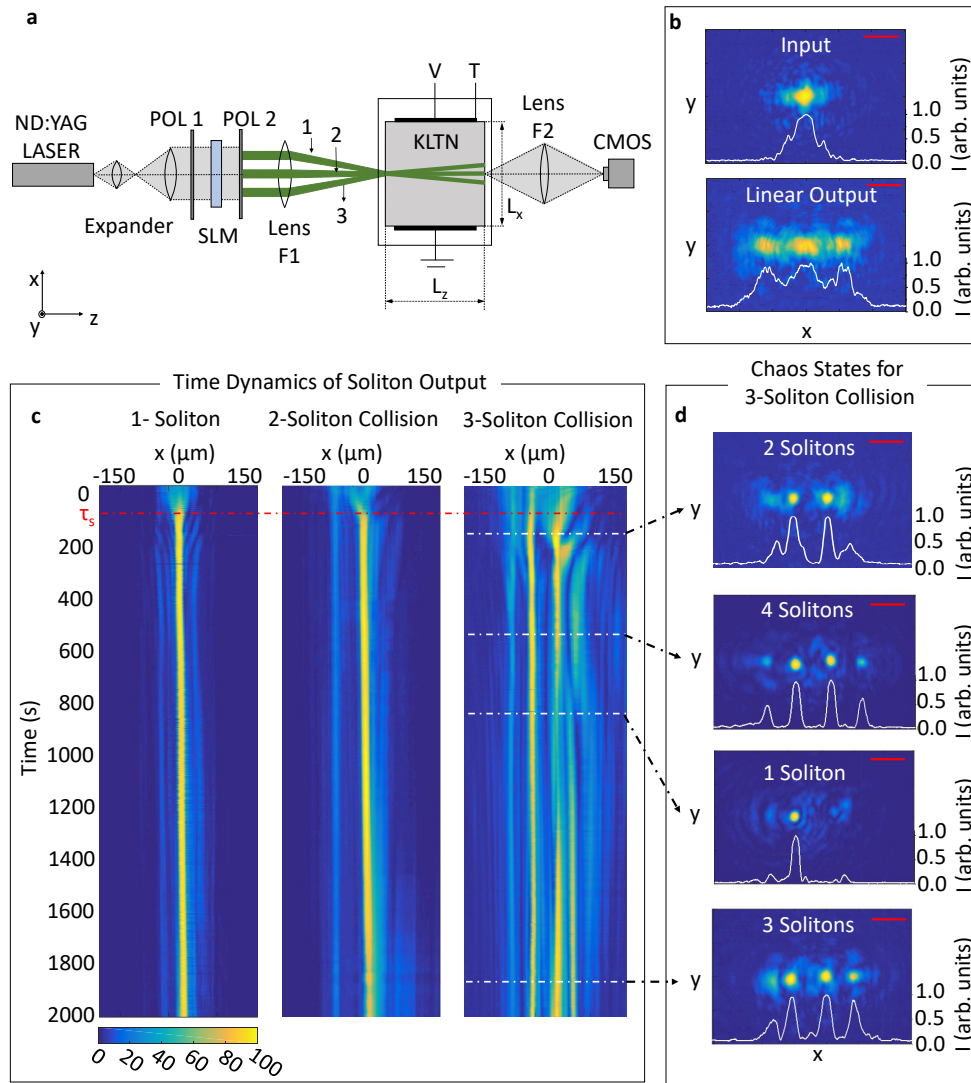


Figure 9.7. Chaotic behavior of 3-soliton coherent collisions. (a) Experimental setup. The three signal beams are prepared in the transverse spatial wave-vector space using an intensity SLM. (b) Top: input intensity distribution of three coherent beams colliding at the same position inside of the crystal at the input facet. Bottom: diffraction image at the output after linear propagation ($V = 0$). (c) The transverse intensity x -profile is analyzed versus time for a single soliton (Left), for a 2-soliton collision (middle), and for a sample 3-soliton collision (right). $\tau_s \simeq 80$ s is the soliton formation time. (d) Observed nonlinear soliton states, including a 1-soliton, 2-soliton, 3-soliton, and 4-soliton output. Images include the intensity distribution and a normalized intensity x -profile. The scale bar is for $50 \mu\text{m}$.

Coherent collisions

Steady-state spatial solitons, localized in the transverse xy -plane and propagating without spreading along the third z -axis (2+1D solitons) form with a $10\mu\text{m}$ FWHM after a $\tau_s \simeq 80$ s transient for $E_0 = V/L_x = 135\text{V}/\text{mm}$. In Fig. 9.7 (c) we compare soliton output time dynamics, i.e., the intensity profile along x -axis, for a single-soliton (left panel, only beam 2 is launched), a two-soliton collision (central panel, beams 1 and 3 launched), and a three-soliton collision (right panel, beams 1, 2, and 3 launched). While both the 1-soliton and 2-soliton time dynamics are regular, the 3-soliton collision manifests an irregular chaotic time process. Specifically, the 1-soliton and 2-soliton collisions lead to approximately the same output distribution, starting from very close initial conditions, with one soliton always forming at almost the same position and, for the 2-soliton case, with the same soliton-soliton energy transfer. In turn, in the 3-soliton collision, even starting from close initial conditions, the space-time dynamics are very different, manifesting 1-soliton, 2-soliton, 3-soliton, and 4-soliton distributions erratically at different time intervals. Fig. 9.7 (d) reported the discrete set of soliton states of the output intensity distribution taken from different time of 3-soliton collision time dynamics, switching erratically between 1-soliton, 2-soliton, 3-soliton, and 4-soliton output.

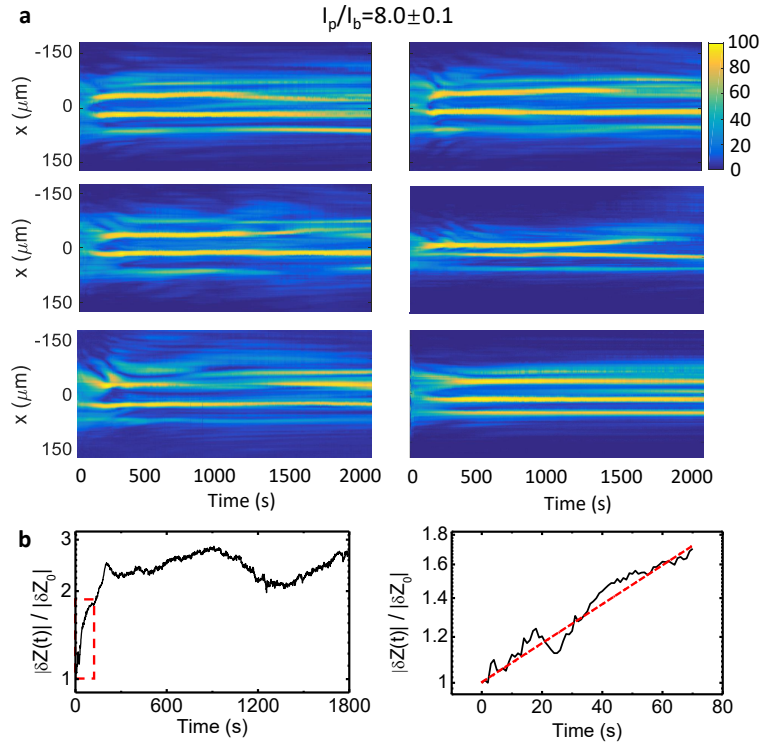


Figure 9.8. (a) A sample of six independent observed output intensity distributions (x -profile) versus exposure time t . (b) Lyapunov exponent analysis of the output time dynamics. The plot of $|\delta Z(t)|/|\delta Z_0|$ in logarithmic scale demonstrates the ratio between divergence at time t and initial divergence. Here, an average of the divergence over all nearby initial trajectories is fitted by $e^{\lambda_L t} = |\delta Z(t)|/|\delta Z_0|$. The right panel shows the exponent fitting result of $\lambda_L \simeq 0.0078/\text{s}$.

The chaotic nature of the associated time process is analyzed in Fig. 9.8. The transverse intensity x -profile dynamics are recorded versus time for different experiments, performed in the same initial setup conditions (see Fig. 9.8 (a) for a sample set of trajectories). The ratio between input peak intensity of each beam and the background illumination is $I_p/I_b = 8.0 \pm 0.1$ for all the subfigures in Fig. 9.8 (a). The uncertainty is associated to the fluctuation of the background scattering and, along with fluctuations in temperature ($\pm 0.5\text{K}$), acting as the initial small divergence $|\delta Z_0|$ of the trajectories of different events. The exponential divergence of a chaotic system is quantified by the so-called Lyapunov exponent λ_L , used to estimate the amount of chaos in a system [304].

For time series produced by dynamical systems, a $\lambda_L > 0$ signals chaos. Quantitatively, two trajectories in phase-space with initial separation vector δZ_0 diverge at a rate given by $|\delta Z(t)| = e^{\lambda_L t} |\delta Z_0|$, where $|\delta Z(t)|$ is the divergence at time t . In our analysis, $|\delta Z(t)| = (\sum_{i,j}^n D_{ij}(t))/n$ is an average divergence of the considered trajectories. $D_{ij}(t)$ is the divergence of two trajectories of the output intensity distributions $D_{ij}(t) = \sum_{x,y} |A_{ixy}(t) - A_{jxy}(t)|$, where $|A_{ixy}(t)|$ is the output intensity distribution of realization i at position (x,y) . The resulting average divergence of 3-soliton collisions is analyzed in Fig. 9.8 (b). The trajectories manifest an exponential divergence with Lyapunov exponent $\lambda_L \simeq 0.0078/\text{s}$ (standard error $1 \times 10^{-4}/\text{s}$), followed by saturation (for $t > 70$ s) as expected for a system governed by a chaotic (strange) attractor, because the trajectories will not depart from the attractor during the evolution [304].

Incoherent collisions

Multiple collision for mutually incoherent beams is investigated having each beam (i.e., beams 1, 2, and 3 in Fig. 9.7 (a) and Fig. 9.9 (a)) alternatively switched ON and OFF, so that at each instant in time only one beam is propagating through the sample. The SLM programming of the incoherent beams (solid lines) compared with coherent beams (dashed lines) is demonstrated in Fig. 9.9 (a) lower panel.

Each incoherent beam is three times more intense when ON relative to the coherent case, achieving an overall equal exposure to the coherent case. Furthermore, the switching cycle period (0.15 s) is taken to be much smaller than the characteristic response time of the nonlinearity ($\tau_d \simeq 100$ s, as shown in Fig. 9.9 (e)). Fig. 9.9 (b), (c) and (d) shows the input, linear output, and nonlinear output of the 3 incoherent beams, respectively. The resulting intensity pictures are achieved by adding up the frames of one switching cycle. In distinction to the coherent collision case of Figs. 9.7 and 9.8, here no transition to chaotic behavior is observed in passing from a 2-soliton to a 3-soliton collision, as shown in Fig. 9.9 (e) for time dynamics of incoherent 3-soliton collisions.

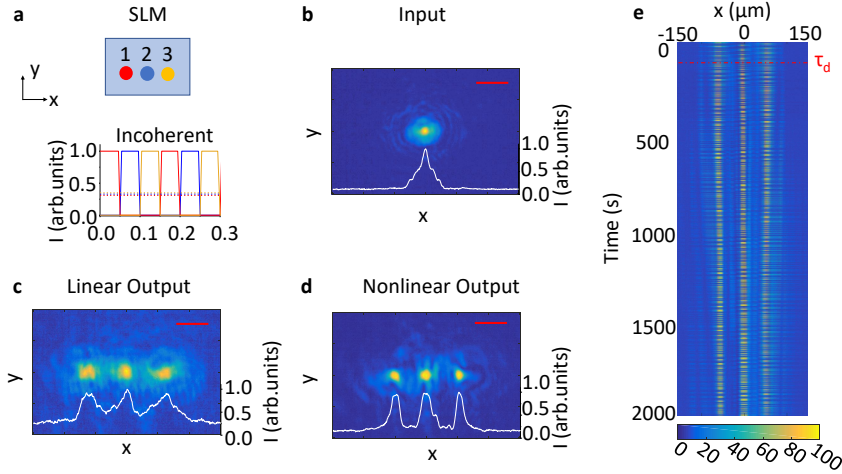


Figure 9.9. Incoherent soliton collisions. (a) Experimental scheme: the SLM is programmed to allow only one of the three input soliton beams to propagate at one time, alternating between beam 1 (labeled by red) beam 2 (labeled by blue) and beam 3 (labeled by yellow). Note that the colors are used to distinguish different beams that all have the same wavelength ($\lambda=532$ nm). (b) Input intensity distribution, (c) output after linear propagation ($V = 0$), and (d) nonlinear 3-soliton output state in an electric field of $V = 350$ V (the resulting intensity frames were added to create the images in b-d). The scale bar is for $50 \mu\text{m}$. (e) Time dynamics of incoherent 3-soliton collision, in which no chaotic behavior is observed.

9.3.2

Model

To address the physical mechanisms involved in the transition to chaos observed in the coherent 3-soliton collision, we consider the simplified 1+1D nonlinear paraxial equation governing optical propagation.

$$i\partial_z A = -\frac{1}{2k}\partial_{xx}^2 A + \frac{k}{n_0}\Delta n(I, t)A. \quad (9.6)$$

Here z is the propagation axis, x is the transverse plane, A is the slowly varying component of the optical field $E_{opt} = A(x, z)\exp(-ikz)$ along the x axis, $k = 2\pi n_0/\lambda$, n_0 is the unperturbed crystal index of refraction, λ is the optical wavelength, and $I = |A|^2$ is the optical intensity. $\Delta n(I, t)$ is the photorefractive nonlinearity that has accumulated after an exposure time t , and reads in the paraelectric phase [188, 279]

$$\Delta n(I, t) = \Delta n_0 Y^2, \quad (9.7)$$

where $\Delta n_0 = (1/2)n_0^3 g_{eff} \varepsilon_0^2 \chi^2 E_0^2$, with g_{eff} the effective quadratic electro-optic coefficient, ε_0 the vacuum dielectric constant, $\chi = \epsilon_r - 1$ the low-frequency susceptibility, E_0 the time-independent bias electric field applied in the transverse x direction, and $Y = E/E_0$. The accumulated Y obeys [188]

$$\frac{\partial Y(\xi, \tau)}{\partial \tau} + Q(\xi, \tau)Y(\xi, \tau) + a \frac{\partial Q(\xi, \tau)}{\partial \xi} = G. \quad (9.8)$$

Here $\xi = x/x_q$, where $x_q = \varepsilon_0 E_0 / (N_a q)$ is the saturation length, N_a is the concentration of acceptor impurities, $\tau = t/\tau_d$, where $\tau_d = \varepsilon_0 \gamma / (q \mu s \alpha I_b)$ is the dielectric relaxation time, γ the recombination constant, μ the charge mobility, and s is connected to the absorption cross-section. Moreover, $\alpha = N_d / N_a$, N_d is the concentration of donors, $Q = (I + I_b) / I_b$, $a = k_B T / (q E_0 x_q)$, k_B is the Boltzmann constant, T the sample temperature, and q the electron charge. In these conditions,

$$Y = e^{-\int_0^\tau Q d\tau'} \left(G + G \int_0^\tau d\tau' e^{\int_0^{\tau'} Q d\tau''} \right) + e^{-\int_0^\tau Q d\tau'} \int_0^\tau d\tau' a \frac{\partial Q}{\partial \xi} e^{\int_0^{\tau'} Q d\tau''}. \quad (9.9)$$

Inserting Y into Eq. ((9.7)) and taking the steady-state limit (i.e., $\tau \gg 1$) leads to

$$\Delta n(I) / \Delta n_0 = 1/Q^2 - 2a \partial_\xi Q / Q^2 + a^2 (\partial_\xi Q)^2 / Q^2, \quad (9.10)$$

where the first term physically embodies the saturated Kerr self-focusing nonlinearity, the second is the saturated nonlinear Raman-like effect [269], while the third term is negligible [290].

9.3.3

Numerical results

Numerical results of 3-soliton collisions are reported in Fig. 9.10 for a subset of experimental conditions (coherent/incoherent, input peak intensity ratio I_p/I_b , Δn_0 , and Raman coefficient a ¹). Time dynamics for specific realizations are reported in Figs. 9.10 (a-d) and (j). In qualitative agreement with experimental findings, the simulation on coherent 3-soliton collisions demonstrates time evolution trajectories of the output with the formation of a 1-soliton (Fig. 9.10 (e)), 2-soliton (Fig. 9.10 (f)), 3-soliton (Fig. 9.10 (h)), and 4-soliton (Fig. 9.10 (g)) state at specific instants of time.

¹3-soliton collisions are simulated using 3D matrix, i.e., one time dimension (t) plus two space dimensions (x and z). A time loop is set up in which the xz propagation is calculated numerically solving Eq. ((9.6)) by means of the beam propagation method (BPM) [305]. For each i -th time step, Δn is determined by Eqs.((9.7)) and ((9.9)) for a fixed time t_i , as τ_d is much larger than the propagation time. The $(i+1)$ -th step is then calculated with Δn evaluated at $t_{i+1} = t_i + \Delta t$ from Eqs. 9.7 and 9.9 using the Q evaluated in the i -th step.

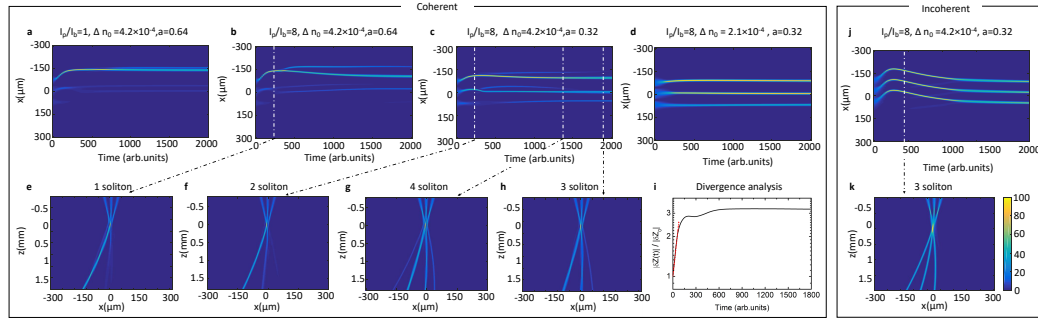


Figure 9.10. Simulating a 3-soliton collision. (a-d) Output time evolution for mutually coherent solitons in various conditions of input intensity ratio I_p/I_b , nonlinear response Δn_0 , and Raman coefficient a ($a = k_B T / (qE_0 x_q)$), including 1-soliton (e), 2-soliton (f), 4-soliton (g), and 3-soliton (h) outcomes. (i) Divergence (in logarithm scale) analysis of coherent 3-soliton collisions fitted by $e^{\lambda_L t} = |\delta Z(t)|/|\delta Z_0|$ (red dashed line). (j) 3-soliton output time evolution for mutually incoherent solitons and (k) corresponding 3-soliton outcome. In distinction to the coherent case, here no chaotic dynamics is observed, and different input conditions have a minimal effect on the output state.

As in experiments (see Fig. 9.8 (b)), divergence analysis of numerical trajectories manifests an exponential stage followed by saturation in the attractor (Fig. 9.10 (i)). While the chaotic nature by the 3-soliton collision means that simulation will not reproduce the exact details for single trajectory (i.e., Fig. 9.8 (a)), it does allow the prediction of the set of observed output soliton states (Fig. 9.7 (d)) of the underlying strange attractor. The strong output soliton-state dynamics in time become negligible as Δn_0 is lessened (the onset of a regular behavior that can be appreciated in Fig. 9.10 (d)). The Δn_0 threshold value ($\sim 2.1 \times 10^{-4}$) of the 1+1D simulation is in agreement with the threshold observed for the 2+1D experiments ($\sim 2 \times 10^{-4}$). As reported in Fig. 9.10 (j-k), in agreement with experimental findings, a 3-soliton incoherent collision leads to regular behavior, with a soliton-number-preserving 3-soliton output, in direct analogy to standard 2-soliton collisions (coherent/incoherent).

9.4

Evidence of chaotic dynamics

Both experimental and numerical results indicate that a 3-soliton coherent collision manifests irregular dynamics (Fig. 9.7, Fig. 9.8, and Figs. 9.10 (a-i)) while an incoherent one does not (Fig. 9.9 and Figs. 9.10 (j,k)). The basic difference between the coherent and incoherent collision is that in the coherent collision the nonlinear Raman interaction (the second term in Eq. (9.10)) causes strong energy exchange mediated by soliton-wave-mixing², while in the incoherent case, it only causes the single solitons to self-bend [175, 188], the spatial equivalent of the Raman-induced soliton red-shift observed in optical pulses in fibers [269]. It follows that the irregular exploration of the multi-soliton output states observed after a 3-soliton collision is driven by coherent energy exchange mediated by the nonlinear Raman effect, a feature it shares with spatial rogue wave formation [290]. The driving role of the Raman correction now explains why the simplified 1+1D simulation is able to capture the salient features of the strange attractor. In fact, since the Raman correction is the result of the coupling between the diffusion space-charge field and the external bias field, which is along the x direction, the energy exchange and hence chaotic behavior is relegated to the single transverse x direction. We further note that numerical results highlight how the specific output soliton state depends strongly on the input intensity ratio and on the specific value of Δn_0 and a (see selected examples in Fig. 9.10 (a-d)). This helps explain why chaotic dynamics arise readily observed in proximity of the sample Curie point. In fact, since the quasi-static susceptibility follows the Curie-Weiss law, $\Delta n_0 \propto \chi^2 \sim 1/(T - T_C)^2$, even minimal thermal fluctuations allow the system to explore the entire family of available soliton-output states. Our system is modeled by a nonintegrable nonlinearity, not only because of the Raman correction, but more fundamentally because it is saturated (see Eq. (9.10)). An interesting development may be to experimentally analyze multi-soliton collisions in systems whose leading model is an integrable nonlinearity [306, 307].

9.4.1

Applicative perspective

Chaotic soliton behavior is observed when more than two solitons are made to collide and in conditions in which soliton-soliton coherent energy exchange is efficient. Since these are also the conditions in which rogue waves and optical turbulence are observed, our findings suggest that multi-soliton collisions may play a key role in extreme wave formation. From an applicative perspective, the ability to access chaos directly from soliton collisions can form the basis for all-optical random number generators and chaos-based secure optical transmission schemes.

²We note that while coherence is found to play a major role, the actual relative phase of input beams does not alter soliton-soliton wave-mixing (see Eq. (9.8) and Ref. [290]), and hence hardly affects chaotic behavior.

Conclusions

The first part of the work presented in this Thesis reports several new findings in nanodisordered ferroelectric crystals in the super-crystal (SC) phase. Starting with the characterization of this new phase, studying the optical polarization dynamics, we find that the ordered polar domains can coherently modify the polarization of light, forming a checkerboard-like polarization pattern, with an alternating linear polarization parallel to the SC principal axes. Results suggest the possibility of using ferroelectric SC in photonic applications, for example, based on polarization control. The most surprising novelty of this new phase is that it is accompanied by a giant index of refraction ($n > 26$) for the whole visible spectrum, without absorption. The result is a material able to project visible light, of any color, and even white incoherent light, from its input to its output, without diffraction and chromatic dispersion, irrespective of beam size, numerical aperture, wavelength, coherence (from single-mode laser to white projector lamp light), intensity, and input direction. Moreover, the achromatic and diffraction-free nature of optical propagation in the material makes an ideal setting for nonlinear optical processes, such as second-harmonic generation. We demonstrate how the presence of giant refraction allows the wavelength conversion process to occur with a broad angular, spectral, and polarization acceptance, even without the fulfillment of phase-matching conditions. All these findings open up a route for the development of a new platform, based on giant refraction, to achieve miniaturized achromatic light manipulation. Moreover, the enhanced nonlinear functionality opens hereto unexplored applications in imaging. The specific 3D geometry of the SC, with its spatially ordered and periodic birefringent polar clusters and its giant optical refraction, allows us to explore ferroelectric cluster dynamics under the effect of a bias electric field, using a 3D orthographic projection technique. In this case, the electric field is able to switch off the effect of giant refraction, through a percolative transition, by causing the ferroelectric sample to form a disordered array of polar nanoregions, effectively causing critical opalescence. Findings shed light on the nature and susceptibility of ferroelectric SC. They suggest a specific role for organized 3D polarization structures below the Curie temperature, which can have profound repercussions on the development of future information storing technology. From a structural point of view, an interesting point on SC phase arises from the X-ray diffraction experiments. We found an unconventional deformation in the average atomic structure compatible with the strain field caused by the vortex polar domain distribution of our SC model. We then corroborate the results obtained on the atomic scale through calorimetry,

optical diffraction, dielectric, and second-harmonic generation experiments. Albeit all these findings have led to a better understanding of this new ferroelectric phase of matter, the physical mechanism allowing giant refraction remains a still open question. Experimental and theoretical investigation are still on going.

In the second part of this thesis, we used nanodisordered ferroelectric crystals to study nonlinear waves dynamics, due to their strong optical properties. From an applicative point of view, we demonstrate the feasibility of Bessel beam writing to build a scalable and a rewritable network of waveguides inside the bulk ferroelectric medium. While studying experimentally both single and three solitons collisions, we have identified a soliton amplification and rectification in the first case and a chaotic dynamics in the second one. These findings represent a possible response to a still open question regarding the mechanism leading to the formation of rogue waves.

Bibliography

- [1] S. D. Stranks and H. J. Snaith, “Metal-halide perovskites for photovoltaic and light-emitting devices”, *Nature nanotechnology*, vol. 10, no. 5, p. 391, 2015.
- [2] Y.-C. Chang, C. Wang, S. Yin, R. C. Hoffman, and A. G. Mott, “Giant electro-optic effect in nanodisordered ktn crystals”, *Optics letters*, vol. 38, no. 22, pp. 4574–4577, 2013.
- [3] D Pierangeli, F Di Mei, J Parravicini, G. Parravicini, A. Agranat, C Conti, and E DelRe, “Observation of an intrinsic nonlinearity in the electro-optic response of freezing relaxor ferroelectrics”, *Optical Materials Express*, vol. 4, no. 8, pp. 1487–1493, 2014.
- [4] X. Zhang, S. He, Z. Zhao, P. Wu, X. Wang, and H. Liu, “Abnormal optical anisotropy in correlated disorder $\text{KTa}_{1-x}\text{Nb}_x\text{O}_3$: Cu with refractive index gradient”, *Scientific reports*, vol. 8, no. 1, p. 2892, 2018.
- [5] V. V. Shvartsman and D. C. Lupascu, “Lead-free relaxor ferroelectrics”, *Journal of the American Ceramic Society*, vol. 95, no. 1, pp. 1–26, 2012.
- [6] K. M. Rabe, M. Dawber, C. Lichtensteiger, C. H. Ahn, and J.-M. Triscone, “Modern physics of ferroelectrics: Essential background”, *Physics of Ferroelectrics*, pp. 1–30, 2007.
- [7] F. Jona and G. Shirane, *Ferroelectric crystals, international series of monographs on solid state physics*. Pergamon press Oxford, UK: 1962.
- [8] E. DelRe, B. Crosignani, M. Tamburrini, M. Segev, M. Mitchell, E. Refaeli, and A. J. Agranat, “One-dimensional steady-state photorefractive spatial solitons in centrosymmetric paraelectric potassium lithium tantalate niobate”, *Optics letters*, vol. 23, no. 6, pp. 421–423, 1998.
- [9] D Pierangeli, M Flammini, F Di Mei, J Parravicini, C. de Oliveira, A. Agranat, and E DelRe, “Continuous solitons in a lattice nonlinearity”, *Physical review letters*, vol. 114, no. 20, p. 203 901, 2015.
- [10] M. Flammini, G. Di Domenico, D. Pierangeli, F. Di Mei, A. J. Agranat, and E. DelRe, “Observation of bessel-beam self-trapping”, *Physical Review A*, vol. 98, no. 3, p. 033 808, 2018.

-
- [11] D. Pierangeli, M. Flammini, L. Zhang, G. Marcucci, A. J. Agranat, P. G. Grinevich, P. M. Santini, C. Conti, and E. DelRe, “Observation of fermi-pasta-ulam-tsingou recurrence and its exact dynamics”, *Phys. Rev. X*, vol. 8, p. 041 017, 4 2018.
- [12] G. A. Samara, “The relaxational properties of compositionally disordered ABO_3 perovskites”, *Journal of Physics: Condensed Matter*, vol. 15, no. 9, 2003.
- [13] A. Bokov and Z.-G. Ye, “Recent progress in relaxor ferroelectrics with perovskite structure”, *Journal of materials science*, vol. 41, no. 1, pp. 31–52, 2006.
- [14] G. Burns and F. Dacol, “Glassy polarization behavior in ferroelectric compounds pb $(Mg_{13}Nb_{23}) O_3$ and Pb $(Zn_{13}Nb_{23}) O_3$ ”, *Solid state communications*, vol. 48, no. 10, pp. 853–856, 1983.
- [15] J. Trull, C. Cojocar, R. Fischer, S. M. Saltiel, K. Staliunas, R. Herrero, R. Vilaseca, D. N. Neshev, W. Krolikowski, and Y. S. Kivshar, “Second-harmonic parametric scattering in ferroelectric crystals with disordered nonlinear domain structures”, *Optics express*, vol. 15, no. 24, pp. 15 868–15 877, 2007.
- [16] V. Roppo, W. Wang, K. Kalinowski, Y Kong, C. Cojocar, J. Trull, R. Vilaseca, M. Scalora, W. Krolikowski, and Y. Kivshar, “The role of ferroelectric domain structure in second harmonic generation in random quadratic media”, *Optics Express*, vol. 18, no. 5, pp. 4012–4022, 2010.
- [17] M. Ayoub, J. Imbrock, and C. Denz, “Second harmonic generation in multi-domain χ^2 media: From disorder to order”, *Optics express*, vol. 19, no. 12, pp. 11 340–11 354, 2011.
- [18] E. DelRe, E. Spinozzi, A. J. Agranat, and C. Conti, “Scale-free optics and diffractionless waves in nanodisordered ferroelectrics”, *Nature Photonics*, vol. 5, no. 1, p. 39, 2011.
- [19] E. DelRe, F. Di Mei, J. Parravicini, G. Parravicini, A. J. Agranat, and C. Conti, “Subwavelength anti-diffracting beams propagating over more than 1,000 rayleigh lengths”, *Nature Photonics*, vol. 9, no. 4, p. 228, 2015.
- [20] F Di Mei, P Caramazza, D Pierangeli, G Di Domenico, H Ilan, A. Agranat, P Di Porto, and E DelRe, “Intrinsic negative mass from nonlinearity”, *Physical review letters*, vol. 116, no. 15, p. 153 902, 2016.
- [21] D Pierangeli, F Di Mei, C Conti, A. Agranat, and E DelRe, “Spatial rogue waves in photorefractive ferroelectrics”, *Physical review letters*, vol. 115, no. 9, p. 093 901, 2015.
- [22] D Pierangeli, F Di Mei, G Di Domenico, A. Agranat, C Conti, and E DelRe, “Turbulent transitions in optical wave propagation”, *Physical review letters*, vol. 117, no. 18, p. 183 902, 2016.
- [23] Q. Lu, B. Li, Z. Li, and B. Ge, “Field-induced lifetime enhancement of photorefractive gratings in a Mn: Fe: KTN crystal”, *Optics letters*, vol. 42, no. 13, pp. 2407–2410, 2017.

-
- [24] A. Gumennik, Y. Kurzweil-Segev, and A. J. Agranat, “Electrooptical effects in glass forming liquids of dipolar nano-clusters embedded in a paraelectric environment”, *Optical Materials Express*, vol. 1, no. 3, pp. 332–343, 2011.
- [25] H. Tian, B. Yao, C. Hu, X. Meng, and Z. Zhou, “Impact of polar nanoregions on the quadratic electro-optic effect in $K_{0.95}Na_{0.05}Ta_{1-x}Nb_xO_3$ crystals near the curie temperature”, *Applied Physics Express*, vol. 7, no. 6, p. 062601, 2014.
- [26] D Pierangeli, J Parravicini, F Di Mei, G. Parravicini, A. Agranat, and E DelRe, “Photorefractive light needles in glassy nanodisordered kntn”, *Optics letters*, vol. 39, no. 6, pp. 1657–1660, 2014.
- [27] P. Tan, H. Tian, C. Hu, X. Meng, C. Mao, F. Huang, G. Shi, and Z. Zhou, “Temperature field driven polar nanoregions in $KTa_{1-x}Nb_xO_3$ ”, *Applied Physics Letters*, vol. 109, no. 25, p. 252904, 2016.
- [28] X. Meng, H. Tian, P. Tan, F. Huang, R. Zhang, and Z. Zhou, “Strong electromechanical coupling in paraelectric $KTa_{1-x}Nb_xO_3$ crystals”, *Journal of the American Ceramic Society*, vol. 100, no. 11, pp. 5220–5225, 2017.
- [29] H. Tian, B. Yao, L. Wang, P. Tan, X. Meng, G. Shi, and Z. Zhou, “Dynamic response of polar nanoregions under an electric field in a paraelectric $KTa_{0.61}Nb_{0.39}O_3$ single crystal near the para-ferroelectric phase boundary”, *Scientific reports*, vol. 5, p. 13751, 2015.
- [30] P. Tan, H. Tian, C. Mao, C. Hu, X. Meng, L. Li, G. Shi, and Z. Zhou, “Field-driven electro-optic dynamics of polar nanoregions in nanodisordered $KTa_{1-x}Nb_xO_3$ crystal”, *Applied Physics Letters*, vol. 111, no. 1, p. 012903, 2017.
- [31] D. Viehland, S. Jang, L. E. Cross, and M. Wuttig, “Freezing of the polarization fluctuations in lead magnesium niobate relaxors”, *Journal of Applied Physics*, vol. 68, no. 6, pp. 2916–2921, 1990.
- [32] R. Pirc and R. Blinc, “Vogel-fulcher freezing in relaxor ferroelectrics”, *Physical review B*, vol. 76, no. 2, p. 020101, 2007.
- [33] S Prosandeev, D. Wang, A. Akbarzadeh, B Dkhil, and L Bellaiche, “Field-induced percolation of polar nanoregions in relaxor ferroelectrics”, *Physical review letters*, vol. 110, no. 20, p. 207601, 2013.
- [34] J. Parravicini, E. DelRe, A. J. Agranat, and G. Parravicini, “Liquid–solid directional composites and anisotropic dipolar phases of polar nanoregions in disordered perovskites”, *Nanoscale*, vol. 9, no. 27, pp. 9572–9580, 2017.
- [35] K. J. Choi, M. Biegalski, Y. Li, A Sharan, J Schubert, R. Uecker, P Reiche, Y. Chen, X. Pan, V. Gopalan, *et al.*, “Enhancement of ferroelectricity in strained $BaTiO_3$ thin films”, *Science*, vol. 306, no. 5698, pp. 1005–1009, 2004.
- [36] H. N. Lee, H. M. Christen, M. F. Chisholm, C. M. Rouleau, and D. H. Lowndes, “Strong polarization enhancement in asymmetric three-component ferroelectric superlattices”, *Nature*, vol. 433, no. 7024, pp. 395–399, 2005.

- [37] V. Garcia, S. Fusil, K. Bouzouane, S. Enouz-Vedrenne, N. D. Mathur, A. Barthelemy, and M. Bibes, “Giant tunnel electroresistance for non-destructive readout of ferroelectric states”, *Nature*, vol. 460, no. 7251, pp. 81–84, 2009.
- [38] W.-H. Kim, J. Y. Son, Y.-H. Shin, and H. M. Jang, “Imprint control of non-volatile shape memory with asymmetric ferroelectric multilayers”, *Chemistry of Materials*, vol. 26, no. 24, pp. 6911–6914, 2014.
- [39] M. Dawber, K. Rabe, and J. Scott, “Physics of thin-film ferroelectric oxides”, *Reviews of modern physics*, vol. 77, no. 4, p. 1083, 2005.
- [40] G Catalan, A Janssens, G Rispens, S Csiszar, O Seeck, G Rijnders, D. H. Blank, and B. Noheda, “Polar domains in lead titanate films under tensile strain”, *Physical review letters*, vol. 96, no. 12, p. 127 602, 2006.
- [41] G. Catalan, A. Lubk, A. Vlooswijk, E. Snoeck, C Magen, A Janssens, G. Rispens, G Rijnders, D. H. Blank, and B. Noheda, “Flexoelectric rotation of polarization in ferroelectric thin films”, *Nature materials*, vol. 10, no. 12, pp. 963–967, 2011.
- [42] A. Biancoli, C. M. Fancher, J. L. Jones, and D. Damjanovic, “Breaking of macroscopic centric symmetry in paraelectric phases of ferroelectric materials and implications for flexoelectricity”, *Nature materials*, vol. 14, no. 2, pp. 224–229, 2015.
- [43] E. Bousquet, M. Dawber, N. Stucki, C. Lichtensteiger, P. Hermet, S. Gariglio, J.-M. Triscone, and P. Ghosez, “Improper ferroelectricity in perovskite oxide artificial superlattices”, *Nature*, vol. 452, no. 7188, pp. 732–736, 2008.
- [44] S. Callori, J Gabel, D. Su, J Sinsheimer, M. Fernandez-Serra, and M Dawber, “Ferroelectric $\text{PbTiO}_3/\text{SrRuO}_3$ superlattices with broken inversion symmetry”, *Physical review letters*, vol. 109, no. 6, p. 067 601, 2012.
- [45] A. L. Roytburd, J. Ouyang, and A. Artemev, “Polydomain structures in ferroelectric and ferroelastic epitaxial films”, *Journal of Physics: Condensed Matter*, vol. 29, no. 16, p. 163 001, 2017.
- [46] G. Catalan, J Seidel, R. Ramesh, and J. F. Scott, “Domain wall nanoelectronics”, *Reviews of Modern Physics*, vol. 84, no. 1, p. 119, 2012.
- [47] P. Zubko, J. C. Wojdel, M. Hadjimichael, S. Fernandez-Pena, A. Sené, I. Luk’yanchuk, J.-M. Triscone, and J. Íñiguez, “Negative capacitance in multidomain ferroelectric superlattices”, *Nature*, vol. 534, no. 7608, pp. 524–528, 2016.
- [48] A. K. Yadav, K. X. Nguyen, Z. Hong, P. García-Fernández, P. Aguado-Puente, C. T. Nelson, S. Das, B. Prasad, D. Kwon, S. Cheema, *et al.*, “Spatially resolved steady-state negative capacitance”, *Nature*, vol. 565, no. 7740, pp. 468–471, 2019.
- [49] V. Stoica, N Laanait, C Dai, Z Hong, Y Yuan, Z Zhang, S Lei, M. McCarter, A Yadav, A. Damodaran, *et al.*, “Optical creation of a supercrystal with three-dimensional nanoscale periodicity”, *Nature materials*, vol. 18, no. 4, pp. 377–383, 2019.

-
- [50] M. Hadjimichael, Y. Li, E. Zatterin, G. A. Chahine, M. Conroy, K. Moore, E. N. O'Connell, P. Ondrejovic, P. Marton, J. Hlinka, *et al.*, "Metal-ferroelectric supercrystals with periodically curved metallic layers", *Nature Materials*, vol. 20, no. 4, pp. 495–502, 2021.
- [51] D Pierangeli, M Ferraro, F Di Mei, G Di Domenico, C. De Oliveira, A. Agranat, and E DelRe, "Super-crystals in composite ferroelectrics", *Nature communications*, vol. 7, p. 10674, 2016.
- [52] G. N. Ramachandran, *Advanced Methods of Crystallography*. Academic Press, Inc., 1964.
- [53] L. Wang, H. Tian, X. Meng, H. Chen, Z. Zhou, and Y. Shen, "Field-induced enhancement of voltage-controlled diffractive properties in paraelectric iron and manganese co-doped potassium–tantalate–niobate crystal", *Applied Physics Express*, vol. 7, no. 11, p. 112601, 2014.
- [54] J Parravicini, R. M. Lorente, F Di Mei, D Pierangeli, A. Agranat, and E DelRe, "Volume integrated phase modulator based on funnel waveguides for reconfigurable miniaturized optical circuits", *Optics letters*, vol. 40, no. 7, pp. 1386–1389, 2015.
- [55] A. Bitman, N. Sapiens, L. Secundo, A. J. Agranat, G. Bartal, and M. Segev, "Electroholographic tunable volume grating in the g 44 configuration", *Optics letters*, vol. 31, no. 19, pp. 2849–2851, 2006.
- [56] C Menzel, C Helgert, C Rockstuhl, E.-B. Kley, A Tünnermann, T Pertsch, and F Lederer, "Asymmetric transmission of linearly polarized light at optical metamaterials", *Physical review letters*, vol. 104, no. 25, p. 253902, 2010.
- [57] E Plum, X.-X. Liu, V. Fedotov, Y Chen, D. Tsai, and N. Zheludev, "Metamaterials: Optical activity without chirality", *Physical review letters*, vol. 102, no. 11, p. 113902, 2009.
- [58] J. B. Mueller, N. A. Rubin, R. C. Devlin, B. Groever, and F. Capasso, "Metasurface polarization optics: Independent phase control of arbitrary orthogonal states of polarization", *Physical Review Letters*, vol. 118, no. 11, p. 113901, 2017.
- [59] M.-X. Ren, W. Wu, W. Cai, B. Pi, X.-Z. Zhang, and J.-J. Xu, "Reconfigurable metasurfaces that enable light polarization control by light", *Light: Science & Applications*, vol. 6, no. 6, e16254–e16254, 2017.
- [60] R. Khomeriki, L. Chotorlishvili, I. Tralle, and J. Berakdar, "Positive–negative birefringence in multiferroic layered metasurfaces", *Nano letters*, vol. 16, no. 11, pp. 7290–7294, 2016.
- [61] P.-F. Li, Y.-Y. Tang, Z.-X. Wang, H.-Y. Ye, Y.-M. You, and R.-G. Xiong, "Anomalous rotary polarization discovered in homochiral organic ferroelectrics", *Nature communications*, vol. 7, no. 1, pp. 1–9, 2016.
- [62] W Kleemann, F. Schäfer, and D Rytz, "Diffuse ferroelectric phase transition and long-range order of dilute $k\text{Ta}_{1-x}\text{Nb}_x\text{O}_3$ ", *Physical review letters*, vol. 54, no. 18, p. 2038, 1985.

- [63] V Westphal, W Kleemann, and M. Glinchuk, “Diffuse phase transitions and random-field-induced domain states of the “relaxor”ferroelectric $\text{PbMg}_{1/3}\text{Nb}_{2/3}\text{O}_3$ ”, *Physical Review Letters*, vol. 68, no. 6, p. 847, 1992.
- [64] M Takagi and T Ishidate, “Anomalous birefringence of cubic BaTiO_3 ”, *Solid state communications*, vol. 113, no. 7, pp. 423–426, 2000.
- [65] A. Pugachev, V. Kovalevskii, N. Surovtsev, S Kojima, S. Prosandeev, I. Raevski, and S. Raevskaya, “Broken local symmetry in paraelectric BaTiO_3 proved by second harmonic generation”, *Physical review letters*, vol. 108, no. 24, p. 247601, 2012.
- [66] J. Parravicini, E. DelRe, A. J. Agranat, and G. Parravicini, “Macroscopic response and directional disorder dynamics in chemically substituted ferroelectrics”, *Physical Review B*, vol. 93, no. 9, p. 094203, 2016.
- [67] A. Yariv and P. Yeh, *Optical waves in crystals*. John Wiley & Sons, New York, 1984, vol. 5.
- [68] A. Shevchenko, M. Roussey, A. T. Friberg, and T. Setälä, “Polarization time of unpolarized light”, *Optica*, vol. 4, no. 1, pp. 64–70, 2017.
- [69] S. W. Hell, “Far-field optical nanoscopy”, *Science*, vol. 316, no. 5828, pp. 1153–1158, 2007.
- [70] M. L. Brongersma, Y. Cui, and S. Fan, “Light management for photovoltaics using high-index nanostructures”, *Nature materials*, vol. 13, no. 5, pp. 451–460, 2014.
- [71] T. Chang, J. U. Kim, S. K. Kang, H. Kim, D. K. Kim, Y.-H. Lee, and J. Shin, “Broadband giant-refractive-index material based on mesoscopic space-filling curves”, *Nature communications*, vol. 7, no. 1, pp. 1–7, 2016.
- [72] M. Choi, S. H. Lee, Y. Kim, S. B. Kang, J. Shin, M. H. Kwak, K.-Y. Kang, Y.-H. Lee, N. Park, and B. Min, “A terahertz metamaterial with unnaturally high refractive index”, *Nature*, vol. 470, no. 7334, pp. 369–373, 2011.
- [73] E. D. Palik, *Handbook of optical constants of solids*. Academic press, 1998, vol. 3.
- [74] A. Yariv, *Quantum Electronics*. John Wiley & Sons, New York, 1967.
- [75] M. Born and E. Wolf, *Principles of optics: electromagnetic theory of propagation, interference and diffraction of light*. Cambridge University Press, 2005.
- [76] A. A. Bokov and Z.-G. Ye, “Dielectric relaxation in relaxor ferroelectrics”, *Journal of Advanced dielectrics*, vol. 2, no. 02, p. 1241010, 2012.
- [77] M Ferraro, D Pierangeli, M Flammini, G Di Domenico, L Falsi, F Di Mei, A. Agranat, and E DelRe, “Observation of polarization-maintaining light propagation in depoled compositionally disordered ferroelectrics”, *Optics letters*, vol. 42, no. 19, pp. 3856–3859, 2017.
- [78] P. Bons, R de Haas, D de Jong, A Groot, and P van der Straten, “Quantum enhancement of the index of refraction in a bose-einstein condensate”, *Physical review letters*, vol. 116, no. 17, p. 173602, 2016.

-
- [79] K. Im, J.-H. Kang, and Q.-H. Park, “Universal impedance matching and the perfect transmission of white light”, *Nature Photonics*, vol. 12, no. 3, pp. 143–149, 2018.
- [80] F. Aieta, M. A. Kats, P. Genevet, and F. Capasso, “Multiwavelength achromatic metasurfaces by dispersive phase compensation”, *Science*, vol. 347, no. 6228, pp. 1342–1345, 2015.
- [81] S. M. Mansfield and G. Kino, “Solid immersion microscope”, *Applied physics letters*, vol. 57, no. 24, pp. 2615–2616, 1990.
- [82] J. B. Pendry, D. Schurig, and D. R. Smith, “Controlling electromagnetic fields”, *science*, vol. 312, no. 5781, pp. 1780–1782, 2006.
- [83] D. E. Chang, V. Vuletić, and M. D. Lukin, “Quantum nonlinear optics—photon by photon”, *Nature Photonics*, vol. 8, no. 9, p. 685, 2014.
- [84] L. Caspani, C. Xiong, B. J. Eggleton, D. Bajoni, M. Liscidini, M. Galli, R. Morandotti, and D. J. Moss, “Integrated sources of photon quantum states based on nonlinear optics”, *Light: Science & Applications*, vol. 6, no. 11, e17100, 2017.
- [85] R. W. Boyd, *Nonlinear Optics, 3rd ed.* Academic Press, Inc., 2008.
- [86] Y.-R. Shen, “The principles of nonlinear optics”, *New York*, 1984.
- [87] R. Loudon, *The quantum theory of light, 3rd ed.* Oxford Science Publications, 2010.
- [88] E. Brown, T. McKee, A. Pluen, B. Seed, Y. Boucher, R. K. Jain, *et al.*, “Dynamic imaging of collagen and its modulation in tumors in vivo using second-harmonic generation”, *Nature medicine*, vol. 9, no. 6, pp. 796–800, 2003.
- [89] T. Tiecke, J. D. Thompson, N. P. de Leon, L. Liu, V. Vuletić, and M. D. Lukin, “Nanophotonic quantum phase switch with a single atom”, *Nature*, vol. 508, no. 7495, pp. 241–244, 2014.
- [90] A. Reiserer, N. Kalb, G. Rempe, and S. Ritter, “A quantum gate between a flying optical photon and a single trapped atom”, *Nature*, vol. 508, no. 7495, pp. 237–240, 2014.
- [91] D. Wei, C. Wang, H. Wang, X. Hu, D. Wei, X. Fang, Y. Zhang, D. Wu, Y. Hu, J. Li, *et al.*, “Experimental demonstration of a three-dimensional lithium niobate nonlinear photonic crystal”, *Nature Photonics*, vol. 12, no. 10, pp. 596–600, 2018.
- [92] T. Xu, K. Switkowski, X. Chen, S. Liu, K. Koynov, H. Yu, H. Zhang, J. Wang, Y. Sheng, and W. Krolikowski, “Three-dimensional nonlinear photonic crystal in ferroelectric barium calcium titanate”, *Nature Photonics*, vol. 12, no. 10, pp. 591–595, 2018.
- [93] X. Zhang, Q. Yang, H. Liu, X. Wang, S. He, X. Li, and P. Wu, “Switching effects of spontaneously formed superlattices in relaxor ferroelectrics”, *Optical Materials Express*, vol. 9, no. 10, pp. 4081–4089, 2019.

-
- [94] S. Liu, K. Switkowski, C. Xu, J. Tian, B. Wang, P. Lu, W. Krolikowski, and Y. Sheng, “Nonlinear wavefront shaping with optically induced three-dimensional nonlinear photonic crystals”, *Nature communications*, vol. 10, no. 1, pp. 1–7, 2019.
- [95] J. Jelley, *Čerenkov Radiation, and Its Applications*. United Kingdom Atomic Energy Authority, 1958.
- [96] E. Mathieu, “Conditions for quasi čerenkov radiation, generated by optical second harmonic polarisation in a nonlinear cristal”, *Zeitschrift für angewandte Mathematik und Physik ZAMP*, vol. 20, no. 4, pp. 433–439, 1969.
- [97] P. Tien, R. Ulrich, and R. Martin, “Optical second harmonic generation in form of coherent čerenkov radiation from a thin-film waveguide”, *Applied Physics Letters*, vol. 17, no. 10, pp. 447–450, 1970.
- [98] Y. Zhang, Z. Gao, Z. Qi, S. Zhu, and N. Ming, “Nonlinear čerenkov radiation in nonlinear photonic crystal waveguides”, *Physical review letters*, vol. 100, no. 16, p. 163904, 2008.
- [99] Y. Sheng, A. Best, H.-J. Butt, W. Krolikowski, A. Arie, and K. Koynov, “Three-dimensional ferroelectric domain visualization by čerenkov-type second harmonic generation”, *Optics express*, vol. 18, no. 16, pp. 16539–16545, 2010.
- [100] Y. Sheng, Q. Kong, V. Roppo, K. Kalinowski, Q. Wang, C. Cojocar, and W. Krolikowski, “Theoretical study of čerenkov-type second-harmonic generation in periodically poled ferroelectric crystals”, *JOSA B*, vol. 29, no. 3, pp. 312–318, 2012.
- [101] V. Roppo, K. Kalinowski, Y. Sheng, W. Krolikowski, C. Cojocar, and J. Trull, “Unified approach to čerenkov second harmonic generation”, *Optics express*, vol. 21, no. 22, pp. 25715–25726, 2013.
- [102] R. Ni, L. Du, Y. Wu, X. Hu, J. Zou, Y. Sheng, A. Arie, Y. Zhang, and S. Zhu, “Nonlinear čerenkov difference-frequency generation exploiting birefringence of ktp”, *Applied Physics Letters*, vol. 108, no. 3, p. 031104, 2016.
- [103] F. Di Mei, L. Falsi, M. Flammini, D. Pierangeli, P. Di Porto, A. Agranat, and E. DelRe, “Giant broadband refraction in the visible in a ferroelectric perovskite”, *Nature Photonics*, vol. 12, no. 12, pp. 734–738, 2018.
- [104] J. Armstrong, N. Bloembergen, J. Ducuing, and P. S. Pershan, “Interactions between light waves in a nonlinear dielectric”, *Physical review*, vol. 127, no. 6, p. 1918, 1962.
- [105] D. Kleinman, “Theory of second harmonic generation of light”, *Physical Review*, vol. 128, no. 4, p. 1761, 1962.
- [106] M. M. Fejer, G. Magel, D. H. Jundt, and R. L. Byer, “Quasi-phase-matched second harmonic generation: Tuning and tolerances”, *IEEE Journal of quantum electronics*, vol. 28, no. 11, pp. 2631–2654, 1992.
- [107] S. M. Saitel, D. N. Neshev, W. Krolikowski, A. Arie, O. Bang, and Y. S. Kivshar, “Multiorder nonlinear diffraction in frequency doubling processes”, *Optics letters*, vol. 34, no. 6, pp. 848–850, 2009.

-
- [108] Y. Amnon and P. Yeh, “Optical waves in crystals: Propagation and control of laser radiation”, *New York City, NY: Wiley*, 2002.
- [109] J.-s. Wang, K.-j. Jin, J.-x. Gu, Q. Wan, H.-b. Yao, and G.-z. Yang, “Direct evidence of correlation between the second harmonic generation anisotropy patterns and the polarization orientation of perovskite ferroelectric”, *Scientific reports*, vol. 7, no. 1, pp. 1–6, 2017.
- [110] P. Molina, M. d. l. O. Ramirez, and L. E. Bausa, “Strontium barium niobate as a multifunctional two-dimensional nonlinear “Photonic Glass””, *Advanced Functional Materials*, vol. 18, no. 5, pp. 709–715, 2008.
- [111] Z. Bor and B Racz, “Dispersion of optical materials used for picosecond spectroscopy”, *Applied optics*, vol. 24, no. 21, pp. 3440–3441, 1985.
- [112] P Molina, S Alvarez-Garcia, M. Ramírez, J García-Solé, L. Bausá, H. Zhang, W. Gao, J. Wang, and M. Jiang, “Nonlinear prism based on the natural ferroelectric domain structure in calcium barium niobate”, *Applied Physics Letters*, vol. 94, no. 7, p. 071 111, 2009.
- [113] L. Mateos, P. Molina, J. Galisteo, C. López, L. E. Bausá, and M. O. Ramírez, “Simultaneous generation of second to fifth harmonic conical beams in a two dimensional nonlinear photonic crystal”, *Optics express*, vol. 20, no. 28, pp. 29 940–29 948, 2012.
- [114] H. Li, S. Mu, P Xu, M. Zhong, C. Chen, X. Hu, W. Cui, and S. Zhu, “Multicolor čerenkov conical beams generation by cascaded- χ (2) processes in radially poled nonlinear photonic crystals”, *Applied Physics Letters*, vol. 100, no. 10, p. 101 101, 2012.
- [115] H. Zhang, X. He, Y. Shih, K. Harshavardhan, and L. Knauss, “Optical and nonlinear optical study of $\text{KTa}_{0.52}\text{Nb}_{0.48}\text{O}_3$ epitaxial film”, *Optics letters*, vol. 22, no. 23, pp. 1745–1747, 1997.
- [116] H. Suchowski, K. O’Brien, Z. J. Wong, A. Salandrino, X. Yin, and X. Zhang, “Phase mismatch-free nonlinear propagation in optical zero-index materials”, *Science*, vol. 342, no. 6163, pp. 1223–1226, 2013.
- [117] J.-P. Bouchaud, “Weak ergodicity breaking and aging in disordered systems”, *Journal de Physique I*, vol. 2, no. 9, pp. 1705–1713, 1992.
- [118] V. Wadhawan, *Introduction to ferroic materials*. CRC press, 2000.
- [119] D. Stauffer and A. Aharony, *Introduction to percolation theory*. CRC press, 2018.
- [120] A. L. Roytburd, S. Alpay, L. Bendersky, V Nagarajan, and R Ramesh, “Three-domain architecture of stress-free epitaxial ferroelectric films”, *Journal of Applied Physics*, vol. 89, no. 1, pp. 553–556, 2001.
- [121] N.-T. Tsou, P. Potnis, and J. Huber, “Classification of laminate domain patterns in ferroelectrics”, *Physical Review B*, vol. 83, no. 18, p. 184 120, 2011.
- [122] Y Nahas, S Prokhorenko, L Louis, Z Gui, I. Kornev, and L. Bellaiche, “Discovery of stable skyrmionic state in ferroelectric nanocomposites”, *Nature communications*, vol. 6, no. 1, pp. 1–6, 2015.

- [123] S. Prosandeev, B. Xu, and L. Bellaiche, “Polarization switching in the pbmg 1/3 nb 2/3 o 3 relaxor ferroelectric: An atomistic effective hamiltonian study”, *Physical Review B*, vol. 98, no. 2, p. 024105, 2018.
- [124] I Muench, A. R. Balakrishna, and J. Huber, “Periodic boundary conditions for the simulation of 3d domain patterns in tetragonal ferroelectric material”, *Archive of Applied Mechanics*, vol. 89, no. 6, pp. 955–972, 2019.
- [125] S. Lerner, P. B. Ishai, A. Agranat, and Y. Feldman, “Percolation of polar nanoregions: A dynamic approach to the ferroelectric phase transition”, *Journal of non-crystalline solids*, vol. 353, no. 47-51, pp. 4422–4427, 2007.
- [126] R. Viswanathan and M. B. Heaney, “Direct imaging of the percolation network in a three-dimensional disordered conductor-insulator composite”, *Physical review letters*, vol. 75, no. 24, p. 4433, 1995.
- [127] N. Shimoni, D. Azulai, I. Balberg, and O. Millo, “Tomographic-like reconstruction of the percolation cluster as a phase transition”, *Physical Review B*, vol. 66, no. 2, p. 020102, 2002.
- [128] L. Falsi, L. Tartara, F. Di Mei, M. Flammini, J. Parravicini, D. Pierangeli, G. Parravicini, F. Xin, P. DiPorto, A. J. Agranat, *et al.*, “Constraint-free wavelength conversion supported by giant optical refraction in a 3d perovskite supercrystal”, *Communications Materials*, vol. 1, no. 1, pp. 1–8, 2020.
- [129] C. Li, X. Wang, Y. Wu, F. Liang, F. Wang, X. Zhao, H. Yu, and H. Zhang, “Three-dimensional nonlinear photonic crystal in naturally grown potassium–tantalate–niobate perovskite ferroelectrics”, *Light: Science & Applications*, vol. 9, no. 1, pp. 1–8, 2020.
- [130] K Du, M Zhang, C Dai, Z. Zhou, Y. Xie, Z. Ren, H Tian, L. Chen, G. Van Tendeloo, and Z Zhang, “Manipulating topological transformations of polar structures through real-time observation of the dynamic polarization evolution”, *Nature communications*, vol. 10, no. 1, pp. 1–8, 2019.
- [131] K. Christensen and N. R. Moloney, *Complexity and criticality*. World Scientific Publishing Company, 2005, vol. 1.
- [132] K. Falconer, *Fractal geometry: mathematical foundations and applications*. John Wiley & Sons, 2014.
- [133] M. Rams and K. Simon, “The geometry of fractal percolation”, in *Geometry and analysis of fractals*, Springer, 2014, pp. 303–323.
- [134] K. Falconer and X. Jin, “Self-similar sets: Projections, sections and percolation”, in *Conference of Fractals and Related Fields*, Springer, 2015, pp. 113–127.
- [135] B. B. Mandelbrot, *The fractal geometry of nature*. New York: WH Freeman, 1983.
- [136] Y. Feldman, A. Puzenko, and Y. Ryabov, “Dielectric relaxation phenomena in complex materials”, in *Fractals, Diffusion, and Relaxation in Disordered Complex Systems*. John Wiley & Sons, Ltd, 2006, ch. 1, pp. 1–125.
- [137] L. E. Cross, “Relaxorferroelectrics: An overview”, *Ferroelectrics*, vol. 151, no. 1, pp. 305–320, 1994.

- [138] J. Scott, “Applications of modern ferroelectrics”, *Science*, vol. 315, no. 5814, pp. 954–959, 2007.
- [139] R. Destro, R. Ruffo, P. Roversi, R. Soave, L. Loconte, and L. Lo Presti, “Anharmonic motions versus dynamic disorder at the mg ion from the charge densities in pyrope ($\text{Mg}_3\text{Al}_2\text{Si}_3\text{O}_{12}$) crystals at 30 K: Six of one, half a dozen of the other”, *Acta Crystallographica Section B: Structural Science, Crystal Engineering and Materials*, vol. 73, no. 4, pp. 722–736, 2017.
- [140] R. Destro, E. Sartirana, L. Loconte, R. Soave, P. Colombo, C. Destro, and L. Lo Presti, “Competing $C = O \cdots C - O$, $C - H \cdots O$, $Cl \cdots O$, and $Cl \cdots Cl$ interactions governing the structural phase transition of 2,6-dichloro-p-benzoquinone at $T_c = 122.6$ k”, *Crystal Growth & Design*, vol. 13, no. 10, pp. 4571–4582, 2013.
- [141] R. Destro, E. Ortoleva, R. Soave, L. Loconte, and L. L. Presti, “Detection and kinetics of the single-crystal to single-crystal complete transformation of a thiiuranium ion into thietanium ion”, *Physical Chemistry Chemical Physics*, vol. 11, no. 33, pp. 7181–7188, 2009.
- [142] L. L. Presti, M. Allieta, M. Scavini, P. Ghigna, L. Loconte, V. Scagnoli, and M. Brunelli, “Crystal structure and structural phase transitions in the $\text{GdBaCo}_2\text{O}_{5.0}$ cobaltite”, *Physical Review B*, vol. 84, no. 10, p. 104107, 2011.
- [143] L. L. Presti, D. Invernizzi, R. Soave, and R. Destro, “Looking for structural phase transitions in the colossal magnetoresistive thiospinel FeCr_2S_4 by a multi-temperature single-crystal x-ray diffraction study”, *Chemical physics letters*, vol. 416, no. 1-3, pp. 28–32, 2005.
- [144] X. Wang, J. Wang, Y. Yu, H. Zhang, and R. I. Boughton, “Growth of cubic $\text{KTa}_{1-x}\text{Nb}_x\text{O}_3$ crystal by czochralski method”, *Journal of crystal growth*, vol. 293, no. 2, pp. 398–403, 2006.
- [145] B. Zalar, A. Lebar, J. Seliger, R. Blinc, V. V. Laguta, and M. Itoh, “Nmr study of disorder in BaTiO_3 and SrTiO_3 ”, *Physical Review B*, vol. 71, no. 6, p. 064107, 2005.
- [146] B. Zalar, V. V. Laguta, and R. Blinc, “Nmr evidence for the coexistence of order-disorder and displacive components in barium titanate”, *Physical review letters*, vol. 90, no. 3, p. 037601, 2003.
- [147] A. Agranat, R. Hofmeister, and A. Yariv, “Characterization of a new photorefractive material: $\text{K}_{1-y}\text{L}_y\text{T}_{1-x}\text{N}_x$ ”, *Optics letters*, vol. 17, no. 10, pp. 713–715, 1992.
- [148] A. Hewat, “Cubic-tetragonal-orthorhombic-rhombohedral ferroelectric transitions in perovskite potassium niobate: Neutron powder profile refinement of the structures”, *Journal of Physics C: Solid State Physics*, vol. 6, no. 16, p. 2559, 1973.
- [149] J. Toulouse, “The three characteristic temperatures of relaxor dynamics and their meaning”, *Ferroelectrics*, vol. 369, no. 1, pp. 203–213, 2008.

- [150] X. Huang, S. Jiang, X. Xu, J. Wang, Q. Guan, J. Jiang, and D Feng, “Ferroelectric domain structures and phase transitions in $\text{KTa}_{1-x}\text{Nb}_x\text{O}_3$ crystals”, *physica status solidi (a)*, vol. 148, no. 2, pp. 611–618, 1995.
- [151] E Bouziane, M Fontana, and W Kleemann, “A study of the successive phase transitions in $\text{KTa}_{0.93}\text{Nb}_{0.07}\text{O}_3$ by light scattering, dielectric permittivity and light diffraction measurements”, *Journal of Physics: Condensed Matter*, vol. 6, no. 10, p. 1965, 1994.
- [152] G. Shirane and A. Takeda, “Transition energy and volume change at three transitions in barium titanate”, *Journal of the Physical Society of Japan*, vol. 7, no. 1, pp. 1–4, 1952.
- [153] D Rytz and H. Scheel, “Crystal growth of $\text{KTa}_{1-x}\text{Nb}_x\text{O}_3$ ($0 < x \leq 0.04$) solid solutions by a slow-cooling method”, *Journal of Crystal Growth*, vol. 59, no. 3, pp. 468–484, 1982.
- [154] E. Politova, E. Fortalnova, G. Kaleva, A. Mosunov, M. Safronenko, N. Venkovskii, V. Shvartsman, and W Kleemann, “Ferroelectric phase transitions and electroconducting properties of ceramic bimevov solid solutions (Me=La, Zr)”, *Ferroelectrics*, vol. 391, no. 1, pp. 3–11, 2009.
- [155] H. Fröhlich, *Theory of Dielectrics, 2nd ed.* Claredon Press, Oxford., 1958.
- [156] A Sassella, D Braga, M Campione, T Ciabattoni, M Moret, J Parravicini, and G. Parravicini, “Probing phase transitions and stability of organic semiconductor single crystals by dielectric investigation”, *Journal of applied physics*, vol. 109, no. 1, p. 013 529, 2011.
- [157] J.-C. Tolédano, V Janovec, V Kopský, J. Scott, and P Boček, “Structural phase transitions”, 2006.
- [158] K. Aizu, “Possible species of ferromagnetic, ferroelectric, and ferroelastic crystals”, *Physical Review B*, vol. 2, no. 3, p. 754, 1970.
- [159] A. Bokov and Z. Ye, *Reentrant phenomena in relaxors, nanoscale ferroelectrics and multiferroics: Key processing and characterization issues, and nanoscale effects*, 2016.
- [160] R Comes, M Lambert, and A Guinier, “Désordre linéaire dans les cristaux (cas du silicium, du quartz, et des pérovskites ferroélectriques)”, *Acta Crystallographica Section A: Crystal Physics, Diffraction, Theoretical and General Crystallography*, vol. 26, no. 2, pp. 244–254, 1970.
- [161] P. W. Forsbergh Jr, “Domain structures and phase transitions in barium titanate”, *Physical Review*, vol. 76, no. 8, p. 1187, 1949.
- [162] J Sapriel, “Domain-wall orientations in ferroelastics”, *Physical Review B*, vol. 12, no. 11, p. 5128, 1975.
- [163] J. G. M. Alguero and L. Mitoseriu, *Nanoscale Ferroelectrics and Multiferroics*. Wiley, Chichester, UK, 2016.
- [164] S Das, Y. Tang, Z Hong, M. Gonçalves, M. McCarter, C Klewe, K. Nguyen, F Gómez-Ortiz, P Shafer, E Arenholz, *et al.*, “Observation of room-temperature polar skyrmions”, *Nature*, vol. 568, no. 7752, pp. 368–372, 2019.

- [165] K. Wang and J.-F. Li, “Analysis of crystallographic evolution in (na, k) nb o 3-based lead-free piezoceramics by x-ray diffraction”, *Applied Physics Letters*, vol. 91, no. 26, p. 262 902, 2007.
- [166] S. Borisov, S. Vakhrushev, E. Y. Koroleva, A. Naberezhnov, P. Syrnikov, V. Simkin, Z Kutnjak, T Egami, W Dmowski, and P Piekarz, “Investigation into the evolution of the structure of $K_{1-x} Li_x Ta_{1-y} Nb_y O_3$ single crystals under variations in temperature”, *Crystallography Reports*, vol. 52, no. 3, pp. 440–446, 2007.
- [167] H. Abe, K Harada, R. Matsuo, H Uwe, and K Ohshima, “X-ray diffuse scattering associated with ferroelectric microregions in $KTa_{1-x} Nb_x O_3$ ”, *Journal of Physics: Condensed Matter*, vol. 13, no. 14, p. 3257, 2001.
- [168] P. Gehring, H. Chou, S. Shapiro, J. Hriljac, D. Chen, J Toulouse, D Rytz, and L. Boatner, “Dipole-glass behavior of lightly doped $KTa_{1-x} Nb_x O_3$ ”, *Physical Review B*, vol. 46, no. 9, p. 5116, 1992.
- [169] M. Hoffmann, F. P. Fengler, M. Herzig, T. Mittmann, B. Max, U. Schroeder, R. Negra, P. Lucian, S. Slesazek, and T. Mikolajick, “Unveiling the double-well energy landscape in a ferroelectric layer”, *Nature*, vol. 565, no. 7740, pp. 464–467, 2019.
- [170] M. Azuma, W.-t. Chen, H. Seki, M. Czapski, S. Olga, K. Oka, M. Mizumaki, T. Watanuki, N. Ishimatsu, N. Kawamura, *et al.*, “Colossal negative thermal expansion in $BiNiO_3$ induced by intermetallic charge transfer”, *Nature communications*, vol. 2, no. 1, pp. 1–5, 2011.
- [171] J. D. Dunitz, “Phase transitions in molecular crystals: Looking backwards, glancing sideways”, *Physica Scripta*, vol. 91, no. 11, p. 112 501, 2016.
- [172] Y. V. Mnyukh, “Molecular mechanism of polymorphic transitions”, *Molecular Crystals and Liquid Crystals*, vol. 52, no. 1, pp. 163–199, 1979.
- [173] S Triebwasser, “Study of ferroelectric transitions of solid-solution single crystals of $KNbO_3$ - $KTaO_3$ ”, *Physical Review*, vol. 114, no. 1, p. 63, 1959.
- [174] P. Tan, H. Tian, F. Huang, X. Meng, Y. Wang, C. Hu, X. Cao, L. Li, and Z. Zhou, “Strain-gradient-controlled disorder dynamics in chemically substituted ferroelectrics”, *Physical Review Applied*, vol. 11, no. 2, p. 024 037, 2019.
- [175] J. Parravicini, P. Minzioni, V. Degiorgio, and E. DelRe, “Observation of nonlinear airy-like beam evolution in lithium niobate”, *Optics letters*, vol. 34, no. 24, pp. 3908–3910, 2009.
- [176] J Parravicini, F Di Mei, C Conti, A. Agranat, and E DelRe, “Diffraction cancellation over multiple wavelengths in photorefractive dipolar glasses”, *Optics express*, vol. 19, no. 24, pp. 24 109–24 114, 2011.
- [177] J Parravicini, C Conti, A. Agranat, and E DelRe, “Rejuvenation in scale-free optics and enhanced diffraction cancellation life-time”, *Optics express*, vol. 20, no. 24, pp. 27 382–27 387, 2012.
- [178] G. Johari, “Effects of electric field on the entropy, viscosity, relaxation time, and glass-formation”, *The Journal of chemical physics*, vol. 138, no. 15, p. 154 503, 2013.

-
- [179] L. L. E. Lifshitz, *Electrodynamics of Continuous Media*. Pergamon Press, Oxford, UK., 1960.
- [180] J. F. Nye *et al.*, *Physical properties of crystals: their representation by tensors and matrices*. Oxford university press, 1985.
- [181] A. Devonshire, “Theory of ferroelectrics”, *Advances in physics*, vol. 3, no. 10, pp. 85–130, 1954.
- [182] Y. S. Kivshar and G. Agrawal, *Optical solitons: from fibers to photonic crystals*. Academic press, 2003.
- [183] A. Ashkin, G. Boyd, J. Dziedzic, R. Smith, A. Ballman, J. Levinstein, and K. Nassau, “Optically-induced refractive index inhomogeneities in LiNbO_3 and LiTaO_3 ”, *Applied Physics Letters*, vol. 9, no. 1, pp. 72–74, 1966.
- [184] P. Günter and J. P. Huignard, *Photorefractive Materials and Their Applications 1: Basic Effects*. Springer, 2007, vol. 114.
- [185] P. Yeh *et al.*, *Introduction to photorefractive nonlinear optics*. Wiley-Interscience, 1993, vol. 14.
- [186] N. Kukhtarev, “Kinetics of hologram recording and erasure in electrooptic crystals”, *Technical Physics Letters*, vol. 2, pp. 438–440, 1976.
- [187] E. DelRe, A. Ciattoni, B. Crosignani, and M. Tamburrini, “Approach to space-charge field description in photorefractive crystals”, *JOSA B*, vol. 15, no. 5, pp. 1469–1475, 1998.
- [188] E. DelRe, B. Crosignani, and P. Di Porto, “Photorefractive solitons and their underlying nonlocal physics”, *Progress in Optics*, vol. 53, p. 153, 2009.
- [189] J. Petter, C. Weidmann, C. Denz, A. Stepken, and F. Kaiser, “Self-bending of photorefractive solitons”, *Optics communications*, vol. 170, no. 4-6, pp. 291–297, 1999.
- [190] E. DelRe and E. Palange, “Optical nonlinearity and existence conditions for quasi-steady-state photorefractive solitons”, *JOSA B*, vol. 23, no. 11, pp. 2323–2327, 2006.
- [191] L. F. Mollenauer, R. H. Stolen, and J. P. Gordon, “Experimental observation of picosecond pulse narrowing and solitons in optical fibers”, *Physical Review Letters*, vol. 45, no. 13, p. 1095, 1980.
- [192] B. Kibler, J. Fatome, C. Finot, G. Millot, F. Dias, G. Genty, N. Akhmediev, and J. M. Dudley, “The peregrine soliton in nonlinear fibre optics”, *Nature Physics*, vol. 6, no. 10, p. 790, 2010.
- [193] S. Barland, J. R. Tredicce, M. Brambilla, L. A. Lugiato, S. Balle, M. Giudici, T. Maggipinto, L. Spinelli, G. Tissoni, T. Knoedl, *et al.*, “Cavity solitons as pixels in semiconductor microcavities”, *Nature*, vol. 419, no. 6908, p. 699, 2002.
- [194] K. E. Strecker, G. B. Partridge, A. G. Truscott, and R. G. Hulet, “Formation and propagation of matter-wave soliton trains”, *Nature*, vol. 417, no. 6885, p. 150, 2002.

-
- [195] A Chabchoub, N. Hoffmann, and N. Akhmediev, “Rogue wave observation in a water wave tank”, *Physical Review Letters*, vol. 106, no. 20, p. 204502, 2011.
- [196] M. Segev and A. J. Agranat, “Spatial solitons in centrosymmetric photorefractive media”, *Optics letters*, vol. 22, no. 17, pp. 1299–1301, 1997.
- [197] D. N. Christodoulides and M. Carvalho, “Bright, dark, and gray spatial soliton states in photorefractive media”, *JOSA B*, vol. 12, no. 9, pp. 1628–1633, 1995.
- [198] D Burak and W Nasalski, “Gaussian beam to spatial soliton formation in kerr media”, *Applied optics*, vol. 33, no. 27, pp. 6393–6401, 1994.
- [199] E DelRe, M Segev, D Christodoulides, B Crosignani, and G Salamo, “Photorefractive solitons”, in *Photorefractive Materials and Their Applications 1*, Springer, 2006, pp. 317–367.
- [200] E DelRe, G De Masi, A Ciattoni, and E Palange, “Pairing space-charge field conditions with self-guiding for the attainment of circular symmetry in photorefractive solitons”, *Applied physics letters*, vol. 85, no. 23, pp. 5499–5501, 2004.
- [201] M. Onorato, S Residori, U Bortolozzo, A Montina, and F. Arecchi, “Rogue waves and their generating mechanisms in different physical contexts”, *Physics Reports*, vol. 528, no. 2, pp. 47–89, 2013.
- [202] K. Dysthe, H. E. Krogstad, and P. Müller, “Oceanic rogue waves”, *Annu. Rev. Fluid Mech.*, vol. 40, pp. 287–310, 2008.
- [203] J. W. Goodman, “Statistical properties of laser speckle patterns”, in *Laser speckle and related phenomena*, Springer, 1975, pp. 9–75.
- [204] S. Wabnitz, *Nonlinear guided wave optics: a testbed for extreme waves*. IOP Publishing, 2017.
- [205] D. A. Miller, “Silicon photonics: Meshing optics with applications”, *Nature Photonics*, vol. 11, no. 7, p. 403, 2017.
- [206] Y. Shen, N. C. Harris, S. Skirlo, M. Prabhu, T. Baehr-Jones, M. Hochberg, X. Sun, S. Zhao, H. Larochelle, D. Englund, *et al.*, “Deep learning with coherent nanophotonic circuits”, *Nature Photonics*, vol. 11, no. 7, p. 441, 2017.
- [207] N. C. Harris, G. R. Steinbrecher, M. Prabhu, Y. Lahini, J. Mower, D. Bunandar, C. Chen, F. N. Wong, T. Baehr-Jones, M. Hochberg, *et al.*, “Quantum transport simulations in a programmable nanophotonic processor”, *Nature Photonics*, vol. 11, no. 7, p. 447, 2017.
- [208] X. Qiang, X. Zhou, J. Wang, C. M. Wilkes, T. Loke, S. O’Gara, L. Kling, G. D. Marshall, R. Santagati, T. C. Ralph, *et al.*, “Large-scale silicon quantum photonics implementing arbitrary two-qubit processing”, *Nature Photonics*, vol. 12, no. 9, p. 534, 2018.
- [209] J. W. Chan, T. R. Huser, S. H. Risbud, J. S. Hayden, and D. M. Krol, “Waveguide fabrication in phosphate glasses using femtosecond laser pulses”, *Applied physics letters*, vol. 82, no. 15, pp. 2371–2373, 2003.

- [210] A. C. Sullivan, M. W. Grabowski, and R. R. McLeod, “Three-dimensional direct-write lithography into photopolymer”, *Applied optics*, vol. 46, no. 3, pp. 295–301, 2007.
- [211] G. D. Marshall, A. Politi, J. C. Matthews, P. Dekker, M. Ams, M. J. Withford, and J. L. O’Brien, “Laser written waveguide photonic quantum circuits”, *Optics express*, vol. 17, no. 15, pp. 12 546–12 554, 2009.
- [212] F. Flamini, L. Magrini, A. S. Rab, N. Spagnolo, V. D’ambrosio, P. Mataloni, F. Sciarrino, T. Zandrini, A. Crespi, R. Ramponi, *et al.*, “Thermally reconfigurable quantum photonic circuits at telecom wavelength by femtosecond laser micromachining”, *Light: Science & Applications*, vol. 4, no. 11, e354, 2015.
- [213] Z. Chaboyer, A Stokes, J Downes, M. Steel, and M. J. Withford, “Design and fabrication of reconfigurable laser-written waveguide circuits”, *Optics Express*, vol. 25, no. 26, pp. 33 056–33 065, 2017.
- [214] Y. Yang, X. Song, X. Li, Z. Chen, C. Zhou, Q. Zhou, and Y. Chen, “Recent progress in biomimetic additive manufacturing technology: From materials to functional structures”, *Advanced Materials*, p. 1 706 539, 2018.
- [215] T. M. Monro, C. M. De Sterke, and L Poladian, “Catching light in its own trap”, *Journal of Modern Optics*, vol. 48, no. 2, pp. 191–238, 2001.
- [216] M. Asaro, M. Sheldon, Z. Chen, O. Ostroverkhova, and W. Moerner, “Soliton-induced waveguides in an organic photorefractive glass”, *Optics letters*, vol. 30, no. 5, pp. 519–521, 2005.
- [217] H. Terasawa, F. Tan, O. Sugihara, A. Kawasaki, D. Inoue, T. Yamashita, M. Kagami, O. Maury, Y. Bretonnière, and C. Andraud, “Light-induced self-written waveguide fabrication using 1550 nm laser light”, *Optics letters*, vol. 42, no. 11, pp. 2236–2238, 2017.
- [218] A. Bezryadina, T. Hansson, R. Gautam, B. Wetzal, G. Siggins, A. Kalmbach, J. Lamstein, D. Gallardo, E. J. Carpenter, A. Ichimura, *et al.*, “Nonlinear self-action of light through biological suspensions”, *Physical review letters*, vol. 119, no. 5, p. 058 101, 2017.
- [219] R. Malallah, D. Cassidy, I. Muniraj, J. P. Ryle, J. J. Healy, and J. T. Sheridan, “Self-written waveguides in photopolymer”, *Applied Optics*, vol. 57, no. 22, E80–E88, 2018.
- [220] S. Lan, E. DelRe, Z. Chen, M.-f. Shih, and M. Segev, “Directional coupler with soliton-induced waveguides”, *Optics letters*, vol. 24, no. 7, pp. 475–477, 1999.
- [221] K. Dorkenoo, O. Crégut, L. Mager, F. Gillot, C. Carre, and A. Fort, “Quasi-solitonic behavior of self-written waveguides created by photopolymerization”, *Optics letters*, vol. 27, no. 20, pp. 1782–1784, 2002.
- [222] Z. Chen, M. Segev, and D. N. Christodoulides, “Optical spatial solitons: Historical overview and recent advances”, *Reports on Progress in Physics*, vol. 75, no. 8, p. 086 401, 2012.

- [223] C.-C. Jeng, Y. Su, R.-C. Hong, and R.-K. Lee, “Control modulation instability in photorefractive crystals by the intensity ratio of background to signal fields”, *Optics express*, vol. 23, no. 8, pp. 10 266–10 271, 2015.
- [224] J. Durnin, J. Miceli Jr, and J. Eberly, “Diffraction-free beams”, *Physical review letters*, vol. 58, no. 15, p. 1499, 1987.
- [225] D. McGloin and K. Dholakia, “Bessel beams: Diffraction in a new light”, *Contemporary Physics*, vol. 46, no. 1, pp. 15–28, 2005.
- [226] M. V. Berry and N. L. Balazs, “Nonspreading wave packets”, *American Journal of Physics*, vol. 47, no. 3, pp. 264–267, 1979.
- [227] M. A. Bandres and J. C. Gutiérrez-Vega, “Airy-gauss beams and their transformation by paraxial optical systems”, *Optics Express*, vol. 15, no. 25, pp. 16 719–16 728, 2007.
- [228] F Gori, G Guattari, and C Padovani, “Bessel-gauss beams”, *Optics communications*, vol. 64, no. 6, pp. 491–495, 1987.
- [229] C. R. Pollock and M. Lipson, *Integrated photonics*, 25. Springer, 2003, vol. 20.
- [230] M. A. Porras, A. Parola, D. Faccio, A. Dubietis, and P. Di Trapani, “Nonlinear unbalanced bessel beams: Stationary conical waves supported by nonlinear losses”, *Physical review letters*, vol. 93, no. 15, p. 153 902, 2004.
- [231] M. A. Porras, C. Ruiz-Jiménez, and J. C. Losada, “Underlying conservation and stability laws in nonlinear propagation of axicon-generated bessel beams”, *Physical Review A*, vol. 92, no. 6, p. 063 826, 2015.
- [232] E. DelRe, B. Crosignani, P. Di Porto, E. Palange, and A. J. Agranat, “Electro-optic beam manipulation through photorefractive needles”, *Optics letters*, vol. 27, no. 24, pp. 2188–2190, 2002.
- [233] A Pierangelo, A Ciattoni, E Palange, A. Agranat, and E DelRe, “Electro-activation and electro-morphing of photorefractive funnel waveguides”, *Optics Express*, vol. 17, no. 25, pp. 22 659–22 665, 2009.
- [234] E. DelRe, A. Pierangelo, E. Palange, A Ciattoni, and A. Agranat, “Beam shaping and effective guiding in the bulk of photorefractive crystals through linear beam dynamics”, *Applied Physics Letters*, vol. 91, no. 8, p. 081 105, 2007.
- [235] A Pierangelo, E DelRe, A Ciattoni, E Palange, A. Agranat, and B Crosignani, “Linear writing of waveguides in bulk photorefractive crystals through a two-step polarization sequence”, *Journal of Optics A: Pure and Applied Optics*, vol. 10, no. 6, p. 064 005, 2008.
- [236] G Di Domenico, J Parravicini, G Antonacci, S Silvestri, A. Agranat, and E DelRe, “Miniaturized photogenerated electro-optic axicon lens gaussian-to-bessel beam conversion”, *Applied optics*, vol. 56, no. 10, pp. 2908–2911, 2017.
- [237] G Antonacci, G Di Domenico, S Silvestri, E DelRe, and G Ruocco, “Diffraction-free light droplets for axially-resolved volume imaging”, *Scientific Reports*, vol. 7, no. 1, p. 17, 2017.

- [238] E. DelRe, A. Ciattoni, and A. J. Agranat, “Anisotropic charge displacement supporting isolated photorefractive optical needles”, *Optics letters*, vol. 26, no. 12, pp. 908–910, 2001.
- [239] J Arlt and K Dholakia, “Generation of high-order bessel beams by use of an axicon”, *Optics Communications*, vol. 177, no. 1-6, pp. 297–301, 2000.
- [240] J. Arlt, V. Garcés-Chávez, W. Sibbett, and K. Dholakia, “Optical micro-manipulation using a bessel light beam”, *Optics communications*, vol. 197, no. 4-6, pp. 239–245, 2001.
- [241] P. Polesana, D. Faccio, P. Di Trapani, A. Dubietis, A. Piskarskas, A. Couairon, and M. A. Porras, “High localization, focal depth and contrast by means of nonlinear bessel beams”, *Optics express*, vol. 13, no. 16, pp. 6160–6167, 2005.
- [242] M. K. Bhuyan, F. Courvoisier, P.-A. Lacourt, M. Jacquot, L. Furfaro, M. Withford, and J. Dudley, “High aspect ratio taper-free microchannel fabrication using femtosecond bessel beams”, *Optics express*, vol. 18, no. 2, pp. 566–574, 2010.
- [243] C. L. Arnold, S. Akturk, A. Mysyrowicz, V. Jukna, A. Couairon, T. Itina, R. Stoian, C Xie, J. Dudley, F Courvoisier, *et al.*, “Nonlinear bessel vortex beams for applications”, *Journal of Physics B: Atomic, Molecular and Optical Physics*, vol. 48, no. 9, p. 094 006, 2015.
- [244] C. Xie, V. Jukna, C. Milián, R. Giust, I. Ouadghiri-Idrissi, T. Itina, J. M. Dudley, A. Couairon, and F. Courvoisier, “Tubular filamentation for laser material processing”, *Scientific reports*, vol. 5, p. 8914, 2015.
- [245] A. Dreischuh, D. N. Neshev, D. E. Petersen, O. Bang, and W. Krolikowski, “Observation of attraction between dark solitons”, *Physical review letters*, vol. 96, no. 4, p. 043 901, 2006.
- [246] E. DelRe, S. Trillo, and A. J. Agranat, “Collisions and inhomogeneous forces between solitons of different dimensionality”, *Optics letters*, vol. 25, no. 8, pp. 560–562, 2000.
- [247] G. I. Stegeman and M. Segev, “Optical spatial solitons and their interactions: Universality and diversity”, *Science*, vol. 286, no. 5444, pp. 1518–1523, 1999.
- [248] C. Conti, “Complex light: Dynamic phase transitions of a light beam in a nonlinear nonlocal disordered medium”, *Physical Review E*, vol. 72, no. 6, p. 066 620, 2005.
- [249] D. R. Solli, C. Ropers, P. Koonath, and B. Jalali, “Optical rogue waves”, *Nature*, vol. 450, no. 7172, pp. 1054–1057, 2007.
- [250] G. Genty, C. M. de Sterke, O. Bang, F Dias, N. Akhmediev, and J. M. Dudley, “Collisions and turbulence in optical rogue wave formation”, *Physics Letters A*, vol. 374, no. 7, pp. 989–996, 2010.
- [251] A. Slunyaev and E. Pelinovsky, “Role of multiple soliton interactions in the generation of rogue waves: The modified korteweg–de vries framework”, *Physical review letters*, vol. 117, no. 21, p. 214 501, 2016.
- [252] A. Clauset, C. R. Shalizi, and M. E. Newman, “Power-law distributions in empirical data”, *SIAM review*, vol. 51, no. 4, pp. 661–703, 2009.

-
- [253] R. P. Feynman, R. B. Leighton, and M. Sands, “The feynman lectures on physics; vol. I”, *American Journal of Physics*, vol. 33, no. 9, pp. 750–752, 1965.
- [254] R. D. Astumian, “Thermodynamics and kinetics of a brownian motor”, *science*, vol. 276, no. 5314, pp. 917–922, 1997.
- [255] J. M. Dudley, F. Dias, M. Erkintalo, and G. Genty, “Instabilities, breathers and rogue waves in optics”, *Nature Photonics*, vol. 8, no. 10, pp. 755–764, 2014.
- [256] S. Birkholz, C. Brée, A. Demircan, and G. Steinmeyer, “Predictability of rogue events”, *Physical review letters*, vol. 114, no. 21, p. 213 901, 2015.
- [257] P. Walczak, S. Randoux, and P. Suret, “Optical rogue waves in integrable turbulence”, *Physical review letters*, vol. 114, no. 14, p. 143 903, 2015.
- [258] N. Akhmediev, B. Kibler, F. Baronio, M. Belić, W.-P. Zhong, Y. Zhang, W. Chang, J. M. Soto-Crespo, P. Vouzas, P. Grellu, *et al.*, “Roadmap on optical rogue waves and extreme events”, *Journal of Optics*, vol. 18, no. 6, p. 063 001, 2016.
- [259] P. Suret, R. El Koussaifi, A. Tikan, C. Evain, S. Randoux, C. Szwaj, and S. Bielawski, “Single-shot observation of optical rogue waves in integrable turbulence using time microscopy”, *Nature communications*, vol. 7, no. 1, pp. 1–8, 2016.
- [260] Z. Yang, W.-P. Zhong, M. Belić, and Y. Zhang, “Controllable optical rogue waves via nonlinearity management”, *Optics express*, vol. 26, no. 6, pp. 7587–7597, 2018.
- [261] A. Armaroli, C. Conti, and F. Biancalana, “Rogue solitons in optical fibers: A dynamical process in a complex energy landscape?”, *Optica*, vol. 2, no. 5, pp. 497–504, 2015.
- [262] J. M. Soto-Crespo, N. Devine, and N. Akhmediev, “Integrable turbulence and rogue waves: Breathers or solitons?”, *Physical review letters*, vol. 116, no. 10, p. 103 901, 2016.
- [263] T Kanna, M Lakshmanan, P. T. Dinda, and N. Akhmediev, “Soliton collisions with shape change by intensity redistribution in mixed coupled nonlinear schrödinger equations”, *Physical Review E*, vol. 73, no. 2, p. 026 604, 2006.
- [264] R. Driben and I. Babushkin, “Accelerated rogue waves generated by soliton fusion at the advanced stage of supercontinuum formation in photonic-crystal fibers”, *Optics letters*, vol. 37, no. 24, pp. 5157–5159, 2012.
- [265] A. Yulin, R Driben, B. Malomed, and D. Skryabin, “Soliton interaction mediated by cascaded four wave mixing with dispersive waves”, *Optics express*, vol. 21, no. 12, pp. 14 481–14 486, 2013.
- [266] P. Andrekson, N. Olsson, P. Becker, J. Simpson, T Tanbun-Ek, R. Logan, and K. Wecht, “Observation of multiple wavelength soliton collisions in optical systems with fiber amplifiers”, *Applied physics letters*, vol. 57, no. 17, pp. 1715–1717, 1990.

- [267] K Kurokawa, H Kubota, and M Nakazawa, “Soliton self-frequency shift accelerated by femtosecond soliton interaction”, *Electronics Letters*, vol. 28, no. 22, pp. 2052–2054, 1992.
- [268] A Mussot, A Kudlinski, M Kolobov, E Louvergneaux, M Douay, and M. Taki, “Observation of extreme temporal events in cw-pumped supercontinuum”, *Optics express*, vol. 17, no. 19, pp. 17 010–17 015, 2009.
- [269] J. P. Gordon, “Theory of the soliton self-frequency shift”, *Optics letters*, vol. 11, no. 10, pp. 662–664, 1986.
- [270] Y Kodama and K Nozaki, “Soliton interaction in optical fibers”, *Optics letters*, vol. 12, no. 12, pp. 1038–1040, 1987.
- [271] B.-J. Hong and C.-C. Yang, “Interactions between femtosecond solitons in optical fibers”, *JOSA B*, vol. 8, no. 5, pp. 1114–1121, 1991.
- [272] In *Nonlinear Fiber Optics (Fifth Edition)*, G. Agrawal, Ed., Fifth Edition, Academic Press, 2013.
- [273] P. Yeh, “Two-wave mixing in nonlinear media”, in *Landmark Papers On Photorefractive Nonlinear Optics*, World Scientific, 1995, pp. 97–132.
- [274] D. Timotijević, M Belic, and R. Boyd, “Two- and four-wave mixing with saturable absorption and gain”, *IEEE journal of quantum electronics*, vol. 28, no. 9, pp. 1915–1921, 1992.
- [275] N. Akhmediev, W. Królikowski, and A. Lowery, “Influence of the raman-effect on solitons in optical fibers”, *Optics communications*, vol. 131, no. 4-6, pp. 260–266, 1996.
- [276] F Luan, D. Skryabin, A. Yulin, and J. Knight, “Energy exchange between colliding solitons in photonic crystal fibers”, *Optics express*, vol. 14, no. 21, pp. 9844–9853, 2006.
- [277] S. Chi and S. Wen, “Raman cross talk of soliton collision in a lossless fiber”, *Optics letters*, vol. 14, no. 21, pp. 1216–1218, 1989.
- [278] D Pierangeli, G Musarra, F Di Mei, G Di Domenico, A. Agranat, C Conti, and E DelRe, “Enhancing optical extreme events through input wave disorder”, *Physical Review A*, vol. 94, no. 6, p. 063 833, 2016.
- [279] E. DelRe, A. D’Ercole, and E. Palange, “Mechanisms supporting long propagation regimes of photorefractive solitons”, *Physical Review E*, vol. 71, no. 3, p. 036 610, 2005.
- [280] M. Chi, J.-P. Huignard, and P. M. Petersen, “A general theory of two-wave mixing in nonlinear media”, *JOSA B*, vol. 26, no. 8, pp. 1578–1584, 2009.
- [281] W. Królikowski and S. A. Holmstrom, “Fusion and birth of spatial solitons upon collision”, *Optics letters*, vol. 22, no. 6, pp. 369–371, 1997.
- [282] W. Królikowski, N. Akhmediev, B. Luther-Davies, and M. Cronin-Golomb, “Self-bending photorefractive solitons”, *Physical Review E*, vol. 54, no. 5, p. 5761, 1996.

-
- [283] M. H. Frosz, O. Bang, and A. Bjarklev, “Soliton collision and raman gain regimes in continuous-wave pumped supercontinuum generation”, *Optics express*, vol. 14, no. 20, pp. 9391–9407, 2006.
- [284] A. Picozzi, J. Garnier, T. Hansson, P. Suret, S. Randoux, G. Millot, and D. N. Christodoulides, “Optical wave turbulence: Towards a unified nonequilibrium thermodynamic formulation of statistical nonlinear optics”, *Physics Reports*, vol. 542, no. 1, pp. 1–132, 2014.
- [285] U. Bortolozzo, J. Laurie, S. Nazarenko, and S. Residori, “Optical wave turbulence and the condensation of light”, *JOSA B*, vol. 26, no. 12, pp. 2280–2284, 2009.
- [286] B. A. Malomed, D. Mihalache, F. Wise, and L. Torner, “Spatiotemporal optical solitons”, *Journal of Optics B: Quantum and Semiclassical Optics*, vol. 7, no. 5, R53, 2005.
- [287] M. Wimmer, A. Regensburger, M.-A. Miri, C. Bersch, D. N. Christodoulides, and U. Peschel, “Observation of optical solitons in pt-symmetric lattices”, *Nature communications*, vol. 6, no. 1, pp. 1–9, 2015.
- [288] J. Peng, N. Tarasov, S. Sugavanam, and D. Churkin, “Rogue waves generation via nonlinear soliton collision in multiple-soliton state of a mode-locked fiber laser”, *Optics express*, vol. 24, no. 19, pp. 21 256–21 263, 2016.
- [289] S. Birkholz, E. T. Nibbering, C. Brée, S. Skupin, A. Demircan, G. Genty, and G. Steinmeyer, “Spatiotemporal rogue events in optical multiple filamentation”, *Physical review letters*, vol. 111, no. 24, p. 243 903, 2013.
- [290] F. Xin, M. Flammini, F. Di Mei, L. Falsi, D. Pierangeli, A. J. Agranat, and E. DelRe, “Observation of extreme nonreciprocal wave amplification from single soliton-soliton collisions”, *Physical Review A*, vol. 100, no. 4, p. 043 816, 2019.
- [291] F. Xin, F. Di Mei, L. Falsi, D. Pierangeli, A. J. Agranat, and E. DelRe, “Soliton maxwell demons and long-tailed statistics in fluctuating optical fields”, *Optics letters*, vol. 45, no. 3, pp. 648–651, 2020.
- [292] C. Bonatto, M. Feyereisen, S. Barland, M. Giudici, C. Masoller, J. R. R. Leite, and J. R. Tredicce, “Deterministic optical rogue waves”, *Physical review letters*, vol. 107, no. 5, p. 053 901, 2011.
- [293] F Selmi, S. Coulibaly, Z Loghmari, I. Sagnes, G. Beaudoin, M. G. Clerc, and S. Barbay, “Spatiotemporal chaos induces extreme events in an extended microcavity laser”, *Physical review letters*, vol. 116, no. 1, p. 013 901, 2016.
- [294] S Coulibaly, M. Clerc, F Selmi, and S Barbay, “Extreme events following bifurcation to spatiotemporal chaos in a spatially extended microcavity laser”, *Physical Review A*, vol. 95, no. 2, p. 023 816, 2017.
- [295] H. Poincaré, *Les méthodes nouvelles de la mécanique céleste: Méthodes de MM. Newcomb, Glydén, Lindstedt et Bohlín. 1893*. Gauthier-Villars it fils, 1893, vol. 2.

-
- [296] N. C. Stone and N. W. Leigh, “A statistical solution to the chaotic, non-hierarchical three-body problem”, *Nature*, vol. 576, no. 7787, pp. 406–410, 2019.
- [297] H. Frauenkron, Y. S. Kivshar, and B. A. Malomed, “Multisoliton collisions in nearly integrable systems”, *Physical Review E*, vol. 54, no. 3, R2244, 1996.
- [298] W. Królikowski, B. Luther-Davies, C. Denz, and T. Tschudi, “Annihilation of photorefractive solitons”, *Optics letters*, vol. 23, no. 2, pp. 97–99, 1998.
- [299] N. Akhmediev, W. Królikowski, and A. Snyder, “Partially coherent solitons of variable shape”, *Physical review letters*, vol. 81, no. 21, p. 4632, 1998.
- [300] A. A. Sukhorukov and N. N. Akhmediev, “Coherent and incoherent contributions to multisoliton complexes”, *Physical Review Letters*, vol. 83, no. 23, p. 4736, 1999.
- [301] N. Akhmediev and A. Ankiewicz, “Multi-soliton complexes”, *Chaos: An Interdisciplinary Journal of Nonlinear Science*, vol. 10, no. 3, pp. 600–612, 2000.
- [302] A. Martin, C. Adams, and S. Gardiner, “Bright matter-wave soliton collisions in a harmonic trap: Regular and chaotic dynamics”, *Physical review letters*, vol. 98, no. 2, p. 020 402, 2007.
- [303] F. Dalfovo, S. Giorgini, L. P. Pitaevskii, and S. Stringari, “Theory of bose-einstein condensation in trapped gases”, *Reviews of modern physics*, vol. 71, no. 3, p. 463, 1999.
- [304] A. Vulpiani, F. Cecconi, and M. Cencini, *Chaos: from simple models to complex systems*. World Scientific, 2009, vol. 17.
- [305] R. A. Fisher and W. Bischel, “The role of linear dispersion in plane-wave self-phase modulation”, *Applied Physics Letters*, vol. 23, no. 12, pp. 661–663, 1973.
- [306] S. Sugavanam, M. K. Kopae, J. Peng, J. E. Prilepsky, and S. K. Turitsyn, “Analysis of laser radiation using the nonlinear fourier transform”, *Nature communications*, vol. 10, no. 1, pp. 1–10, 2019.
- [307] P. Suret, A. Tikan, F. Bonnefoy, F. Copie, G. Ducrozet, A. Gelash, G. Prabhudesai, G. Michel, A. Cazaubiel, E. Falcon, *et al.*, “Nonlinear spectral synthesis of soliton gas in deep-water surface gravity waves”, *Physical Review Letters*, vol. 125, no. 26, p. 264 101, 2020.